

## N O T I C E

THIS DOCUMENT HAS BEEN REPRODUCED FROM  
MICROFICHE. ALTHOUGH IT IS RECOGNIZED THAT  
CERTAIN PORTIONS ARE ILLEGIBLE, IT IS BEING RELEASED  
IN THE INTEREST OF MAKING AVAILABLE AS MUCH  
INFORMATION AS POSSIBLE

INTERIM REPORT

on the

DESIGN, ANALYSIS, AND TEST VERIFICATION  
OF ADVANCED ENCAPSULATION SYSTEMS

For Period Ending

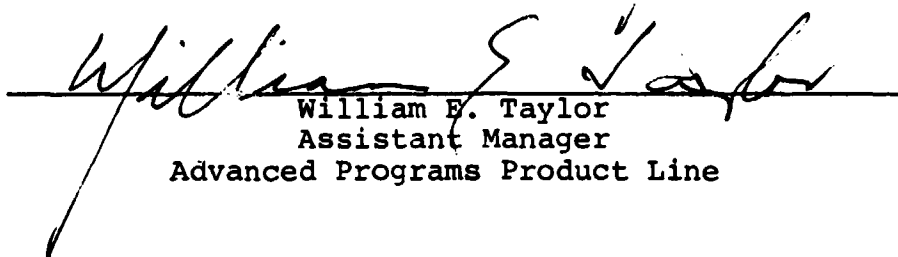
1 October 1980

Contract 955567

Prepared by:

Alec Garcia  
Chuck Minning

Approved by:

  
William E. Taylor  
Assistant Manager  
Advanced Programs Product Line

SPECTROLAB, INC.  
12500 Gladstone Avenue  
Sylmar, CA 91342

November 1981



The JPL Low-Cost Solar Array Project is sponsored by the U.S. Department of Energy and forms part of the Solar Photovoltaic Conversion Program to initiate a major effort toward the development of low-cost solar arrays. This work was performed for the Jet Propulsion Laboratory, California Institute of Technology by agreement between NASA and DOE.

(NASA-CR-168407) DESIGN, ANALYSIS, AND TEST  
VERIFICATION OF ADVANCED ENCAPSULATION  
SYSTEMS Interim Report, period ending 1  
Oct. 1980 (Spectrolab, Inc.) 178 P CSCI 10A G3/44  
HC A09/HF A01  
N82-17604  
Unclas  
08829

INTERIM REPORT

on the

DESIGN, ANALYSIS, AND TEST VERIFICATION  
OF ADVANCED ENCAPSULATION SYSTEMS

For Period Ending

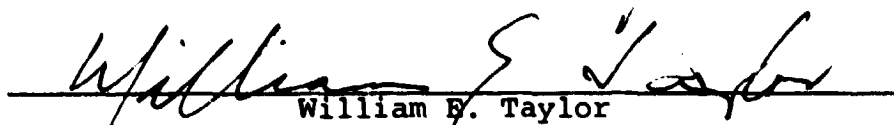
1 October 1980

Contract 955567

Prepared by:

Alec Garcia  
Chuck Minning

Approved by:



William B. Taylor  
Assistant Manager  
Advanced Programs Product Line

SPECTROLAB, INC.  
12500 Gladstone Avenue  
Sylmar, CA 91342

November 1981

The JPL Low-Cost Solar Array Project is sponsored by the U.S. Department of Energy and forms part of the Solar Photovoltaic Conversion Program to initiate a major effort toward the development of low-cost solar arrays. This work was performed for the Jet Propulsion Laboratory, California Institute of Technology by agreement between NASA and DOE.

## ACKNOWLEDGEMENT

The work presented in this report is the result of the joint effort of numerous individuals at both Spectrolab and Hughes Aircraft Company. Members of the team and their respective areas of technical responsibility were as follows:

- +J.P. Bagby - Consultant on optical analysis
- +Dr. J. F. Coakley - Thermal, optical analyses
- +L. B. Duncan - Structural analysis
- \*A. Garcia III - Photovoltaic consultant, program management
- +Dr. C. P. Minning - Electrical analysis, program management
- +C. M. Perrygo - Optical analysis
- +A. H. Samuels - Failure mode analysis
- +D. H. Simons - Electrical analysis
- \*Dr. W. E. Taylor - Photovoltaic consultant, program management
- +S. S. Tung - Failure mode analysis
- +N. K. Weaver - Electrical analysis

\* - Spectrolab

+ - Hughes Aircraft Company

## PREFACE

This report documents the first phase of a three-phase program that is a joint effort by Spectrolab and Hughes Aircraft Company. The objective of Phase 1 was to develop an analytical model which would enable the prediction of performance of various encapsulation designs. Models relating to the thermal, optical, structural, and electrical performance were developed. Using this analytical method the most cost effective module design can be found.

The second phase will verify the models by testing modules and coupons. The models may then be modified as necessary to bring predicted and empirically found results into agreement. Additionally, full-size modules of the most cost effective design will be built and put through the JPL qualification test sequence.

During the third phase Spectrolab will finalize the low cost design and deliver the design to JPL.

## TABLE OF CONTENTS

	<u>Page</u>
LIST OF FIGURES . . . . .	iii
LIST OF TABLES. . . . .	vii
1.0 SUMMARY. . . . .	1
2.0 INTRODUCTION . . . . .	4
3.0 STRUCTURAL ANALYSIS. . . . .	12
3.1 Introduction. . . . .	12
3.2 Thickness Determination for Structural (Load-Bearing) Member. .	13
3.3 Stiffening Rib Studies. . . . .	16
3.4 Pottant Thickness Determination . . . . .	18
3.5 Edge Attachment Considerations. . . . .	28
3.6 Conclusions . . . . .	32
4.0 ELECTRICAL ANALYSIS. . . . .	34
4.1 Introduction. . . . .	34
4.2 Analytical Models . . . . .	35
4.3 Discussion. . . . .	39
4.4 Conclusions . . . . .	42
5.0 OPTICAL ANALYSIS . . . . .	49
5.1 Introduction. . . . .	49
5.2 Basic Principles and Background Information . . . . .	50
5.3 Analytical Procedure and Equations. . . . .	65
6.0 THERMAL ANALYSIS . . . . .	75
6.1 Introduction. . . . .	75
6.2 Basic Equations . . . . .	75
6.3 Computational Sequence . . . . .	80
6.4 Computer Program. . . . .	81
6.5 Results . . . . .	81
6.6 Sensitivity Studies . . . . .	94
6.7 Conclusions . . . . .	99

## TABLE OF CONTENTS (Continued)

	<u>Page</u>
7.0 TECHNOLOGY VOIDS . . . . .	100
7.1 Influence of Pottant Modulus and Thickness on Solar Cell Stress . . . . .	100
7.2 Allowable Fatigue Strength for Silicon. . . . .	101
7.3 Effects of Humidity on Module Design. . . . .	101
7.4 Data Base for Material Electrical Properties. . . . .	102
7.5 Effect of Off-Normal Solar Incidence on Thermal/Optical Performance . . . . .	102
7.6 Effect of Diffuse Sunlight on Thermal/Optical Performance . . .	103
7.7 Effect of Array Perforations on Cooling Effectiveness . . . . .	103
7.8 Effect of Neighboring Modules in Array Field on Thermal/ Optical Performance . . . . .	104
REFERENCES. . . . .	105
Appendix A - Material Properties. . . . .	107
Appendix B - Nomenclature . . . . .	131
Appendix C - Solar Spectrum for Air Mass 1.5. . . . .	136
Appendix D - Sunlight Concentration in Flat-Plate Photovoltaic Modules. .	142
Appendix E - Comparison of Methods for Solving Multireflection Radiation Problems in Single-Layer Thin Films. . . . .	154
Appendix F - Life Cycle Cost . . . . .	162

## LIST OF ILLUSTRATIONS

<u>Figure</u>		<u>Page</u>
2-1	Construction Elements of Photovoltaic Modules . . . . .	5
2-2	Plan View of Module Showing Cell Arrangement. . . . .	8
2-3	Module Placement in an Array Field. . . . .	9
3-1	Dimensionless Deflection at Center of Module versus Load Intensity Factor for Uniformly-Loaded, Simply-Supported Rectangular Plates. . . . .	14
3-2	Stress Intensity Factor (SIF) versus Load Intensity Factor (LIF) Showing Composite Curves of the Larger of the Maximum Positive Principal Stresses on Plate (Center Bottom or Top Surface Near Corner). . . . .	15
3-3	Finite Element Model for Stiffening Rib Studies . . . . .	17
3-4	Finite-Element Structural Model for Determination of Stresses in Module Construction Elements in Vicinity of a Centrally-Located Cell. Stresses Are Due to Normal Pressure Load on Module Surface. . . . .	20
3-5	Cell Stress versus Pottant Thickness for 50 psf Uniform Pressure Load (Tempered-Glass Superstrate Module) . . . . .	22
3-6	Cell Stress versus Pottant (E=1000 psi) Thickness for 50 psf Uniform Pressure Load (Wood-Product Substrate Module) . . . . .	23
3-7	Cell Stress versus Pottant (E=1000 psi) Thickness for 50 psf Uniform Pressure Load (Steel Substrate Module). . . . .	24
3-8	Structural Model for Determination of Cell Stress as Function of Location in Module Subjected to a 100°C Temperature Excursion . . . . .	26
3-9	Cell Stress versus Pottant Thickness for a 100°C Temperature Excursion (Glass Superstrate Module). . . . .	27
3-10	Cell Stress versus Pottant Thickness for a 100°C Temperature Excursion (Wood-Product Substrate Module) . . . . .	29
3-11	Cell Stress versus Pottant Thickness for a 100°C Temperature Excursion (Steel Substrate Module). . . . .	30
3-12	Cell Stress versus Pottant Thickness for a 100°C Temperature Excursion (Aluminum Substrate Module) . . . . .	31
4-1	Series Resistance Model for Determination of Electrical Isolation Characteristics of Photovoltaic Modules . . . . .	36
4-2	Series Capacitance Model for Determination of Electric Isolation Characteristics of Photovoltaic Modules . . . . .	38



## LIST OF ILLUSTRATIONS (Continued)

<u>Figure</u>		<u>Page</u>
4-3	Thickness of Pottant Above Cell versus Top Cover Thickness for $V_0 = 3000$ Volt DC and Top Cover Dielectric Strength = 500 Volt/mil. . . . .	43
4-4	Thickness of Pottant Above Cell versus Top Cover Thickness for $V_0 = 3000$ Volt DC and Top Cover Dielectric Strength = 1000 Volt/mil. . . . .	44
4-5	Thickness of Pottant Above Cell versus Top Cover Thickness for $V_0 = 3000$ Volt DC and Top Cover Dielectric Strength = 3000 Volt/mil. . . . .	45
4-6	Thickness of Pottant Above Cell versus Top Cover Thickness for $V_0 = 3000$ Volt DC and Top Cover Dielectric Strength = 5000 Volt/mil. . . . .	46
4-7	Thickness of Pottant Above Cell versus Top Cover Thickness for Korad and Polyurethane, PNBA, and EPR . . . . .	47
4-8	Thickness of Pottant Above Cell versus Top Cover Thickness for Korad, PVC Platisol, and Silicone Acrylic Copolymer. . . .	48
5-1	Solar Spectral Irradiance for Different Air Mass Values, Assuming U.S. Standard Atmosphere, 20 mm of Precipitable Water Vapor, 3.4 mm of Ozone, and Very Clear Air. . . . .	51
5-2	Definition of Air Mass Ratio. . . . .	53
5-3	Wavelength Dependence of Solar Cell Power Conversion Efficiency. . . . .	54
5-4	Reflection and Refraction at the Interface Between Two Dielectric Materials with Different Indices of Refraction . . .	56
5-5	Reflectivity from Interface Between Two Materials with Different Indices of Refraction . . . . .	57
5-6	Nomenclature for Antireflection Coating . . . . .	58
5-7	AR-Coating Reflectance versus Wavelength for Coating Optimized for Air/Silicon Interface . . . . .	60
5-8	AR-Coating Reflectance versus Wavelength for Coating Optimized for Pottant/Silicon Interface . . . . .	61
5-9	Simplified Model of Texturized Cell Surface . . . . .	63
5-10	Radiant Energy Fluxes at a Surface. . . . .	64
5-11	Percentage of Solar Radiation in Spectral Band $0-\lambda$ for Air Mass One, U.S. Standard Atmosphere, 20 mm Precipitable Water Vapor, and 3.4 mm Ozone . . . . .	68
5-12	Radiosity-Irradiation Network for Front Cover, Transparent Pottant, and Solar Cell . . . . .	71
6-1	Thermal Network for Encapsulated Photovoltaic Cell. . . . .	77
6-2	Energy Balance for Glass Superstrate Module with Amorphous Silicon Cells . . . . .	88
6-3	Energy Balance for Glass Superstrate Module with Polycrystalline Silicon Cells . . . . .	89

# LIST OF ILLUSTRATIONS (Continued)

<u>Figure</u>		<u>Page</u>
6-4	Energy Balance for Glass Superstrate Module with Single Crystal Silicon Cells . . . . .	90
6-5	Energy Balance for Steel Substrate Module with Single-Crystal Silicon Cells . . . . .	91
6-6	Energy Balance for Wood-Product Substrate Module with Single-Crystal Silicon Cells. . . . .	92
6-7	Open-Circuit Cell Temperature versus Backside Emissivity for a Glass Superstrate Module. . . . .	97
6-8	Open-Circuit Cell Temperature versus Thermal Resistance (Cell-to-Backside) for a Glass Superstrate Module . . . . .	98
A-1	Fraction of 1-Minute Load Duration Breakage Stress For Glass versus Load Duration. . . . .	110
A-2	Fraction of Breakage Strength of 1.0 Meter Square Glass Plates versus Plate Area. . . . .	111
A-3	Recommended Design Values for Breakage Strength versus Probability of Failure for a One Meter Square, Simply-Supported, Glass Plate Subjected to a Uniform Normal Pressure Load of 1-Minute Duration. . . . .	112
A-4	Transmittance and Reflectance Plus Transmittance versus Wavelength for Korad. . . . .	116
A-5	Transmittance versus Wavelength (.2 $\mu$ -1.2 $\mu$ ) for Tedlar . . . . .	117
A-6	Transmittance versus Wavelength (3 $\mu$ -15 $\mu$ ) for Tedlar . . . . .	118
A-7	Transmittance and Transmittance Plus Reflectance versus Wavelength for No-Iron Glass. . . . .	119
A-8	Transmittance and Transmittance Plus Reflectance versus Wavelength for Medium-Iron Glass. . . . .	120
A-9	Transmittance and Transmittance Plus Reflectance versus Wavelength for High-Iron Glass. . . . .	121
A-10	Transmittance and Transmittance Plus Reflectance versus Wavelength for EVA. . . . .	122
A-11	Transmittance and Transmittance Plus Reflectance versus Wavelength for EVA/Craneglas. . . . .	123
A-12	Transmittance Plus Reflectance versus Wavelength for White-Pigmented EVA . . . . .	124
A-13	Transmittance and Transmittance Plus Reflectance versus Wavelength for Polyurethane . . . . .	125
A-14	Transmittance and Transmittance Plus Reflectance versus Wavelength for PVC Plastisol. . . . .	126
D-1	Slice Through Infinite Module Consisting of Semi-Infinite Cell and Semi-Infinite White Reflecting Region. . . . .	144
D-2	Enhancement Effect Due to Multiple Internal Reflections in Module Configuration Shown in Figure D-1. . . . .	145

## LIST OF ILLUSTRATIONS (Continued)

<u>Figure</u>		<u>Page</u>
D-3	Slice Through Infinite Area Consisting of Two Semi-Infinite Solar Cells Separated by an Infinitely-Long, White Reflecting Strip. . . . .	145
D-4	Enhancement Effect Due to Multiple Internal Reflections in the Module Configuration Shown in Figure D-3. . . . .	147
D-5	Circular Solar Cell Surrounded by Infinite White Reflecting Region Under Top Cover of Thickness $t$ . . . . .	147
D-6	Average Enhancement Over Entire Cell for Circular Cell Surrounded by Infinite Reflecting Region. . . . .	148
D-7	Total Internal Reflection for Two-Layer Encapsulation System. .	151
D-8	Section of Module Using Square Solar Cells. . . . .	152
D-9	Increase in Irradiation as a Function of Reflecting Strip Width for Results Shown in Figure D-1 . . . . .	152
E-1	Radiant Energy Fluxes in a Transparent Thin Film. . . . .	156
E-2	Path of Light Ray in Single-Layer Thin Film . . . . .	159
F-1	Life Costing Algorithm . . . . .	163

## LIST OF TABLES

<u>Table</u>	<u>Page</u>
2-1 Percent Occurrence of Different Failure Modes for Photovoltaic Modules in a Terrestrial Environment. . . . .	11
3-1 Thickness, Stress, and Maximum Deflection of Load-Bearing Member for a 1.2-Meter Square Module and a Uniform 50 psf Pressure Load . . . . .	16
3-2 Stiffening Rib Concepts for Wood and Porcelainized Steel Substrate Modules . . . . .	18
4-1 Minimum Thickness of Pottant Under Cell to Withstand 3000 Volts DC for Glass Superstrate Modules . . . . .	41
5-1 Values of Conversion Efficiencies for Silicon Solar Cells . . .	63
5-2 Wavelengths at 5 Percent Intervals for Total Solar Irradiation in Spectral Region 0 to $\lambda$ : Air Mass One, U.S. Standard Atmosphere, 20mm Precipitable Water Vapor, 3.4mm Ozone, $\alpha = 0.66$ , $\beta = 0.085$ . . . . .	69
6-1 Summary of Encapsulation System Parameters Studied for Superstrate and Substrate Modules . . . . .	83
6-3 Thermal/Optical Performance of Glass Superstrate Modules with Silicon Cells . . . . .	84
6-4 Thermal/Optical Performance of Wood-Product Substrate Modules With Silicon Cells. . . . .	85
6-5 Thermal/Optical Performance of Steel Substrate Modules with Silicon Cells . . . . .	86
6-6 Thermal/Optical Performance of Substrate Modules with Texturized and/or AR-Coated Silicon Cells . . . . .	93
6-7 Thermal/Optical Performance of Superstrate and Substrate Modules Using Different Pottants. . . . .	95
A-1 Allowable Breakage Stresses for 1.2 Meter x 1.2 Meter Glass Plates Subject to Wind Pressure and Thermal Cyclic Loading. . .	113
A-2 Structural Properties of Silicon Solar Cells, Glass, Wood Product, and Steel. . . . .	113
A-3 Electrical Properties for Wood Product, Different Pottants, and Organic Cover Films . . . . .	115
A-4 Spectral Absorption Coefficients for Glass, Tedlar, and Korad . . . . .	127

# LIST OF TABLES (Continued)

<u>Table</u>		<u>Page</u>
A-5	Spectral Absorption Coefficients for EVA, EVA/Craneglas, PVC Plastisol, and Polyurethane . . . . .	128
A-6	Refractive Index for Module Construction Materials. . . . .	130
A-7	Thermal Conductivity of Typical Module Construction Materials . . . . .	130
C-1	Solar Spectral Irradiance - Standard Curves for 0.2 Ground Albedo and a Horizontal Surface . . . . .	138
C-2	Solar Spectral Irradiance - Standard Curves for 0.2 Ground Albedo and a 37° Tilted Surface . . . . .	140
F-1	Costing Assumptions . . . . .	164
F-2	Task III Design Concepts . . . . .	164
F-3	Module Costing . . . . .	165
F-4	Initial Array Costing . . . . .	165
F-5	Life Cycle Costs . . . . .	166

## 1.0 SUMMARY

The results, as yet unverified, of the thermal, optical, structural, and electrical isolation analyses described in this report indicate that the following items are major factors in the design of terrestrial photovoltaic modules:

- Aluminum is unsuitable as a substrate material.
- Pottant should be elastomeric (i.e. modulus of elasticity less than 2500 psi).
- Cell stress increases with increasing pottant modulus of elasticity for both uniform pressure load and temperature excursion conditions.
- Cell stress decreases with increasing pottant thickness in modules containing elastomeric pottant ( $E < 2500$  psi).
- Finned substrate modules require less material and are structurally stiffer than unribbed substrate modules.
- Cell stress is insensitive to pottant thickness in ribbed, wood-product substrate modules containing elastomeric pottant when module is subjected to uniform pressure loads.
- Cell stress is insensitive to pottant thickness in wood-product substrate modules containing elastomeric pottants when the module undergoes a temperature excursion.
- Pottant thickness between cell and load-bearing member is determined by 100°C temperature excursion criteria for steel substrate and glass superstrate modules.

- Pottant thickness between cell and load-bearing member is determined by 50 psf pressure-load criteria for wood-product substrate modules.
- Required thickness of porcelainized steel substrate to withstand 50 psf pressure load is more than twice the thickness of uncoated steel substrate for the same load.
- Electrical isolation requirement and temperature excursion criterion are equally important in determination of pottant thickness between cell and load-bearing member for steel substrate modules.
- Pottant thickness between cell and load-bearing member of unribbed, wood-product substrate modules is determined by structural deflection criterion.
- Electrical isolation requirement determines necessary pottant thickness between cell and front cover of substrate modules.
- Cell temperature is not strongly affected by either thickness or thermal conductivity of pottant.
- Infrared emissivity of module surfaces exert a significant influence on cell temperature.
- Antireflection coating is most effective on cell surface.
- Antireflection coating on outer surface of transparent superstrate is not as effective as an antireflection coating on cell surface.
- Antireflection coating on both sides of transparent superstrate is not as effective as an antireflection coating on outer surface only.
- Yellowing or discoloration of pottant results in decrease in electric power output from module.
- Presence of Craneglas (a nonwoven glass mat manufactured by Crane and Co., Inc.; Dalton, MA) in the pottant layer on the sun side of a cell does not significantly reduce the transmittance of sunlight through the pottant.

During this phase of the program, it was found that mechanical defects in the different layers of an encapsulation system would strongly influence the minimum pottant thickness required for electrical isolation. In addition, the results of an extensive literature survey indicate that structural, optical and electrical properties are heavily influenced by the presence of moisture. These items have been identified as technology voids and are discussed more completely in Section 7.

All analyses described in this report are for a 1.2 meter square module using 10.2 cm (4-inch) square cells placed 1.3 mm apart as shown in Figure 2-2. Most of the analyses were performed for environments specified in References 9 and 10 (i.e. LSA module qualification requirements). For example, sizing of the structural support member of a module was determined for a uniform, normal pressure load of 50 psf. This load corresponds to the pressure difference generated between the front and back surface of a module by a 100 mph wind. Thermal and optical calculations were performed for a wind velocity of 1 meter/sec parallel to the ground and for a module tilt (relative to the local horizontal) of  $37^{\circ}$ . Placement of a module in a typical array field is illustrated in Figure 2-3.



## 2.0 INTRODUCTION

The role of the encapsulation system in a photovoltaic module is to package, protect, and support the solar cells and electrical interconnects of the module. Construction elements of a typical encapsulation system for the accomplishment of these goals are illustrated in Figure 2-1.

The rational design of these construction elements is the subject of this report. As might be expected, the design of encapsulation systems for flat-plate photovoltaic modules requires tradeoffs between conflicting design requirements. For example, structural requirements favor a thick layer of pottant between the cell and cover glass (i.e. the load-bearing member) of a glass superstrate module; on the other hand, optical and thermal requirements favor a thin pottant layer for this type of module. In the past, design tradeoffs to satisfy these requirements have been carried out in a cut-and-try fashion with resultant heavy investments in time and money.

Presented in the following sections of this report are detailed investigations of the thermal, optical, structural, and electrical isolation aspects of photovoltaic module design for terrestrial applications. The goals of these investigations were basically three-fold: (1) systematize the mathematical models to be used in each of the technical areas with special attention devoted to determination of module performance sensitivity to thickness and physical properties of candidate encapsulation construction elements, (2) establish design/performance trends that will be useful to the module designer, and (3) establish design priorities; that is, identify items that exert the strongest influences on module electrical power output, manufacturing cost, and safety.

Relevant assumptions and limitations of the mathematical models are discussed in detail. These models have been developed so as to maintain as

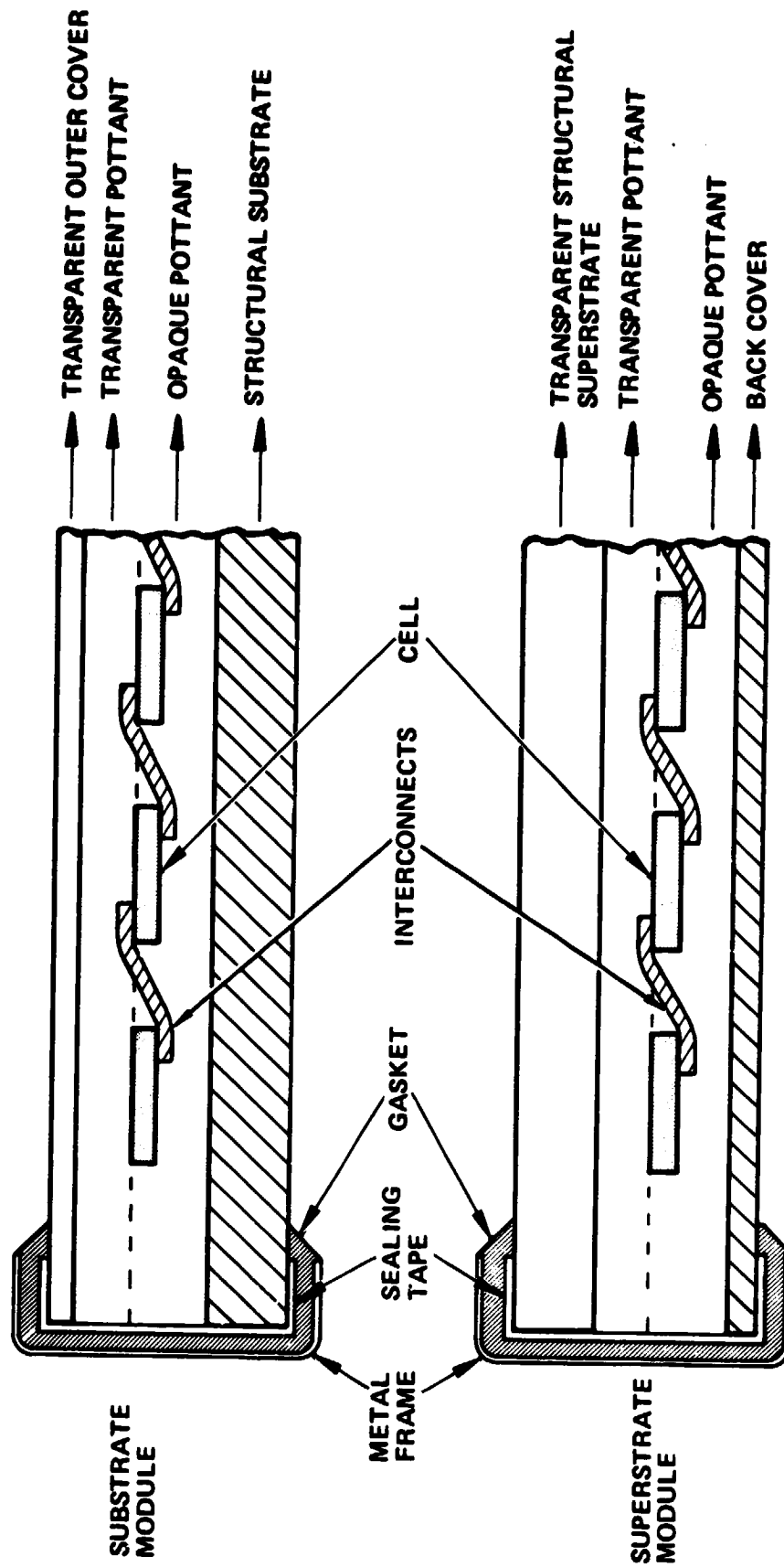


Figure 2-1. Construction Elements of Photovoltaic Modules

much flexibility as possible. For instance, the thermal and optical models were developed in such a way that a wide variety of cell types, illumination sources, pottant and cover materials, and AR (antireflection) coatings could be easily and quickly evaluated.

Two types of modules are investigated in this report:

- Superstrate module in which structural support is provided by a transparent load-bearing member on the sun side of the cells
- Substrate module in which structural support is provided by an opaque backing material behind (i.e. on the anti-sun side) the cells

The arrangement of construction elements for each module type is illustrated in Figure 2-1. Structural support for the cells is provided by the structural substrate in a substrate module and by the transparent superstrate in a superstrate module. The pottant protects the cells and the cell interconnects from the environment. The transparent superstrate in a superstrate module and the transparent front cover in a substrate module help protect the pottant by screening out some of the ultraviolet radiation in the solar spectrum. The superstrate and front cover also provide protection against soiling and abrasive action by wind-blown sand and dirt. Sealing tape around the edge of the module prevents moisture infiltration into the pottant. The gasket cushions the module against shock due to rough handling and also permits the module to expand and contract during the daily heating and cooling cycle. The back cover on a superstrate module protects the pottant from the environment and in certain cases (see Section 6) enhances module cooling. The edge frame is used to attach the module to the array. Some typical materials used for these construction elements are listed below. Comprehensive lists of materials are found in references 4 and 5.

- Superstrate modules
  - Transparent structural superstrate: glass
  - Back cover: white Mylar, aluminized Mylar
- Substrate modules
  - Structural substrate: aluminum, mild steel, porcelain-coated steel, wood product
  - Transparent outer cover: Korad, Tedlar
- Pottant (substrate, superstrate modules): ethylene vinyl acetate (EVA), ethylene propylene rubber (EPR), ethylene methyl acrylate (EMA), poly n-butylacrylate (PNBA), poly vinyl butyrol (PVB), poly vinyl chloride (PVC) plastisol
- Silicon solar cells: single crystal, polycrystalline, amorphous

Module designs incorporating these materials (as well as other materials) are discussed in detail in the following sections of this report.

All analyses described in this report are for a 1.2 meter square module using 10.2 cm (4-inch) square cells spaced 1.3 mm apart as shown in Figure 2-2. Most of the analyses were performed for environments specified in references 9 and 10 (i.e. LSA module qualification requirements). For example, sizing of the structural support member of a module was determined for a uniform, normal pressure load of 50 psf. This load corresponds to the pressure difference generated between the front and back surface of a module by a 100 mph wind. Thermal and optical calculations were performed for a wind velocity of 1 meter/sec parallel to the ground and for a module tilt (relative to the local horizontal) of 37°. Placement of a module in a typical array field is illustrated in Figure 2-3.

During the first five months of the program, significant effort was expended in reviewing module failure data provided by JPL. The purposes of this failure data review were to (1) determine the failure modes of photovoltaic modules which are amenable to solution by proper design of the encapsulation system and (2) develop a module life-prediction methodology. This methodology was to be used to design modules that have a useful life of at least 20 years. The JPL PFR (Problem/Failure Report) listing of 6 May 1980

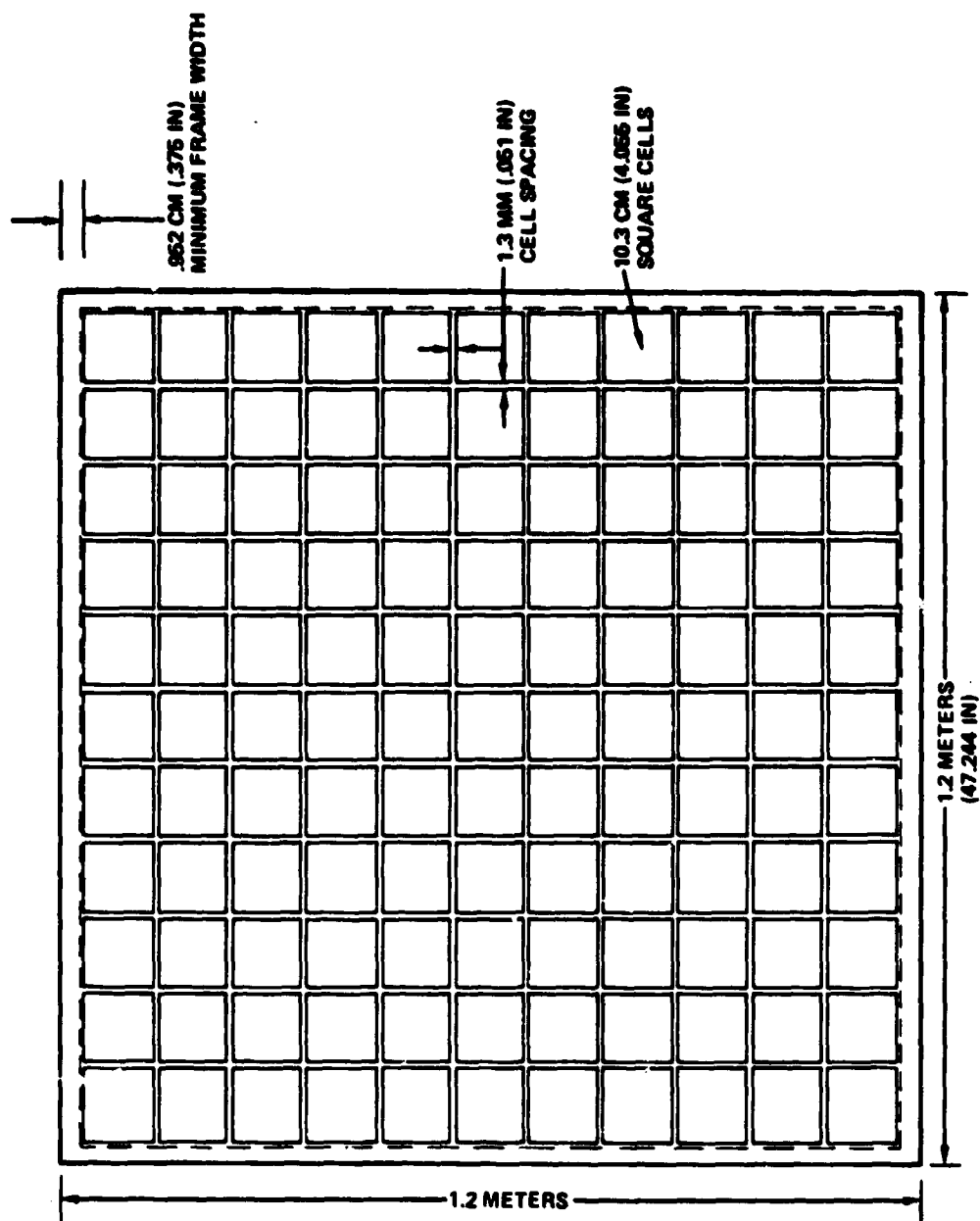


Figure 2-2. Plan View of Module Showing Cell Arrangement

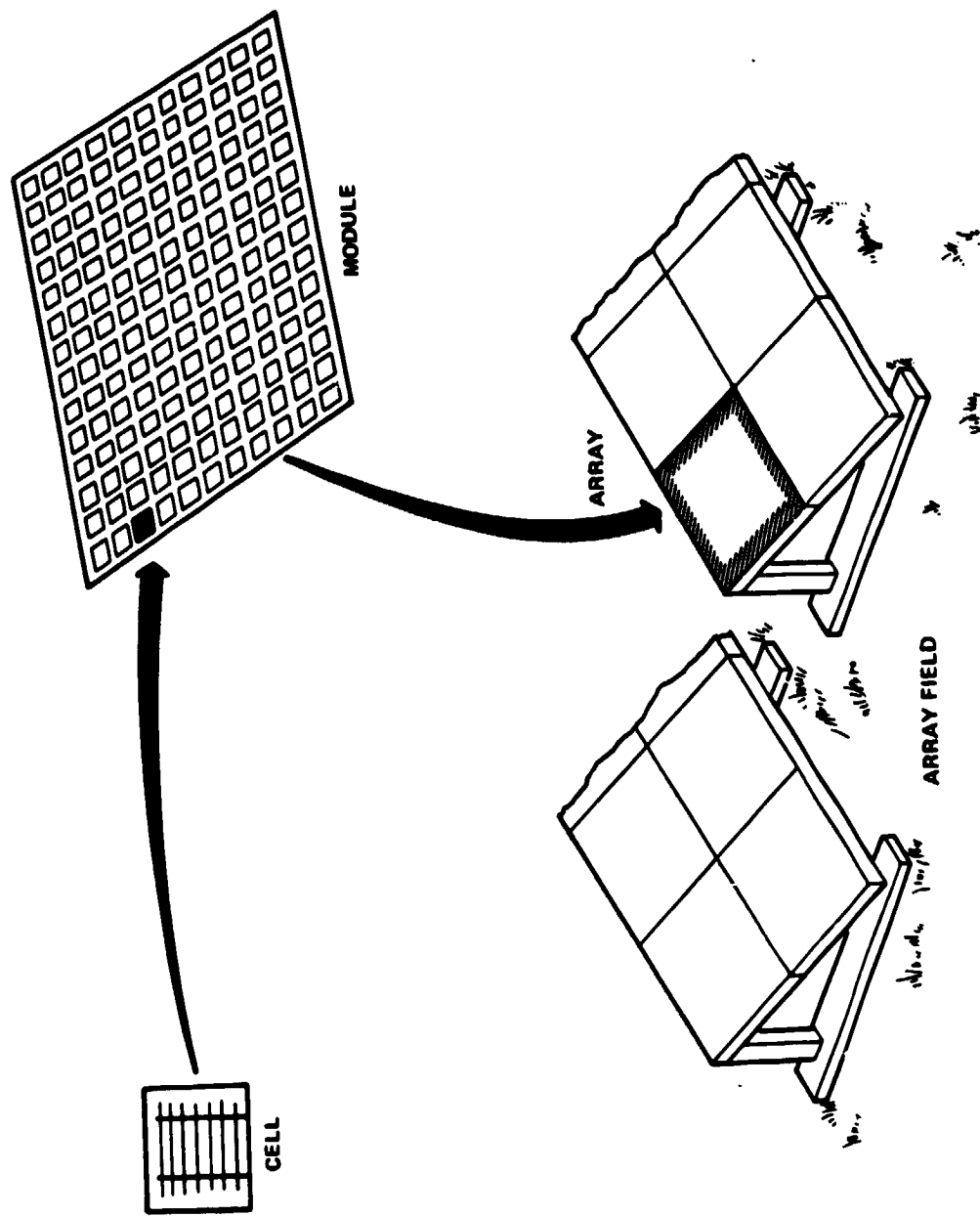


Figure 2-3. Module Placement in an Array Field

PRECEDING PAGE BLANK NOT FILMED

TABLE 2-1. Percent Occurrence of Different Failure Modes for Photovoltaic Modules in a Terrestrial Environment

Failure Modes*	Number of PFRs	Percent	Cum. Percent
Cracked Cells	320	31.2	31.2
Delamination	221	21.5	52.7
Corrosion	68	6.6	59.3
Fractured Interconnections	58	5.6	64.9
Power Degradation	42	4.1	69.0
Discoloration	39	3.7	72.7
Surface Cover Cracking	35	3.4	76.1
Bad Solder Joints	29	2.8	78.9
Excessive Air Bubbles	28	2.7	81.6
Cracked Insulators	24	2.3	83.9
Open Circuit	20	1.9	85.8
Contamination	16	1.6	87.4
Seal Separation	15	1.5	88.9
Silver Silk Screen Contacts Degraded	14	1.4	90.3
Web Interconnect Broken	12	1.2	91.5
Terminal Broken	12	1.2	92.7
Substrate Burned	11	1.1	93.8
Voltage Breakdown	10	1.0	94.8
Short Circuit	8	0.7	95.5
Pottant Leak	8	0.7	96.2
Poor Cover Bond	7	0.7	96.9
Dielectric Breakdown	6	0.6	97.5
End Channel Shrinkage	5	0.6	98.1
Epoxy Outgassing	5	0.5	98.6
Broken Strands	4	0.4	99.0
Hypalon/Hex-Laminate Damaged	4	0.4	99.4
Inadequate Mechanical Back Contact Pressures	3	0.3	99.7
UV Problem	2	0.2	99.9
Vandalism	1	0.1	100.0
Total	1,027	100.0	---

\*Based on JPL PFR listing of 6 May 1980

### 3.0 STRUCTURAL ANALYSIS

#### 3.1 INTRODUCTION

The structural integrity of a photovoltaic module must be such that the module will survive and operate in different terrestrial environments. For instance, wind blowing past the module results in a pressure difference between the front and back surfaces of the module; this pressure difference causes the module to deflect, thus imposing a stress on the fragile solar cells. Accumulation of snow and ice on the module produces the same effect. In certain geographical locations such as the Great Plains region of the United States, hail is a problem that can cause severe damage to a module\*. Diurnal and seasonal temperature cycles lead to repeated expansion and contraction of the module construction elements thus subjecting the cells and interconnects to cyclic stresses and to possible fatigue failure.

In this section of the report, methods for designing structural integrity into a module are discussed in detail. First, a method is described for determining the minimum thickness of a plane, unribbed load-bearing member. For substrate modules, a finite-element structural model is then developed to investigate ribbed load-bearing members that provide greater stiffness but require less material. A different finite-element model is then developed and used to study the sensitivity of solar cell stress to pottant thickness and modulus of elasticity. These sensitivity studies are carried out for both module deflection due to wind loads and module expansion and contraction resulting from temperature cycling. Attachment of the module to the array frame is then briefly discussed.

---

\*Analysis of hail impact loads is not considered in this report.



### 3.2 THICKNESS DETERMINATION FOR STRUCTURAL (LOAD-BEARING) MEMBER

The JPL/LSA qualification test requirements serve as the starting point for determination of the structural member thickness. These test requirements include a uniform pressure of 50 psf (pounds per square foot) normal to the plane of the module and an imposed twist of 0.25 inch per foot along one edge of the module [9, 10]\*. The 50 psf pressure load is the more severe requirement.

The results of previous analyses performed at JPL [14], as shown in Figures 3-1 and 3-2, were used to determine structural member thickness. Extensive nonlinear, finite-element analyses of simply-supported rectangular plates were used to develop the results shown in these figures. Typical thicknesses are listed in Table 3-1 for load-bearing members of substrate and glass superstrate modules subjected to a 50 psf pressure load. The minimum thickness for commercially-available tempered glass is 1/8 inch. Since the maximum allowable normal stress for tempered glass is 13000 psi (pounds per square inch), the results in Table 3-1 indicate that a 1/8-inch thick sheet of tempered glass can easily withstand a 50 psf, wind-generated pressure load. For an unribbed, wood substrate module, a 1/4-inch thick wood substrate is required to withstand a 50 psf pressure load; a normal stress of 1600 psi is the maximum allowable for wood. For an unribbed steel substrate module, a substrate thickness of 0.08 inch was chosen to yield a reasonable ( $< .75$  inch) deflection; this corresponds to a maximum stress of 12000 psi. The fragility of a porcelain coating (tensile strength = 5000 psi, see reference 1), such as that on a household stove, dictates that the maximum stress (and thus the maximum deflection) be much less than that of an uncoated steel substrate. Therefore, the thickness of a porcelainized steel substrate is more than twice that of a plain steel substrate.

When reviewing these results, it should be kept in mind that the module thickness (~0.3 inch) is small compared to the module spanwise dimension (~4 feet). The deflection of the module is expected to be greater than the module thickness; this situation leads to a spanwise "stretching" of the module, a phenomenon often referred to as "membrane action". The net effect of this

---

\*Numbers in brackets designate references at the end of this report.

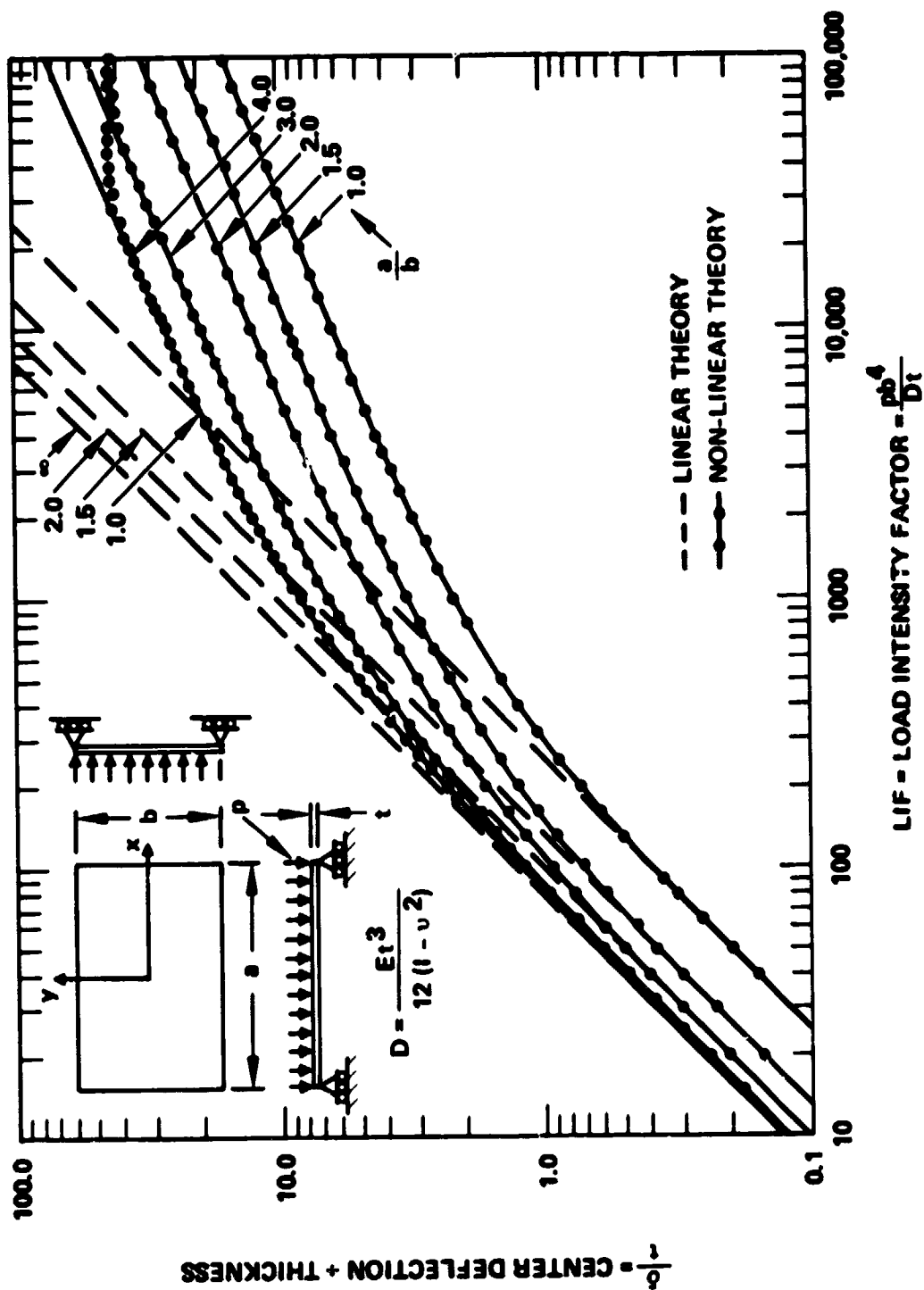


Figure 3-1. Dimensionless Deflection at Center of Module versus Load Intensity Factor for Uniformly-Loaded, Simply-Supported Rectangular Plates

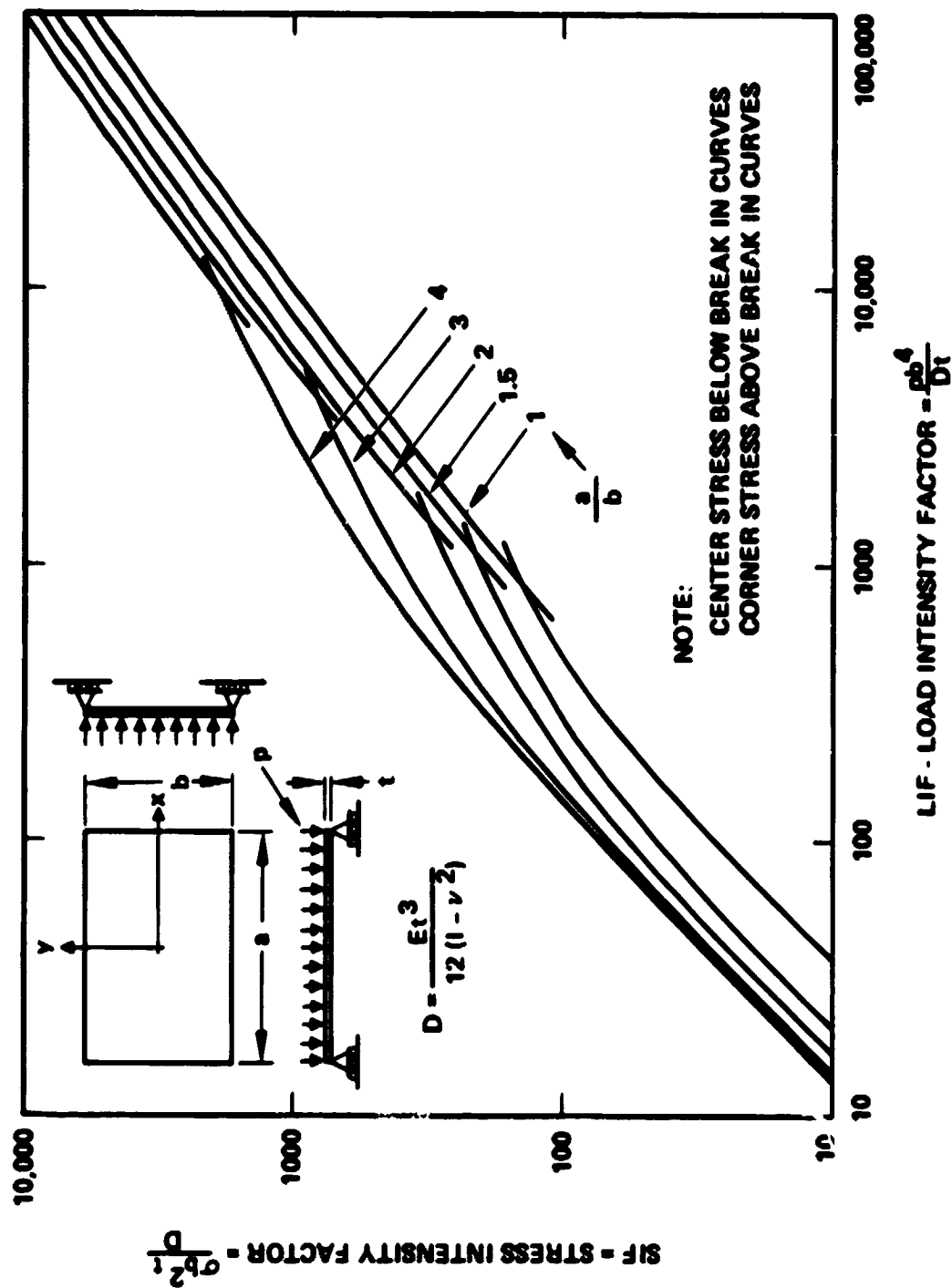


Figure 3-2. Stress Intensity Factor (SIF) versus Load Intensity Factor (LIF) Showing Composite Curves of the Larger of the Maximum Positive Principal Stresses on Plate (Center Bottom or Top Surface Near Corner)

**TABLE 3-1. Thickness, Stress, and Maximum Deflection  
of Load-Bearing Member for a 1.2-Meter  
Square Module and a Uniform 50 psf  
Pressure Load**

Module Design	Thickness, in	Maximum Deflection, in	Stress, psi
Glass Superstrate Tempered Annealed	.125	0.75	6000
	.200	0.50	3200
Wood-Product Substrate*	.25	1.4	1600
Plain Steel Substrate	.08	0.64	12000
Porcelainized Steel Substrate	.20	0.40	5000
Aluminum	.10	0.80	7000

\*Particle board such as Super Dorlux (Masonite, Corp.; Chicago, Ill.) or Duron (U.S. Gypsum Co.; Chicago, Ill.)

stretching is to reduce stresses in and deflections of the module. Linear analyses, such as those summarized in reference 17, do not account for this membrane action and thus predict higher stresses and deflections than those encountered in actual practice. Structural member thicknesses predicted on the basis of linear analysis will be greater than required and will result in a costly oversized module.

### 3.3 STIFFENING-RIB STUDIES

Through the incorporation of stiffening ribs, the weight of a substrate module can be reduced considerably (compared to unribbed substrates) without compromising module structural integrity. Using the MSC/NASTRAN computer program [15], a one-quarter symmetric model of a 1.2-meter square module, as illustrated in Figure 3-3, was developed to determine the extent of this material saving. The model consists of a 10 x 10 uniform grid of CQUAD4 elements representing the substrate and CBAR elements offset from the neutral

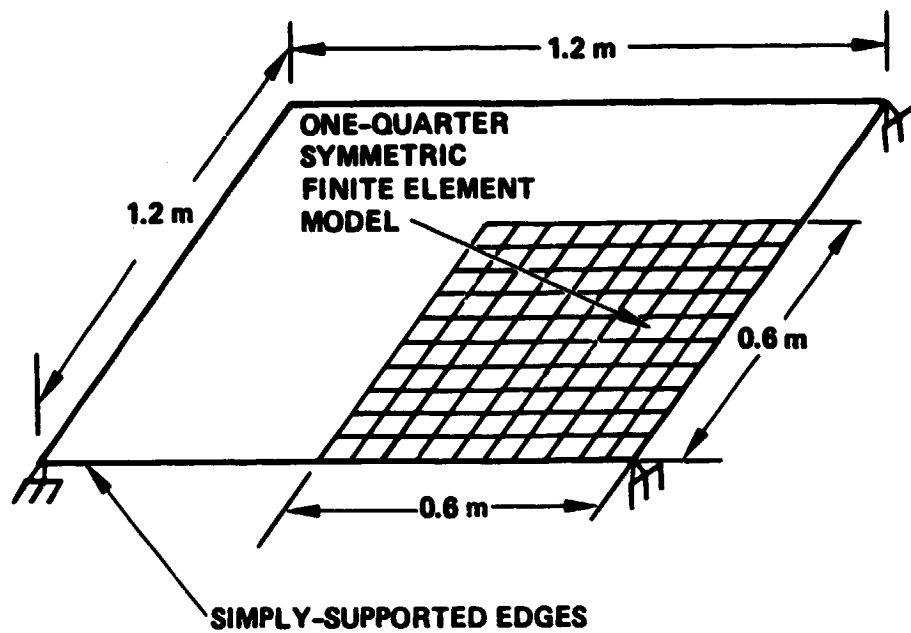


Figure 3-3. Finite Element Model for Stiffening Rib Studies

TABLE 3-2. Stiffening Rib Concepts for Wood and Porcelainized Steel Substrate Modules

Substrate	Number of Ribs and Spacing*	Rib Dimensions	Substrate Thickness	Material Savings**
Wood	5 @ 8"	2.0" x 0.40"	0.125"	20 percent
Porcelainized Steel	5 @ 8"	1.5" x 0.20"	0.080"	50 percent

\* Ribs run in one direction

\*\*Material savings relative to an unstiffened plate

plane of the substrate representing the ribs<sup>+</sup>. This model permitted easy changes of rib cross-section, spacing, and material properties. Simple support boundary conditions were stipulated along the exterior edges, and symmetric boundary conditions were imposed along the interior cut edges of the module. Deflections and stresses were determined for a uniform 50 psf pressure load normal to the plane of the module. Results of this analysis are summarized in Table 3-2. No attempt was made to optimize rib spacing and geometry.

### 3.4 POTTANT THICKNESS DETERMINATION

#### 3.4.1 Deflection/Stress Sensitivity Studies

Mechanical loads such as wind, the weight of a snow or ice layer, acceleration due to earthquakes, and imposed twist due to support settlement or misalignment generate stress in a photovoltaic module. As the module deflects under load, the resulting strain in the load-bearing member is

<sup>+</sup>CBAR and CQUAD4 refer to standard mathematical algorithms in the MSC/NASTRAN computer program. These algorithms are used to simulate the structural behavior of beams and rectangular plates respectively.

propagated through the pottant to the solar cells. The dependence of the resultant cell stresses on pottant thickness and modulus of elasticity are investigated in this section.

As mentioned in Section 3-2, a rather sophisticated analysis is required to determine module deflection due to normal pressure loads. Calculation of stresses inside a laminated structure like that of a photovoltaic module presents additional analytical complications. For example, if the pottant is stiff (i.e. has a high modulus of elasticity), the stress in the load-bearing member is amplified and transmitted thru the pottant to the cell. In other words, the module acts as a rigid beam where a plane cross section (e.g. a vertical grid line in Figure 3-4) remains plane as the module deflects. For an elastomeric or rubbery pottant, on the other hand, the stress in the load-bearing member is attenuated and transmitted thru the pottant to the cell. There are two reasons for this attenuation: (1) as the module deflects under load, the elastomeric pottant allows the cell to slide relative to the load-bearing member, and (2) the cell tends to separate, or move away from the load-bearing member as the module undergoes an out of plane displacement. These attenuation phenomena are referred to as "transverse shear flexibility" and "thickness stretch" respectively. Classical lamination theory [8], such as that used in the structural analysis of "stiff" structural composite materials, does not account for these stress attenuation phenomena. Thus, an analysis of cell stress sensitivity to pottant thickness and modulus of elasticity can be time consuming and costly.

In this section a somewhat simplistic approach is used for the sensitivity analysis. This approach combines the structural information for load-bearing member thickness found in Section 3.2 with a two-dimensional, finite-element NASTRAN model of a cell located at the center of the module where the largest deflection and stresses are expected to occur. The model consists of rectangular plate elements with symmetric boundary conditions along the center of the cell and free-edge conditions along an imaginary cut plane between adjacent cells, as shown in Figure 3-4. It is assumed that the pottant thickness is the same on both sides of the cell. This model can be viewed as a cantilever beam with the left-hand edge considered fixed and non-rotating. A one mil vertical displacement (as indicated by the arrow in Figure 3-4) is

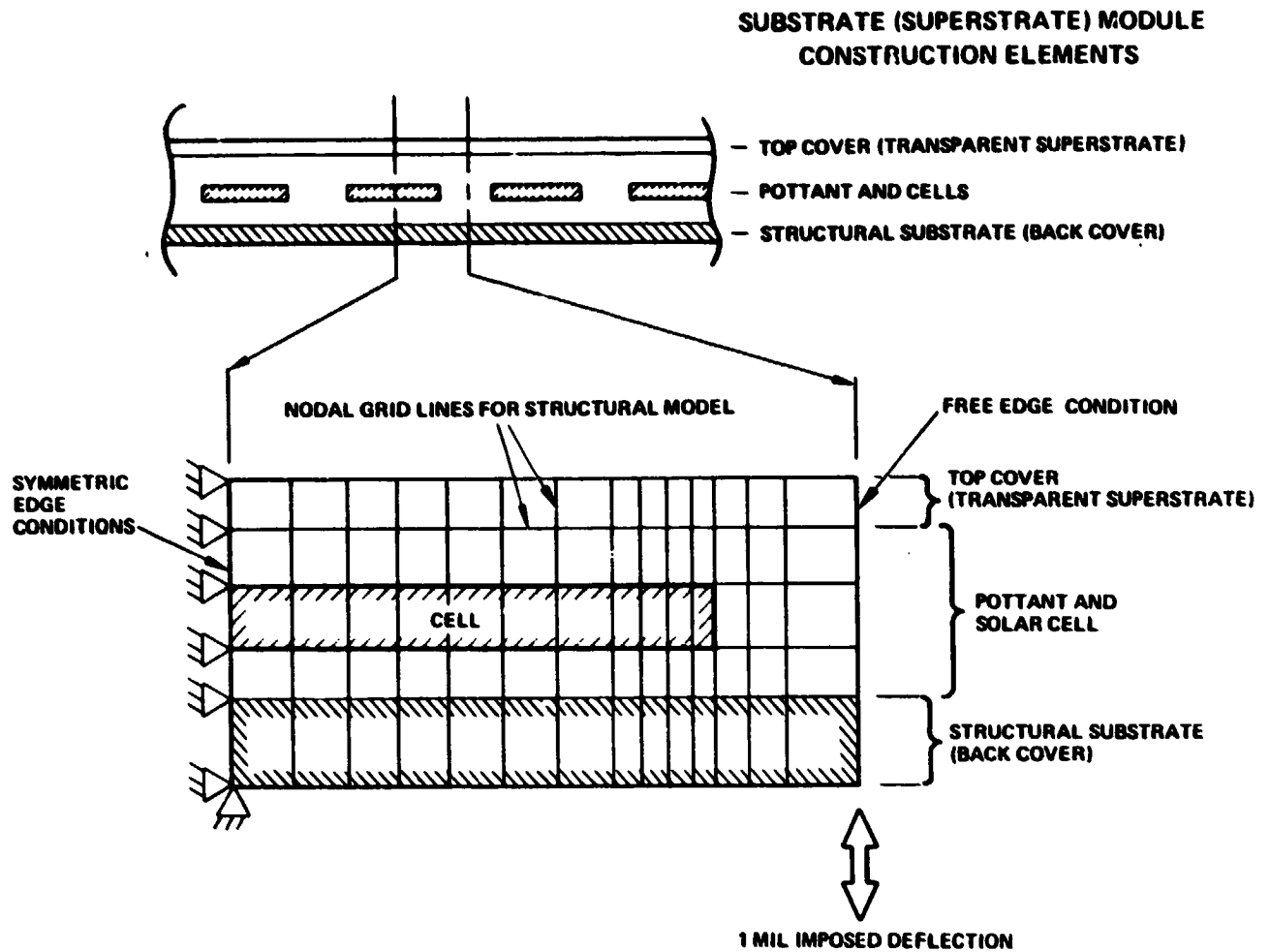


Figure 3-4. Finite-Element Structural Model for Determination of Stresses in Module Construction Elements in Vicinity of a Centrally-Located Cell. Stresses Are Due to Normal Pressure Load on Module Surface



imposed on the extreme right end of the load-bearing member, and the resulting strains in both the cell and the load-bearing member are then determined. The ratio of the strain in the cell to the strain in the load-bearing member is assumed to remain invariant with deflection of the load-bearing member. On the other hand, this strain ratio is a function of both pottant thickness and modulus of elasticity. The cell stress is then determined by multiplying the strain ratio by the appropriate stress in the load bearing member.

Results for glass superstrate and for wood-product and steel substrate modules are shown in Figures 3-5 through 3-7. Solar cell stress is plotted against pottant thickness for different values of modulus of elasticity; here, the pottant thickness refers to the thickness between the cell and the load-bearing member. In each of the figures, the dotted line at 8000 psi represents the allowable normal stress in the solar cell for fatigue loading conditions.\*

For glass superstrate modules, it is seen in Figure 3-5 that for pottant moduli less than 50 ksi (thousand pounds per square inch) the cell stress decreases as the modulus decreases or as the pottant thickness increases. This trend indicates that elastomeric pottants provide strain relief through the thickness of the module. For ethylene vinyl acetate (EVA), which has a modulus of elasticity (i.e. Young's modulus) of about 1000 psi, approximately 0.5 mils of pottant are required to maintain cell stress below the 8000 psi fatigue limit. For a "stiff" pottant with a modulus of 250 ksi, the cell stress increases as the pottant thickness increases.

The sensitivity of cell stress in wood product and steel substrate modules is shown in Figures 3-6 and 3-7, respectively. The pottant modulus of elasticity is 1000 psi in these figures. Again, it is seen that cell stress decreases as the pottant thickness increases. In Figure 3-6, cell stress is plotted for both ribbed and unribbed wood substrate modules, and it is seen that about 3 mils of pottant are required for an unribbed module. Comparable results were not calculated for aluminum substrates because (as shown in Section 3.4.2) thermal expansion and contraction of this material results in unacceptably high cell stress.

---

\*See Appendix A for determination of the allowable normal stress in solar cells.

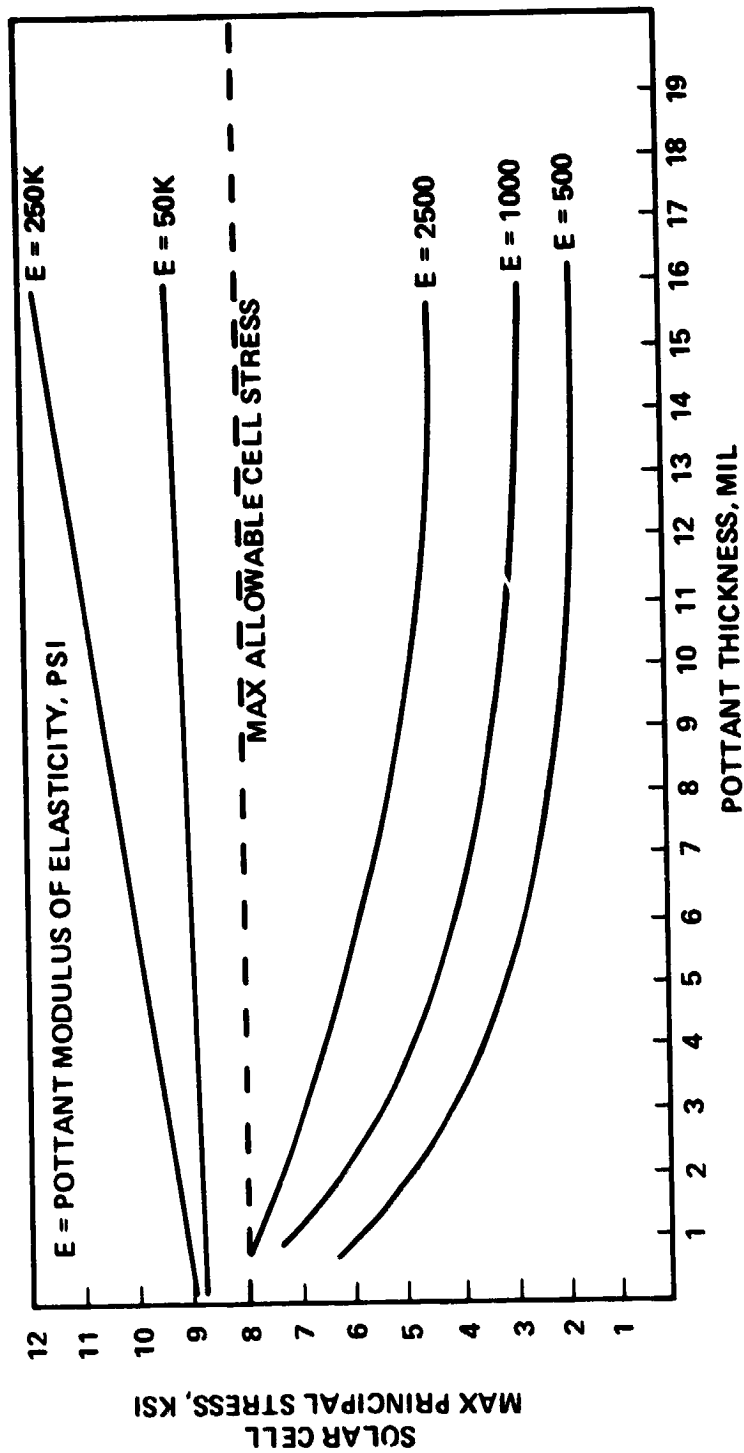


Figure 3-5. Cell Stress versus Pottant Thickness for 50 psf Uniform Pressure Load (Tempered-Glass Superstrate Module)

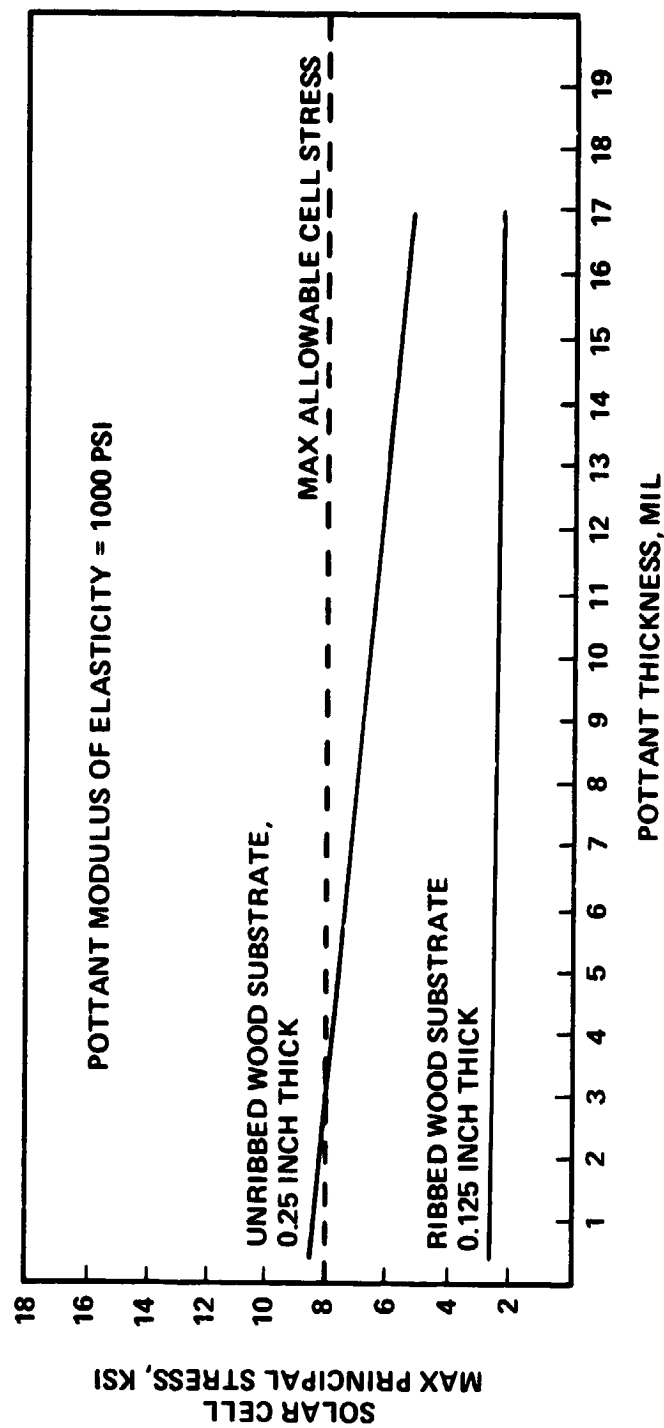


Figure 3-6. Cell Stress versus Pottant (E=1000 psi) Thickness for 50 psf Uniform Pressure Load (Wood-Product Substrate Module)

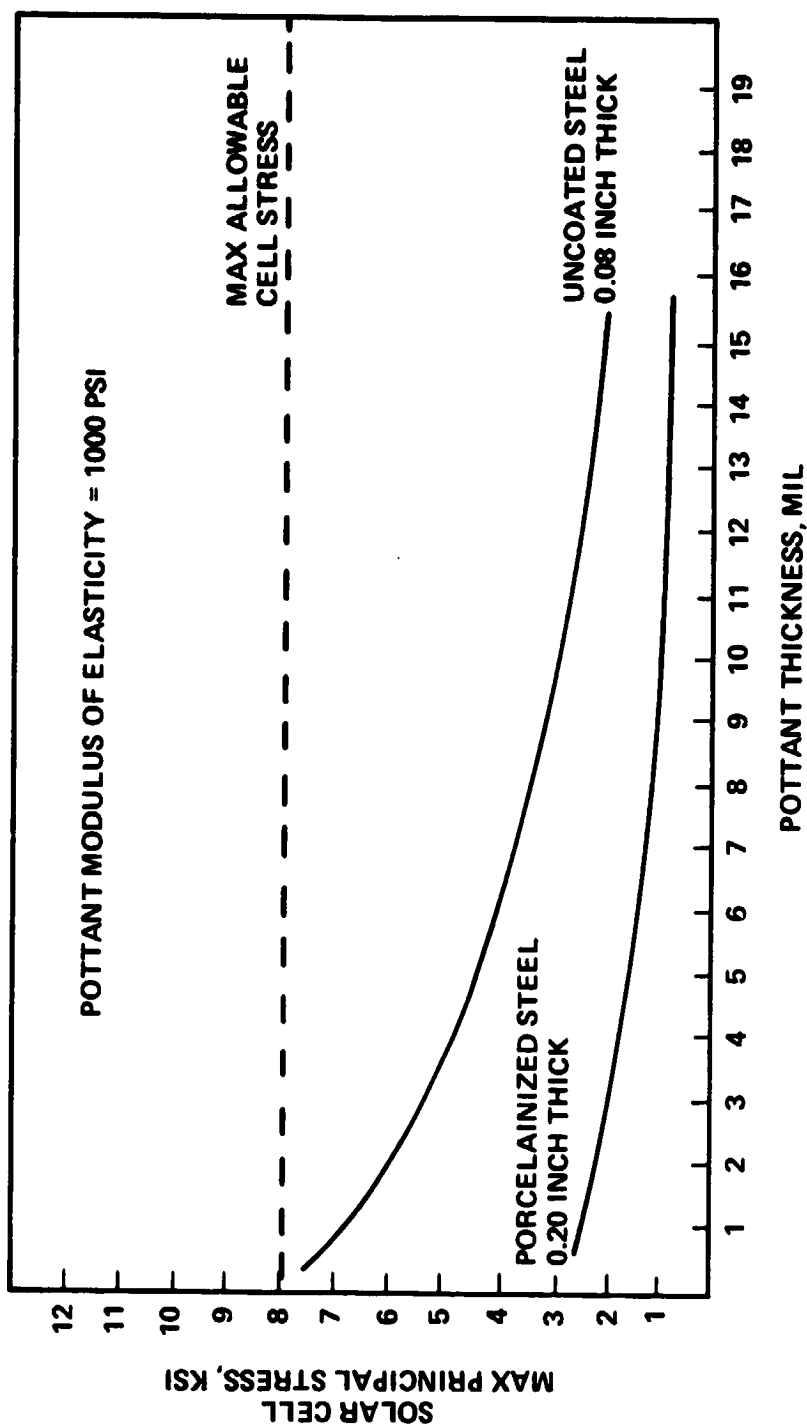


Figure 3-7. Cell Stress versus Pottant (E=1000 psi) Thickness for 50 psf Uniform Pressure Load (Steel Substrate Module)

Stiffening ribs support most of the load thus reducing the stress in the substrate. A lower stress permits the use of a thinner substrate. Cell stress is not sensitive to pottant thickness in ribbed substrate modules.

Figure 3-7 shows that for a plain, unribbed steel-substrate module about 5 mils of pottant is required to maintain cell stress below 8000 psi.

#### 3.4.2 Thermal/Stress Sensitivity Studies

A different set of analyses were performed to determine the sensitivity of cell stress to pottant modulus and thickness for temperature excursions. These analyses used the same two-dimensional NASTRAN model shown in Figure 3-4. In addition, a 5 1/2-cell, two-dimensional model as shown in Figure 3-8 was developed to determine variations in cell stress due to cell location in the module. In all cases studied, it was assumed that the module was isothermal and that the entire module experienced a 100°C temperature excursion. Temperature-invariant material properties (evaluated at 25°C) were used in these studies. However, it is known that the pottant modulus of elasticity increases with decreasing temperature. Since the intent of this analysis was to predict trends, the assumption of temperature-invariant properties was deemed acceptable. The validity of this assumption will be evaluated by means of suitable verification tests.

The results of the 5 1/2-cell model indicate that cell stress at the edge of the module is approximately ten percent higher than the cell stress at the center of the module. Therefore, in the subsequent sensitivity analysis, free-edge conditions were imposed at the boundary of the one-half cell model shown in Figure 3-4.

The results for a glass superstrate module are shown in Figure 3-9. For pottant moduli less than 10 ksi, strain relief is provided by the pottant (due to the transverse shear flexibility phenomenon mentioned previously) and cell stress decreases with increasing pottant thickness. For a pottant modulus of 1000 psi, about 1 mil is sufficient to maintain cell stress below the 5000 psi thermal-fatigue limit.\* For a modulus of 250 ksi, thermal expansion of the

---

\*See Appendix A for the determination of this limit.

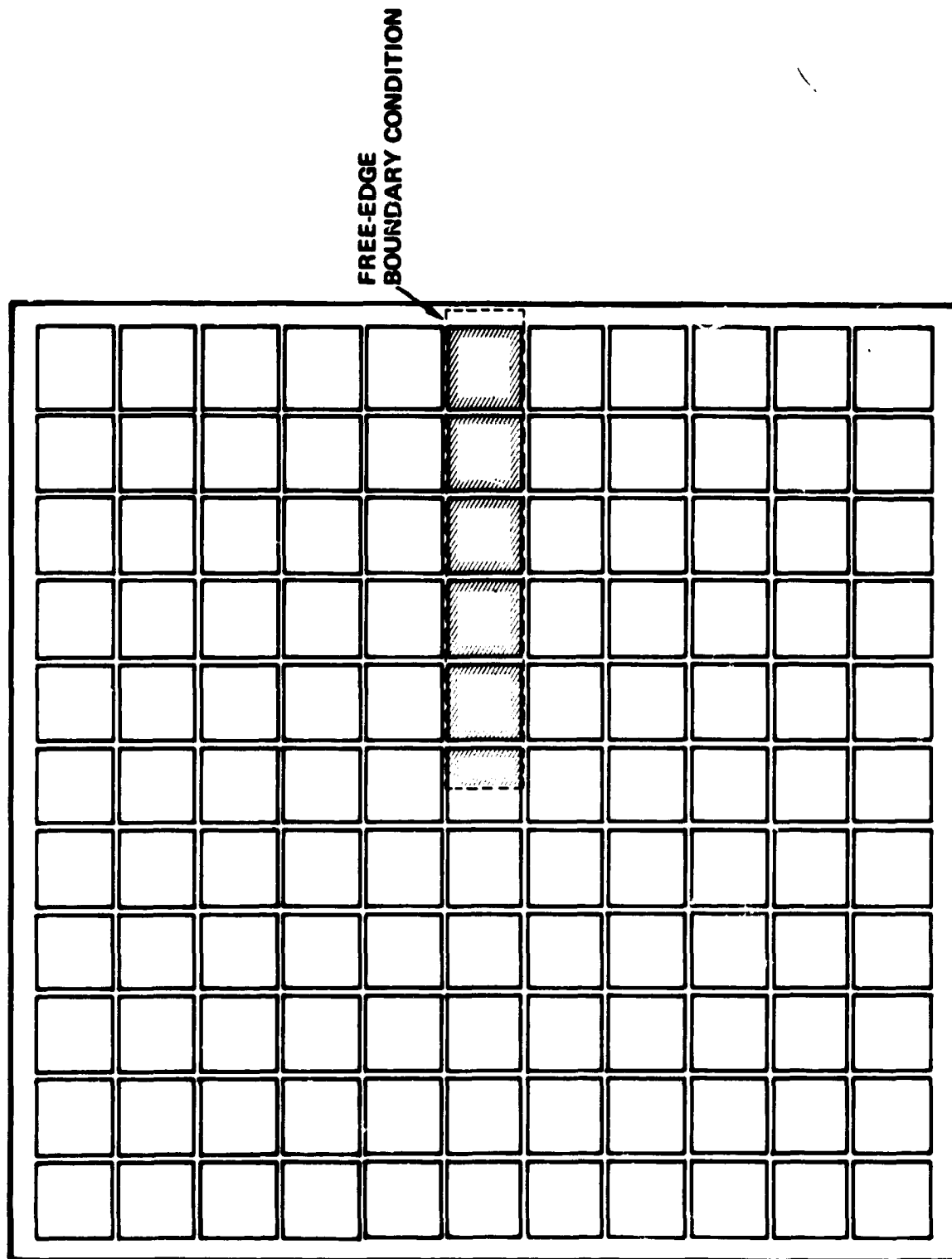


Figure 3-8. Structural Model for Determination of Cell Stress as Function of Location in Module Subjected to a 100°C Temperature Excursion

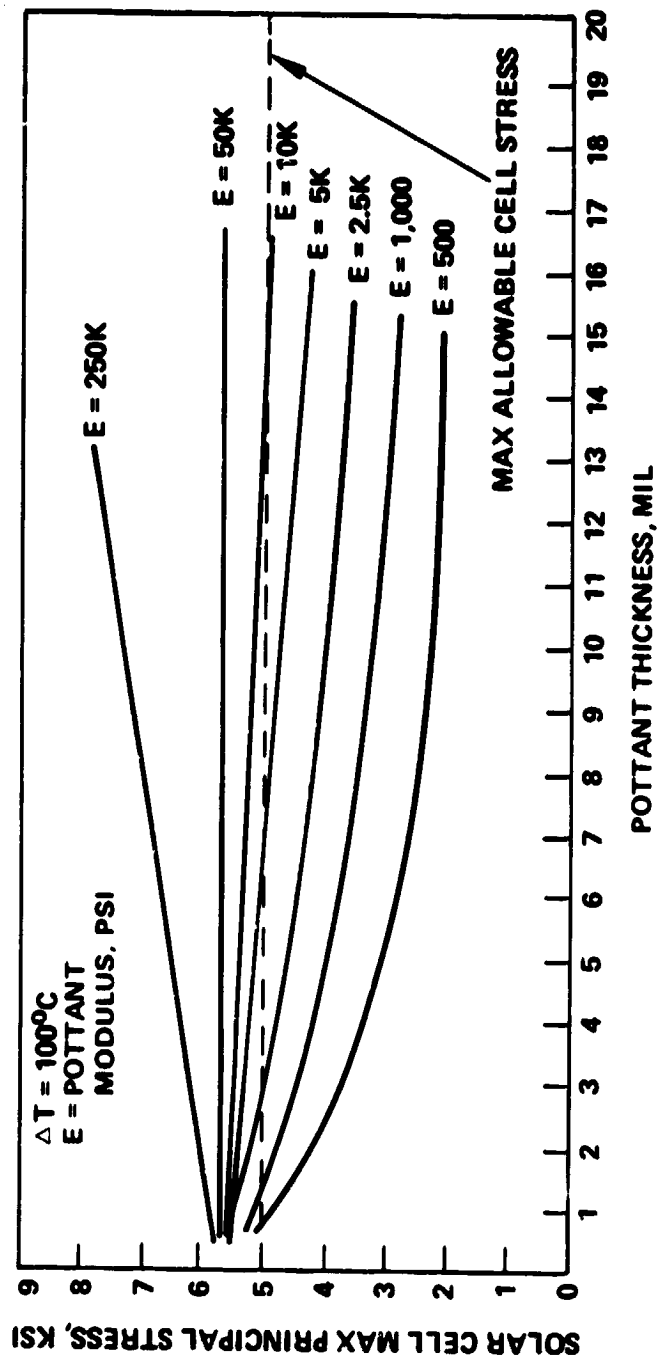


Figure 3-9. Cell Stress versus Pottant Thickness for a 100°C Temperature Excursion (Glass Superstrate Modules)

pottant gives rise to increased cell stresses as the pottant thickness is increased.

The thermal/stress sensitivity for a wood-product substrate design is shown in Figure 3-10. In this case, cell stress is not sensitive to thermal loading (i.e. a temperature excursion due to alternate heating and cooling as found in a diurnal cycle) except for relatively stiff pottants ( $E > 50$  ksi). For a pottant modulus of 250 ksi, thermal expansion of the pottant gives rise to increased cell stresses as the pottant thickness is increased.

The only value of pottant modulus considered for the steel substrate module (Figure 3-11) is 1000 psi. It is seen that 5 mils of this pottant (e.g. EVA) is sufficient to preclude thermal fatigue damage to the cell.

Results for an aluminum substrate module are shown in Figure 3-12. Here it is seen that the cell stresses resulting from temperature cycling are excessively high; hence, aluminum is not a viable material for a structural substrate.

### 3.5 EDGE ATTACHMENT CONSIDERATIONS

Edge attachment requirements were not investigated in detail. However, the following design considerations are offered as general guidelines:

- The edge attachment should provide simply-supported boundary conditions to the module. The design must be capable of transferring edge shear loads to the support structure. However, the edge should be free of significant rotational restraint.
- The edge attachment should provide thermal/mechanical uncoupling between the module and the support structure. If in-plane expansion and contraction of the module is overly constrained, excessively high stresses could result from diurnal thermal cycling.
- The edge gasket should not extrude from the edge frame when the module is subjected to a load condition.
- Stress concentrations along the edge of the module should be minimized. This is especially true for glass superstrate modules.



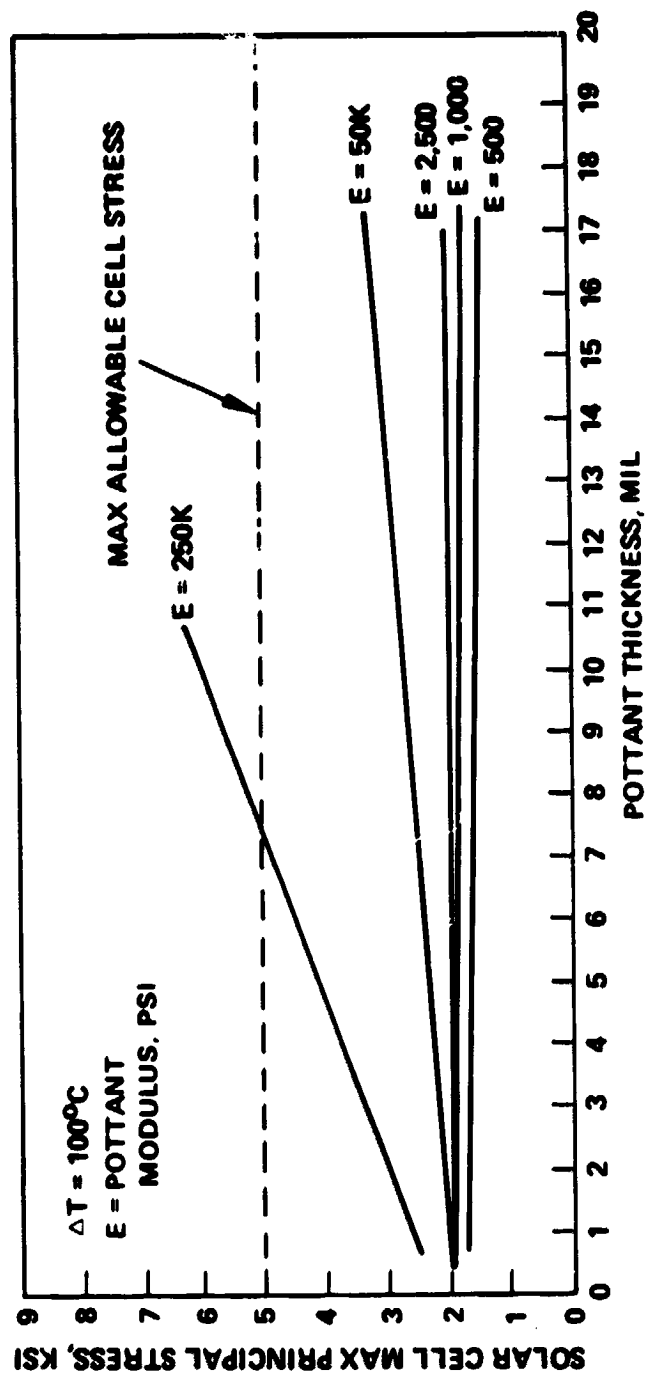


Figure 3-10. Cell Stress versus Pottant Thickness for a 100°C Temperature Excursion (Wood-Product Substrate Module)

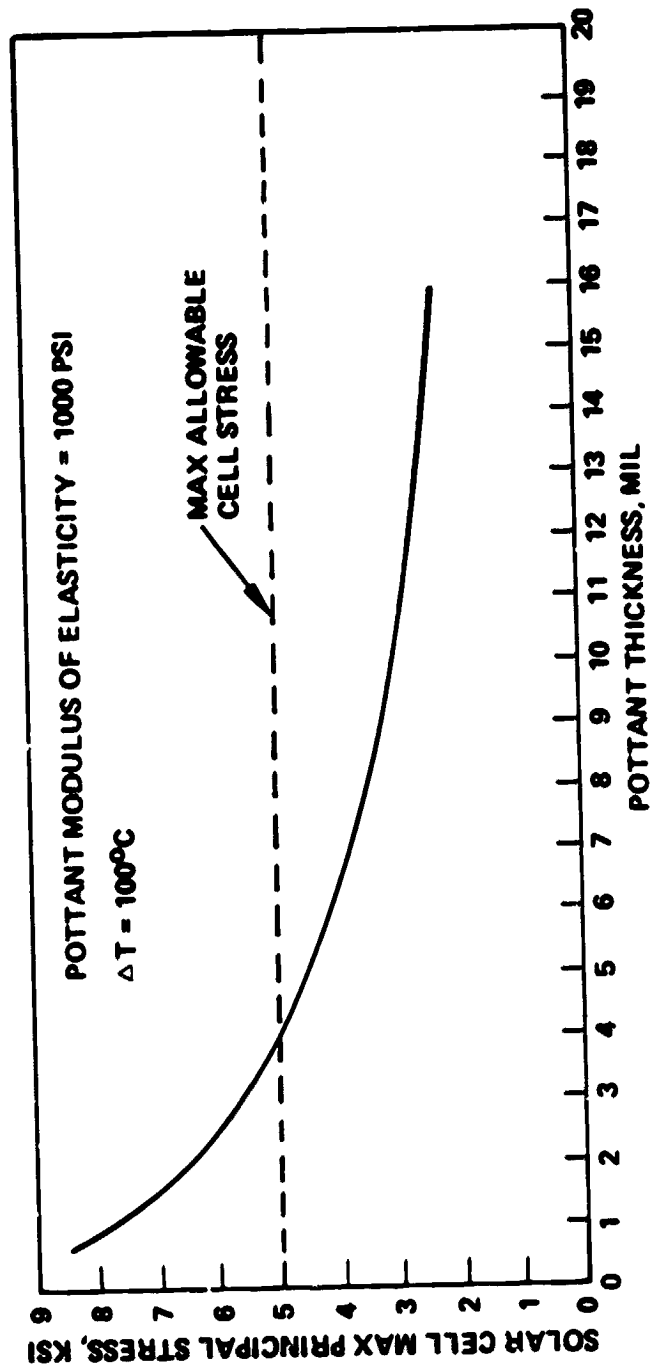


Figure 3-11. Cell Stress versus Pottant Thickness for a  $100^{\circ}\text{C}$  Temperature Excursion (Steel Substrate Module)

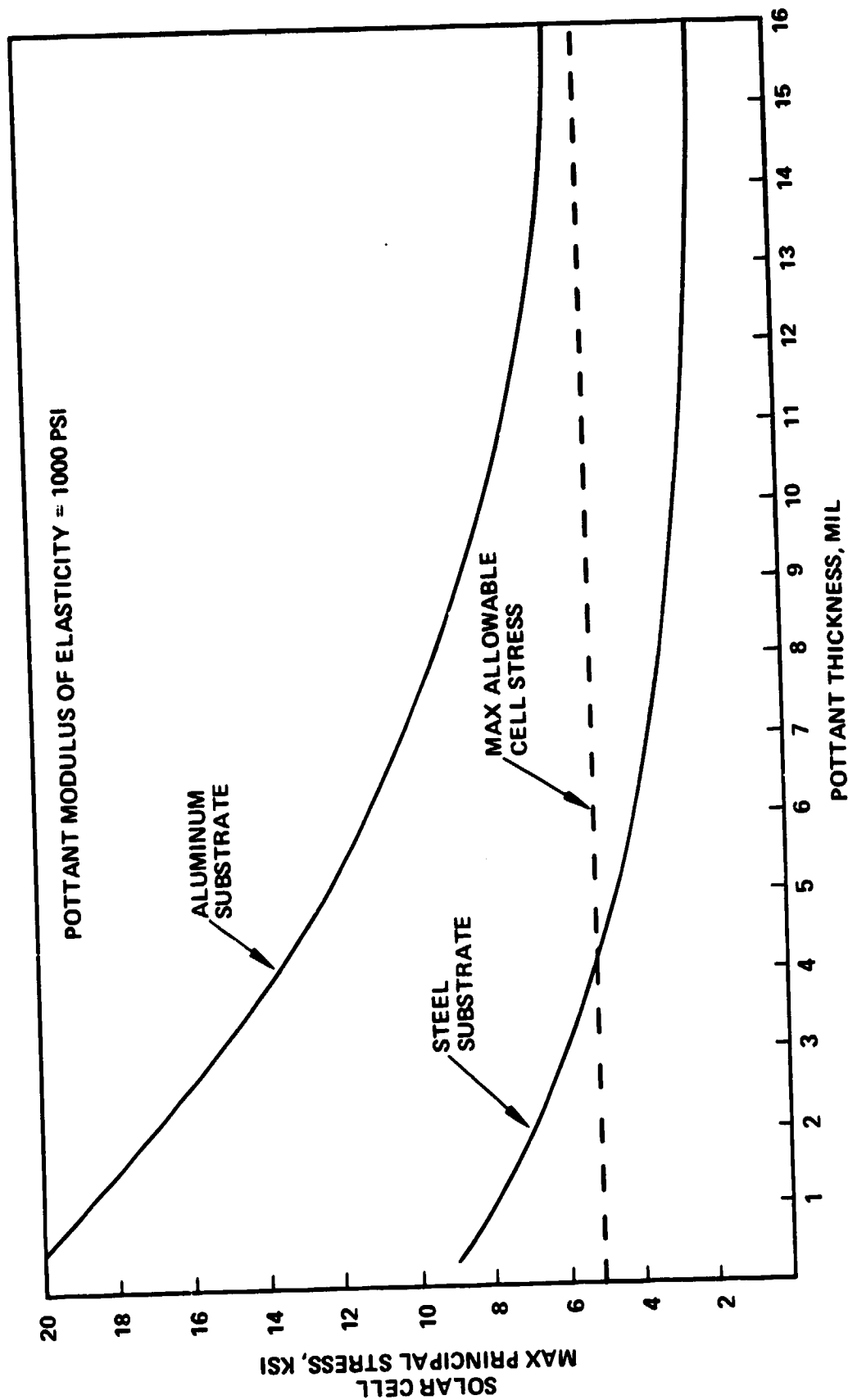


Figure 3-12. Cell Stress versus Pottant Thickness for a 100°C Temperature Excursion (Aluminum Substrate Module)

An elastomeric gasket material, such as polymerized ethylene propylene diene monomer (EPDM) is recommended for a glass superstrate module. A gasket thickness of approximately 60 mils and an edge frame bite of 3/8 inch is suggested as a starting point. It is not clear that a module with metal or wood product substrate will require an edge gasket in addition to an edge frame; however a gasket would tend to reduce damage to the edge of the module due to rough handling during transportation and installation.

### 3.6 CONCLUSIONS

The information presented in this section leads to the following conclusions regarding module structural design:

- Aluminum is unsuitable as a substrate material. An elastomeric pottant cannot relieve cell stress resulting from the large difference between thermal expansion coefficients of aluminum and silicon.
- Pottant should be elastomeric (i.e. modulus of elasticity less than 2500 psi).
- Cell stress increases with increasing pottant modulus of elasticity for both uniform pressure load and temperature excursion conditions.
- Cell stress decreases with increasing pottant thickness in modules containing elastomeric pottant ( $E < 2500$  psi).
- Finned substrate modules require less material and are structurally stiffer than unribbed substrate modules.
- Cell stress is insensitive to pottant thickness in ribbed, wood-product substrate modules containing elastomeric pottant when module is subjected to uniform pressure loads.
- Cell stress is insensitive to pottant thickness in wood-product substrate modules containing elastomeric pottant when the module undergoes a temperature excursion.
- Pottant thickness between cell and load-bearing member is determined by 100°C temperature excursion criteria for steel substrate and glass superstrate modules.

- Potant thickness between cell and load-bearing member is determined by 50 psf pressure-load criteria for wood-product substrate modules.
- Required thickness of porcelainized steel substrate to withstand 50 psf pressure load is more than twice the thickness of uncoated steel substrate for the same load.

## 4.0 ELECTRICAL ANALYSIS

### 4.1 INTRODUCTION

Electrical safety is an important factor that must be incorporated into the design of photovoltaic modules. Of primary concern here is the determination of material thicknesses in the encapsulation system to withstand at least 3000 volts DC (the JPL/LSA requirement for module qualification testing) before the occurrence of electrical breakdown [9, 10].

Electrical breakdown in dielectric materials is a complex phenomenon which is not well understood. For instance, values of electrical properties such as dielectric constant, dielectric strength, and volume resistivity are strongly affected by humidity and temperature. In addition, manufacturing defects such as cracks and bubbles will have a deleterious effect on the ability of a module to withstand high voltage stresses.

A detailed analysis that takes all of the above factors into account is not called for in the present study. Instead, a simple series capacitance model and a simple series resistance model are developed for determining the electric field strength in each material layer of the encapsulation system. It is assumed here that a cell is operating at a given voltage,  $V_0$ , and that the shortest path for a potential short circuit is directly through the material layers on either side of the cell to a low-resistance path (such as a worker cleaning a module) to ground. Short circuit paths might be, for example, the pottant and organic front cover material in a substrate module, the pottant and wood-product/load-bearing member of a wood substrate module, or the pottant between the cell and metal-foil back cover of a glass superstrate module. The capacitance model is then used to calculate minimum material thicknesses (assuming flaws and manufacturing defects are absent) required to withstand electrical breakdown at 3000 volts DC.

## 4.2 ANALYTICAL MODELS

### 4.2.1 Resistance Model

Although organic materials are considered electrical insulators, these materials still exhibit small, but finite, "leakage" currents when subjected to a voltage stress. One method of calculating the electric field distribution in a module is to view the system as a group of resistors in series as shown in Figure 4-1.

The total voltage across the entire series string of resistors is equal to the sum of the voltages across all the resistors; that is,

$$\begin{aligned} V_0 &= V_1 + V_2 + V_3 + \dots + V_n \\ &= i_L (R_1 + R_2 + \dots + R_n) \end{aligned} \quad (4-1)$$

The voltage drop across the  $i^{\text{th}}$  resistor is given by

$$V_i = i_L R_i \quad (4-2)$$

and the resistance  $R_i$  is given by

$$R_i = \beta_i t_i / A \quad (4-3)$$

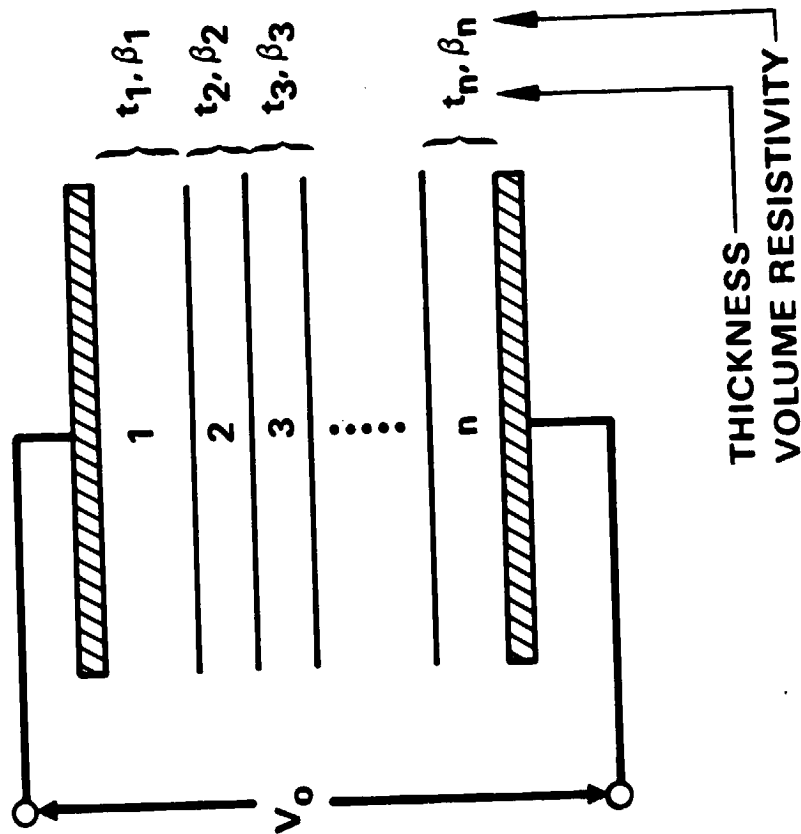
Dividing eq. (4-2) by eq. (4-1) and subsequent substitution of eq. (4-3) then yields

$$V_i / V_0 = \frac{\beta_i t_i}{\sum_{j=1}^n \beta_j t_j} \quad (4-4)$$

Now the electric field strength in layer  $i$ ,  $E_i$ , is related to the voltage drop across that layer as follows

$$E_i = V_i / t_i \quad (4-5)$$

Substitution of eq. (4-5) into eq. (4-4) then yields the desired relation for calculating the electric field strength in each layer.



## ANALYTICAL

- $E_i = \frac{\beta_i V_o}{\sum_{j=1}^n \beta_j t_j}$

## DESIGN CRITERIA

- $E_i < S_i$  FOR ALL LAYERS

$E_i$  = ELECTRIC FIELD STRENGTH IN LAYER  $i$

$S_i$  = DIELECTRIC STRENGTH

- $V_o = 3000$  VOLTS DC (LSA REQM'T)

Figure 4-1. Series Resistance Model for Determination of Electrical Isolation Characteristics of Photovoltaic Modules



$$E_i = \frac{\epsilon_i V_0}{\sum_{j=1}^n \epsilon_j t_j} \quad (4-6)$$

#### 4.2.2 Capacitance Model

In the capacitance model, shown in Figure 4-2, it is assumed that leakage currents are negligible and that crowding of electric field lines at cell corners and interconnects can be neglected as well.

From the fundamental principles of electrostatics, the electric potential,  $V$ , is defined as

$$V = \int E dt \quad (4-7)$$

Assuming the electrical properties are constant within each layer

$$V_0 = E_1 t_1 + E_2 t_2 + \dots + E_n t_n \quad (4-8)$$

To determine  $E_1$ , eq. (4-8) is rewritten as follows

$$V_0 = E_1 \left[ t_1 + \frac{E_2}{E_1} t_2 + \dots + \frac{E_n}{E_1} t_n \right] \quad (4-9)$$

Another fundamental principle of electrostatics is that the electric displacement vector remains constant across any interface between dielectrics.\* This condition may be expressed as follows

$$\epsilon_1 E_1 = \epsilon_2 E_2 = \dots = \epsilon_n E_n \quad (4-10)$$

Substituting eq. (4-10) into eq. (4-9) then yields

$$V_0 = E_1 t_1 + E_1 \left[ \frac{\epsilon_1}{\epsilon_2} t_2 + \dots + \frac{\epsilon_1}{\epsilon_n} t_n \right] \quad (4-11)$$

---

\*See reference 7, pp. 750-756 for a more complete discussion

# ANALYTICAL

$$\bullet E_i = \frac{V_o}{t_i + \gamma_i \sum_{j \neq i}^n \frac{t_j}{\gamma_j}}$$

## DESIGN CRITERIA

- $E_i < S_i$  FOR ALL LAYERS

$E_i$  = ELECTRIC FIELD STRENGTH IN LAYER  $i$

$S_i$  = DIELECTRIC STRENGTH

- $V_o = 3000$  VOLTS DC (LSA REOM'T)

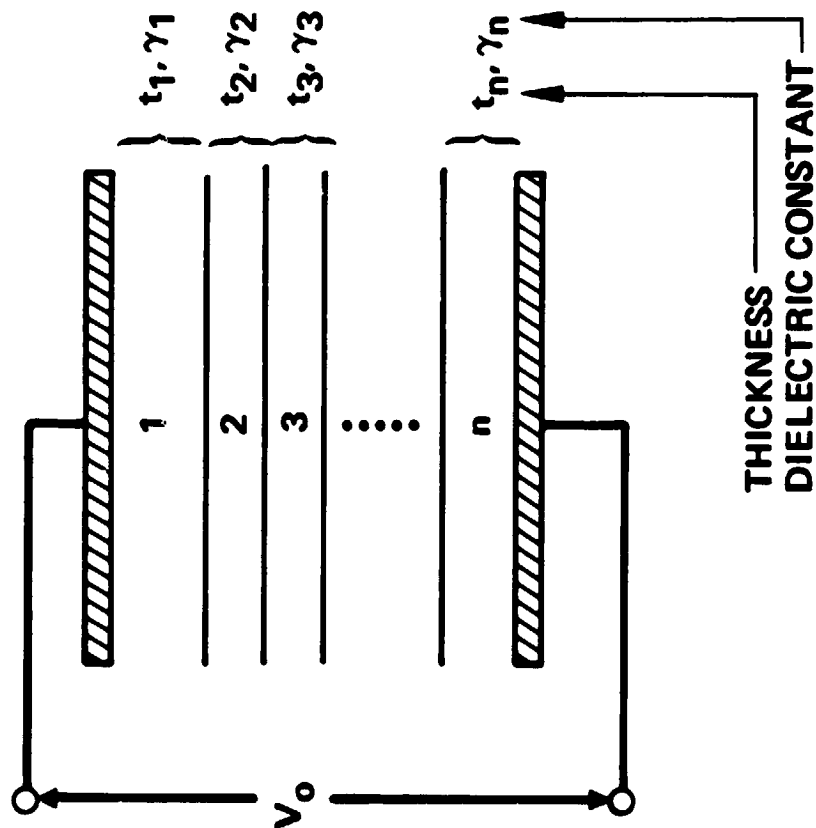


Figure 4-2. Series Capacitance Model for Determination of Electric Isolation Characteristics of Photovoltaic Modules

$$V_0 = E_1 \left[ t_1 + \sum_{j=2}^n \frac{\gamma_1}{\gamma_j} t_j \right] \quad (4-11)$$

Solving for  $E_1$ , leads to

$$E_1 = \frac{V_0}{t_1 + \gamma_1 \sum_{j=2}^n \frac{t_j}{\gamma_j}} \quad (4-12)$$

Equation 4-12 can be generalized for any layer,  $i$

$$E_i = \frac{V_0}{t_i + \gamma_i \sum_{j \neq i}^n \frac{t_j}{\gamma_j}} \quad (4-13)$$

For a two layer system, such as the front cover and pottant above cell combination found in substrate modules, the following expressions apply for  $E_1$  (front cover) and  $E_2$  (pottant)

$$E_1 = \frac{V_0}{t_1 + \frac{\gamma_1}{\gamma_2} t_2} \quad (4-14)$$

$$E_2 = \frac{V_0}{\frac{\gamma_2}{\gamma_1} t_1 + t_2} \quad (4-15)$$

For a single layer system, such as the pottant between cell and metal-foil back cover of a glass superstrate module, the appropriate expression for the electric field strength is given in eq. (4-5).

### 4.3 DISCUSSION

Values of dielectric constant ( $\gamma$ ), dielectric strength ( $S$ ), and volume resistivity ( $\rho$ ) are given in Appendix A (Table A-3) for wood-product substrate and for a variety of pottants and organic cover films used in photovoltaic modules. The results of a literature survey indicate that all three properties are temperature dependent as well as humidity dependent. In addition, both the dielectric constant and the dielectric strength are frequency dependent and the dielectric strength is also dependent upon material thickness. The ranges of uncertainties for the dielectric constant and dielectric strength are significantly less than the uncertainty in volume resistivity; hence only the capacitance model is used in subsequent calculations. Regardless of the model used, the electrical-safety design criteria used in this study is that the electric field strength in each layer does not exceed the dielectric strength,  $S_i$ , of that layer. In other words,

$$E_i < S_i \quad (4-16)$$

for all layers when  $V_0 = 3000$  volt DC.

For glass superstrate modules, the only layer of interest from an electrical safety standpoint is the pottant layer between the cell and the metal-foil back cover. It is assumed the plastic film (i.e. Mylar in most cases) on the exterior surface of the foil can be cracked or nicked while inserting the module in an array frame. Thus, it is assumed that the pottant layer below the cell must withstand the full voltage difference.

To determine the minimum thickness of pottant below the cell to withstand a given potential drop  $V_0$ , the appropriate value of the dielectric strength is substituted for  $E$  in eq. (4-5) to yield:

$$t = V_0/S \quad (4-17)$$

Substitution of appropriate values of  $S$  from Table A-3 into the above equation yields calculated values of the minimum pottant thickness required to withstand 3000 volts. These pottant thicknesses are summarized in Table 4-1. Again, it should be emphasized that these pottant thicknesses are for defect-free materials.

TABLE 4-1. Minimum Thickness of Pottant Under Cell to Withstand 3000 Volts DC for Glass Superstrate Modules\*

Pottant	Thickness, mil
Ethylene vinyl acetate (EVA)	4.8
Ethylene propylene rubber (EPR)	3.0-6.0
Polyurethane	4.3-9.1
Poly n-butyl acrylate (PNBA)	3.8
Poly vinyl chloride plastisol	10

\* Results applicable to metal substrate modules as well.

An item of interest to designers is the relationship between the top cover and transparent pottant thicknesses for safe electrical operation of substrate modules. This relationship can be determined by solving eqs. (4-14) and (4-15) for  $t_2$  and then substituting  $S_1$  for  $E_1$  and  $S_2$  for  $E_2$  (because we want to calculate the minimum thickness at which breakdown can be avoided); the result is:

$$t_2 = \frac{\frac{V_0}{S_1} - t_1}{(r_1/r_2)} \quad (4-18)$$

$$t_2 = \frac{V_0}{S_2} - \frac{t_1}{(r_1/r_2)} \quad (4-19)$$

The thickness  $t_2$  calculated by means of eq. (4-19) is the minimum allowable thickness of pottant above the cell to prevent voltage breakdown in the pottant. For conservative design, the values of  $t_2$  calculated by means of eq. (4-18) should be greater than those by means of eq. (4-19).

A sensitivity study was performed by calculating  $t_2$  for different values of  $S_1$  (top cover dielectric strength),  $\gamma_1/\gamma_2$ , and  $t_1$  for the LSA 3000-volt requirement. The results were calculated by means of eq. (4-18) and are shown in Figures 4-3 through 4-6. For any combination of pottant and front cover materials, the acceptable combinations of  $t_1$  and  $t_2$  lie above and to the right of the line for the value of  $\gamma_1/\gamma_2$  corresponding to that material combination. As expected, when  $t_1 = V_0/S_1$ , the front cover can withstand the entire voltage, and the required pottant thickness for electrical isolation becomes negligible.

Some specific examples for a Korad top cover and different pottants are shown in Figures 4-7 and 4-8. As in Figures 4-3 through 4-6, the values of  $t_2$  were calculated by means of eq. (4-18). The curves in Figures 4-7 and 4-8 exhibit the same behavior as that shown in Figures 4-3 thru 4-6. The two lines each for the polyurethane and EPR in Figure 4-7 and for PVC plastisol in Figure 4-8, correspond to the range of values for the dielectric constant at 60 Hz for each of these pottants. The values of  $\gamma_1$  and  $\gamma_2$  used in these calculations were evaluated at 60 Hz. Ideally, these properties should be evaluated at zero frequency, since photovoltaic cells generate dc power. However, dc values of dielectric constant for most organic materials are not available in the literature.

#### 4.4 CONCLUSIONS

A comparison of the results of this section with those of Section 3 leads to the following conclusions for construction materials free of mechanical defects such as cracks, bubbles, and pinholes:

- Electrical isolation requirement and temperature excursion criterion are equally important in determination of pottant thickness between cell and load-bearing member for steel substrate modules.
- Pottant thickness between cell and load-bearing member of unribbed, wood-product substrate modules is determined by structural deflection criterion.
- Electrical isolation requirement determines necessary pottant thickness between cell and front cover of substrate modules.

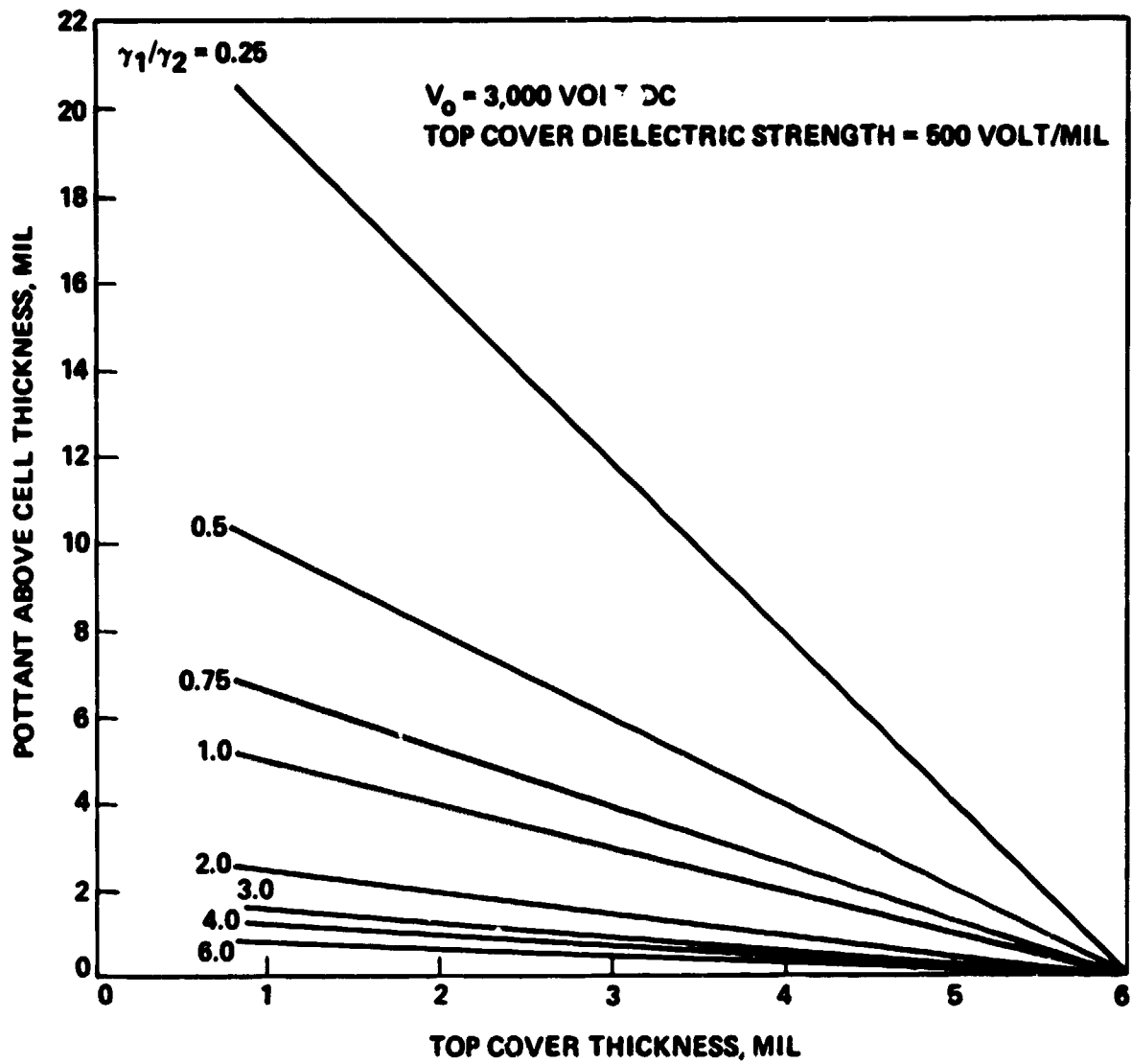


Figure 4-3. Thickness of Pottant Above Cell versus Top Cover Thickness for  $V_0 = 3000$  Volt DC and Top Cover Dielectric Strength = 500 Volt/mil

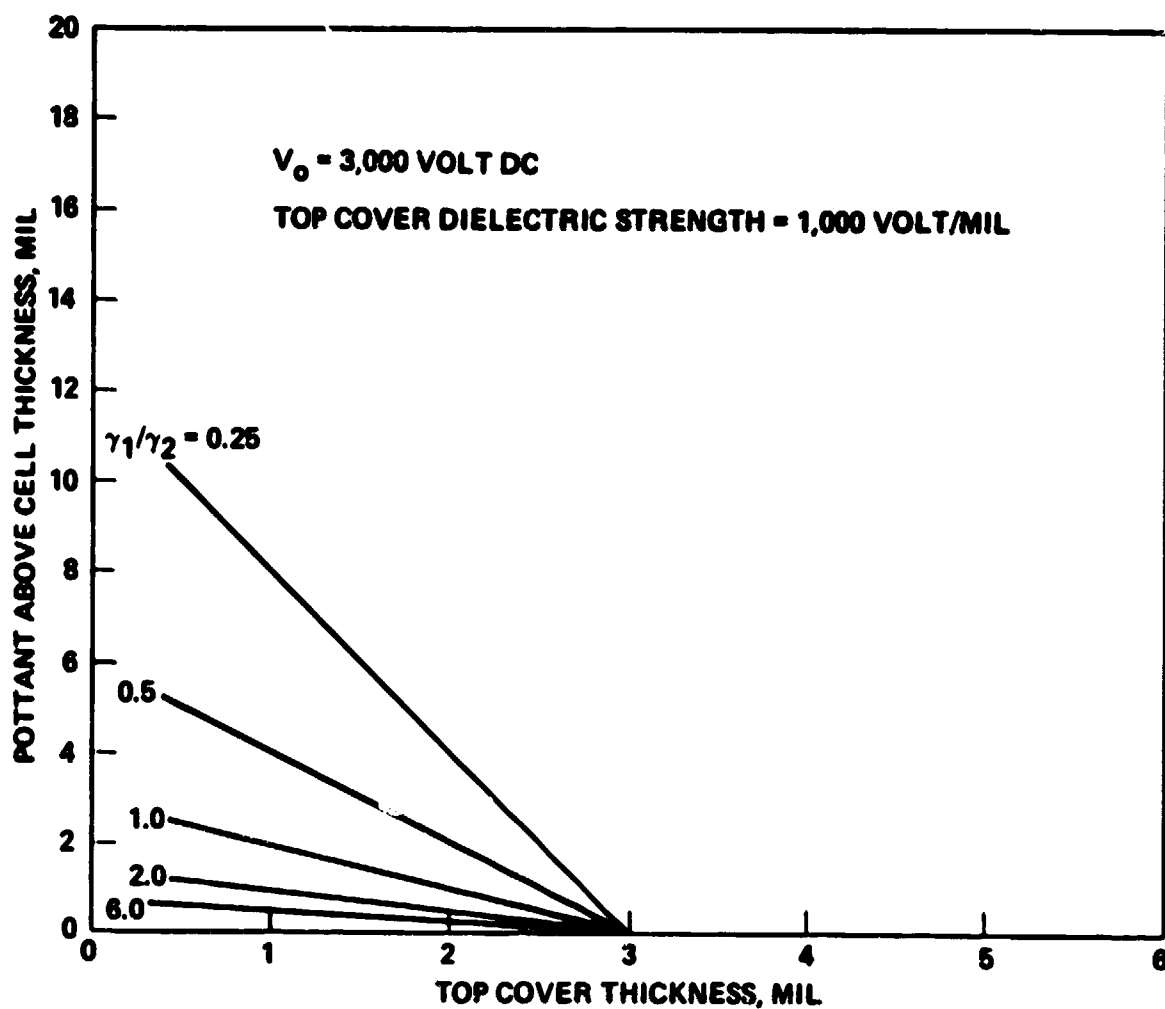


Figure 4-4. Thickness of Pottant Above Cell versus Top Cover Thickness for  $V_0 = 3000$  Volt DC and Top Cover Dielectric Strength = 1000 Volt/mil



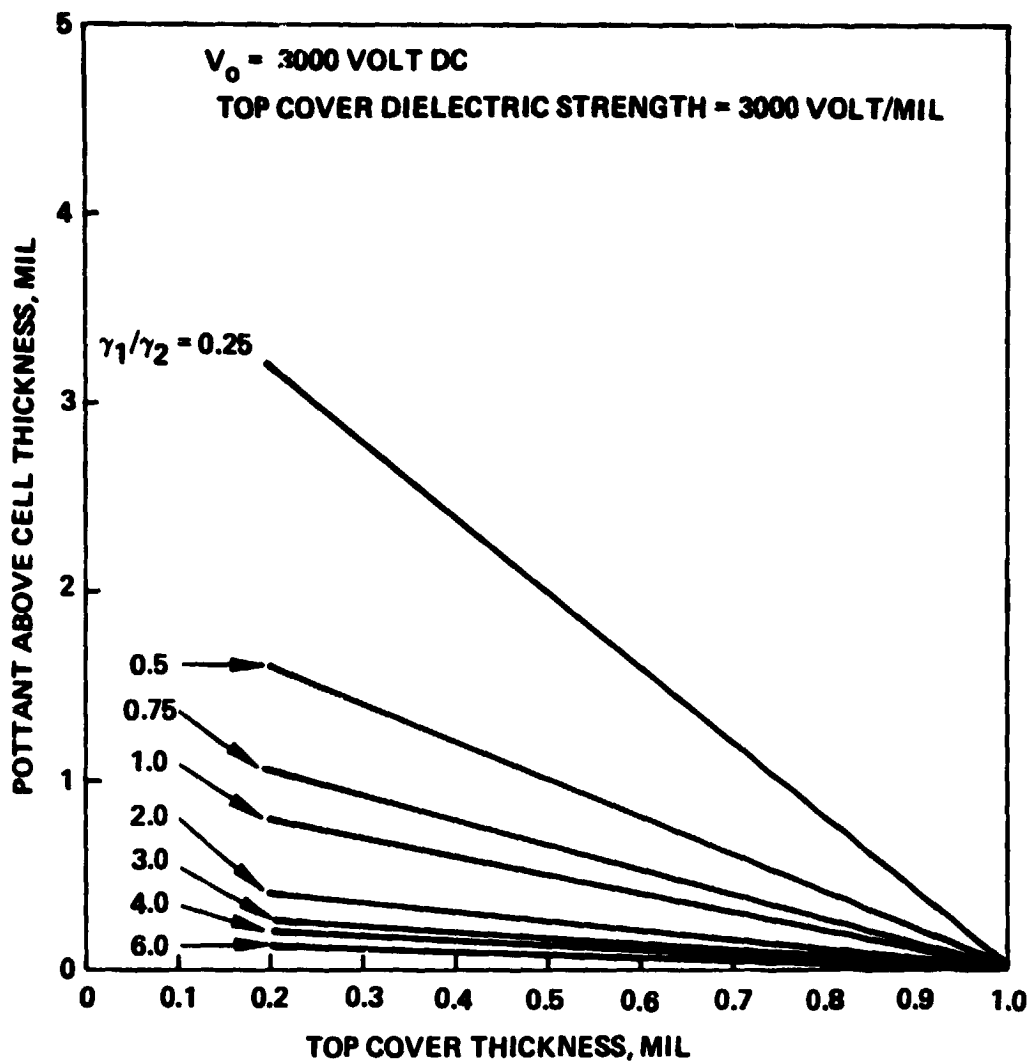


Figure 4-5. Thickness of Pottant Above Cell versus Top Cover Thickness for  $V_0 = 3000 \text{ Volt DC}$  and Top Cover Dielectric Strength = 3000 Volt/mil

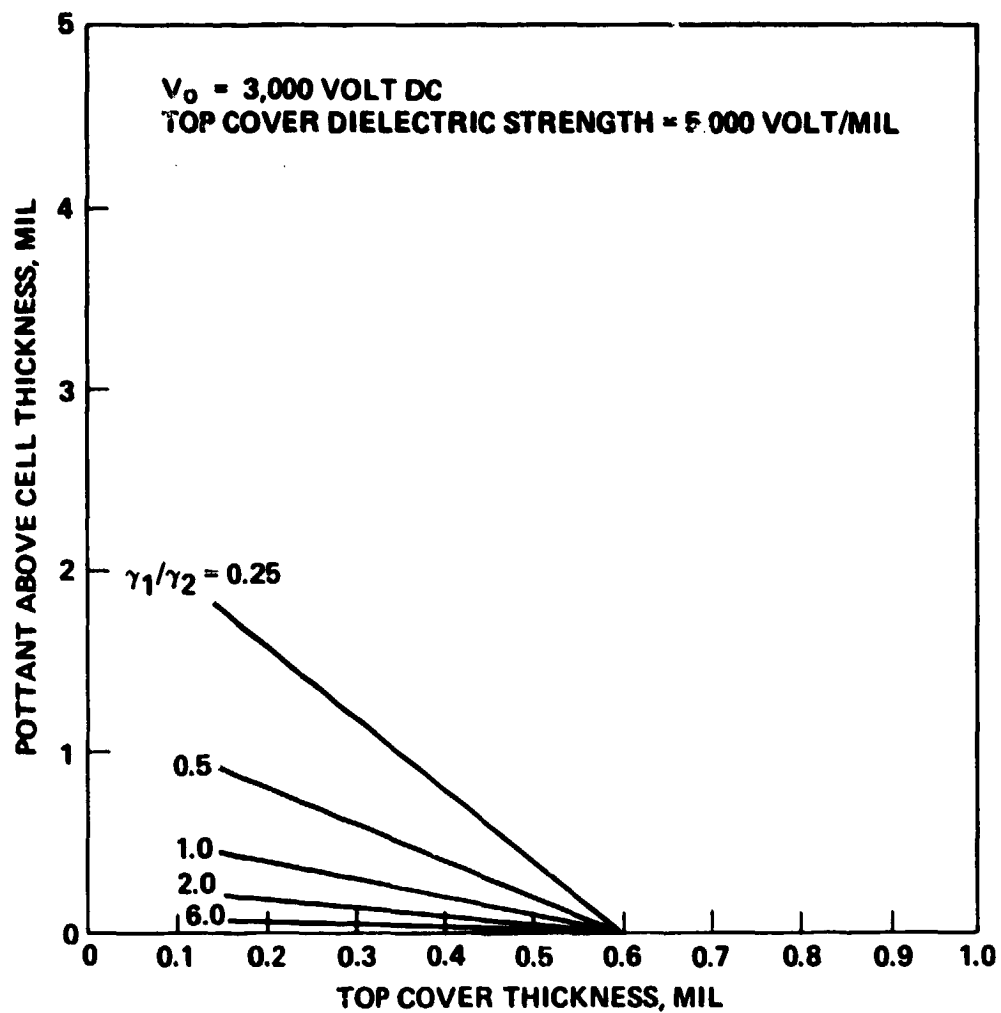


Figure 4-6. Thickness of Pottant Above Cell versus Top Cover Thickness for  $V_0 = 3000$  Volt DC and Top Cover Dielectric Strength = 5000 Volt/mil

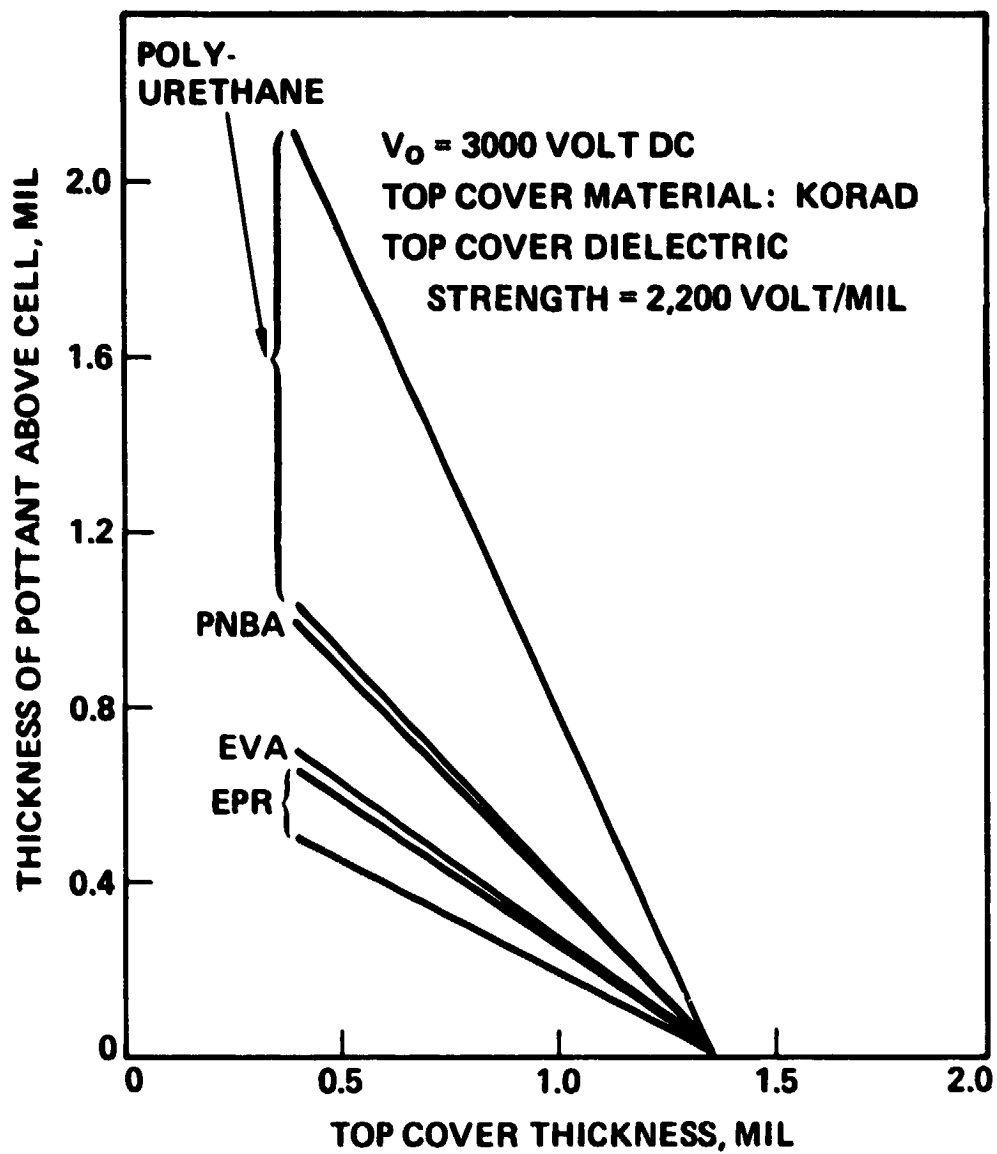


Figure 4-7. Thickness of Pottant Above Cell versus Top Cover Thickness for Korad and Polyurethane, PNBA, and EPR

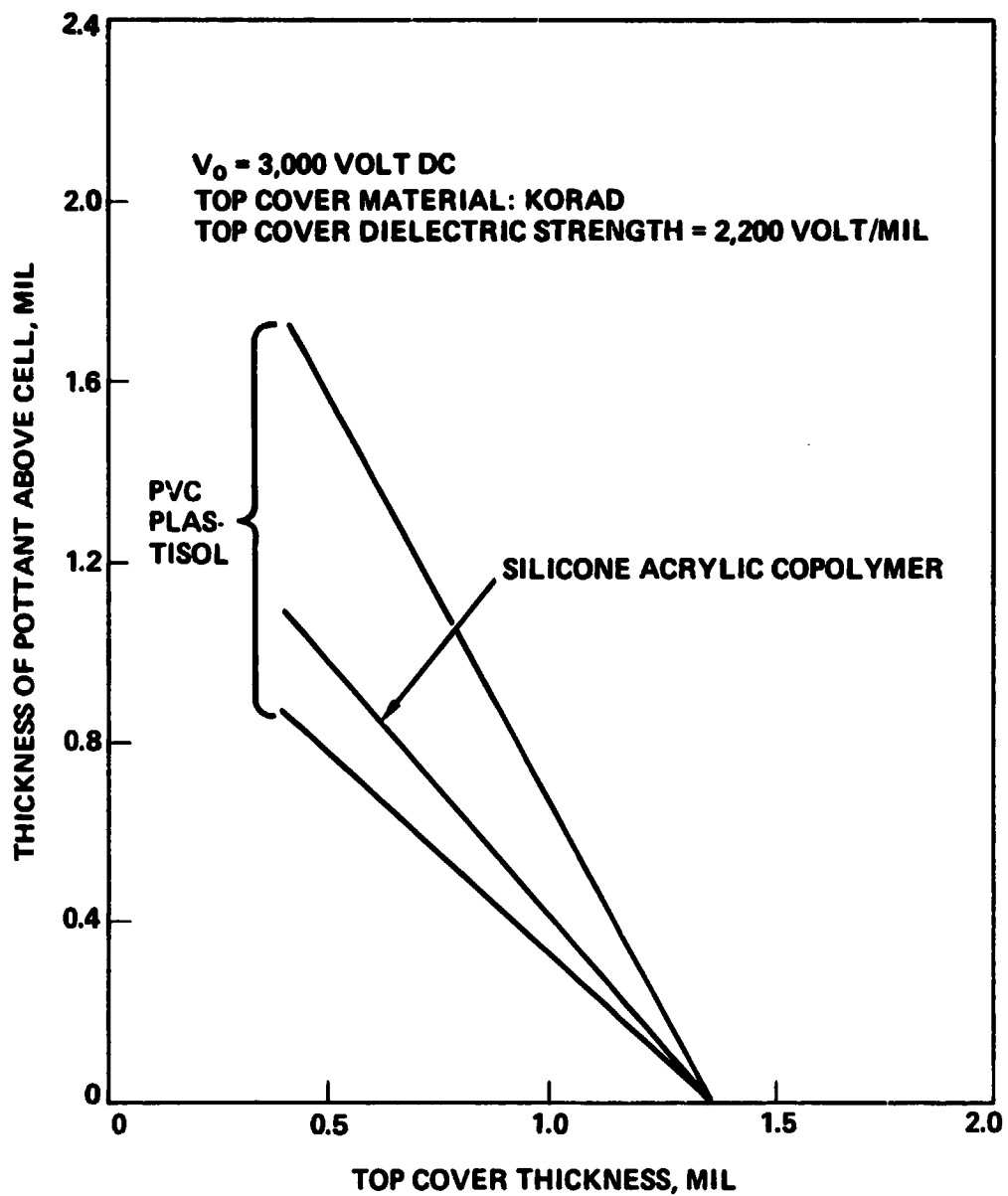


Figure 4-8. Thickness of Pottant Above Cell versus Top Cover Thickness for Korad, PVC Plastisol, and Silicone Acrylic Copolymer

## 5.0 OPTICAL ANALYSIS

### 5.1 INTRODUCTION

Solar radiation incident on the front surface of a module is partially reflected from and partially transmitted through that surface. The transmitted portion is absorbed and reflected within the layers of the encapsulation system and absorbed at the cell surface. Radiant energy absorbed in the encapsulation system is converted to heat, and the radiant energy absorbed at the cell surface is converted partially to electricity and partially to heat.

In this section, a methodology is developed for determination of the radiant energy absorbed by the cells and the encapsulation system of a terrestrial photovoltaic module. Since it is convenient to incorporate the computational algorithms developed in this section into the thermal model described in Section 6, the results and conclusions of the optical analysis are discussed along with the results and conclusions of the thermal analysis. At this point, the reader not interested in details of the optical analysis may skip to the next section.

The primary purpose of the optical analysis is to predict the effective transmittance of sunlight through an encapsulation system and to indicate design directions for maximizing this transmittance. Effective transmittance is defined as the ratio of the electrical power output from an encapsulated cell to the electrical power output from a bare cell. To determine the effective transmittance, it is necessary to determine a weighted average transmittance of the encapsulation system; the weighting corresponds to the spectral power conversion efficiency of the cell. An effective transmittance of at least 90 percent is desired for an encapsulated solar cell facing normal to the sun.

The solar spectrum, solar cells, some basic optical principles, and the radiosity-irradiation analysis technique are briefly reviewed in Section 5.2. In section 5.3 these principles are combined into a general procedure for determination of the radiant energy absorbed by the cells and the encapsulation system. This procedure consists of dividing the solar spectrum into a number of equal-energy spectral bands. For each spectral band, the radiosity-irradiation analysis is used to calculate the solar radiation absorbed in each layer of the encapsulation system and in the cells. For each spectral band, radiant energy absorbed by a cell is then multiplied by the corresponding value of the spectral power conversion efficiency to obtain the dc power generated by the cell. These results are summed for all spectral bands to give the total electrical power output from the cell.

## 5.2 BASIC PRINCIPLES AND BACKGROUND INFORMATION

### 5.2.1 Solar Radiation

Solar radiation propagates radially outward from the sun. The spectral energy distribution of this radiation at the edge of the terrestrial atmosphere is indicated by the solid line in Figure 5-1. Solar radiation is partially absorbed and partially scattered as it travels thru the atmosphere. Absorption is due to the presence of atmospheric constituents such as water vapor and carbon dioxide, and scattering is due to the presence of water droplets and particulates. Both absorption and scattering increase with increasing path length of the radiation travelling thru the atmosphere. Bouger's law, eq. (5-1), is a simple method for calculating the absorption of solar radiation in a clear atmosphere.

$$I_{\lambda} = I_{0\lambda} e^{-km} \quad (5-1)$$

where  $I_{0\lambda}$  and  $I_{\lambda}$  are the extraterrestrial and ground-level intensities of beam radiation respectively,  $k$  is a constant that characterizes atmospheric absorption, and  $m$  is the dimensionless path length for sunlight travelling

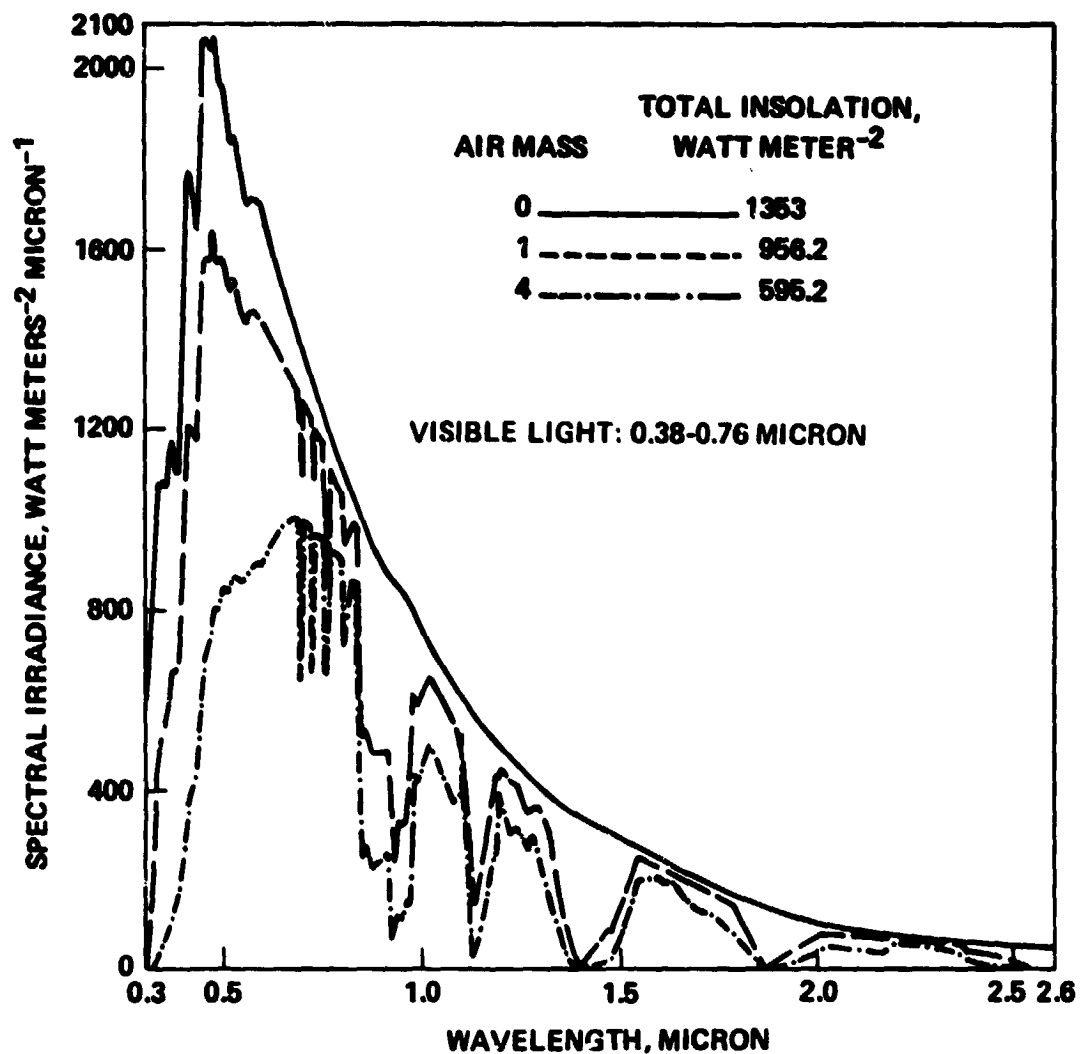


Figure 5-1. Solar Spectral Irradiation for Different Air Mass Values, Assuming U.S. Standard Atmosphere, 20 mm of Precipitable Water Vapor, 3.4 mm of Ozone, and Very Clear Air (from reference 26 .  $\alpha = 1.3$ ,  $\beta = .02$ ).

thru the atmosphere. The parameter  $m$  is called the air mass ratio; a graphical definition of  $m$  is shown in Figure 5-2. Air mass zero ( $m=0$ ) corresponds to extraterrestrial radiation. Solar radiation is absorbed in several wavelength bands for  $m>0$  as shown in Figure 5-1. These bands correspond to the different absorbing constituents in the atmosphere.

In addition to direct solar radiation, there is diffuse radiation from the sky due to the scattering mentioned previously. This diffuse radiation accounts for about 20 percent of the total solar radiation impinging on a horizontal surface. The ratio of diffuse to direct radiation is high in the ultraviolet region (which accounts for the blue sky), but drops rapidly in the visible and infrared regions.

### 5.2.2 Solar Cells

The efficiency of solar cells is strongly dependent upon the wavelength of the incident radiation, the intensity of radiation impinging on the cell surface, and on the cell temperature [16]. An exact analysis of solar cell efficiency requires knowledge of the spectrum of the incident radiation, spectral power conversion efficiency of the cell, current-voltage characteristics, and series resistance of the solar cell [11].

The spectral power output  $P_\lambda$  of a bare (i.e. unencapsulated) solar cell in wavelength band  $d\lambda$  is equal to the product of the spectral power-conversion efficiency of the cell,  $C_\lambda$ , the spectral solar irradiation,  $I_\lambda$ , the area of the cell  $A_c$  and  $d\lambda$ .

$$P_\lambda = A_c C_\lambda I_\lambda d\lambda \quad (5-2)$$

Typical spectral power-conversion efficiencies of unencapsulated single-crystal, polycrystalline, and amorphous silicon cells are shown in Figure 5-3. The total power output of the cell is the integral of eq. (5-2) over all wavelengths.

$$P = A_c \int_0^\infty C_\lambda I_\lambda d\lambda \quad (5-3)$$



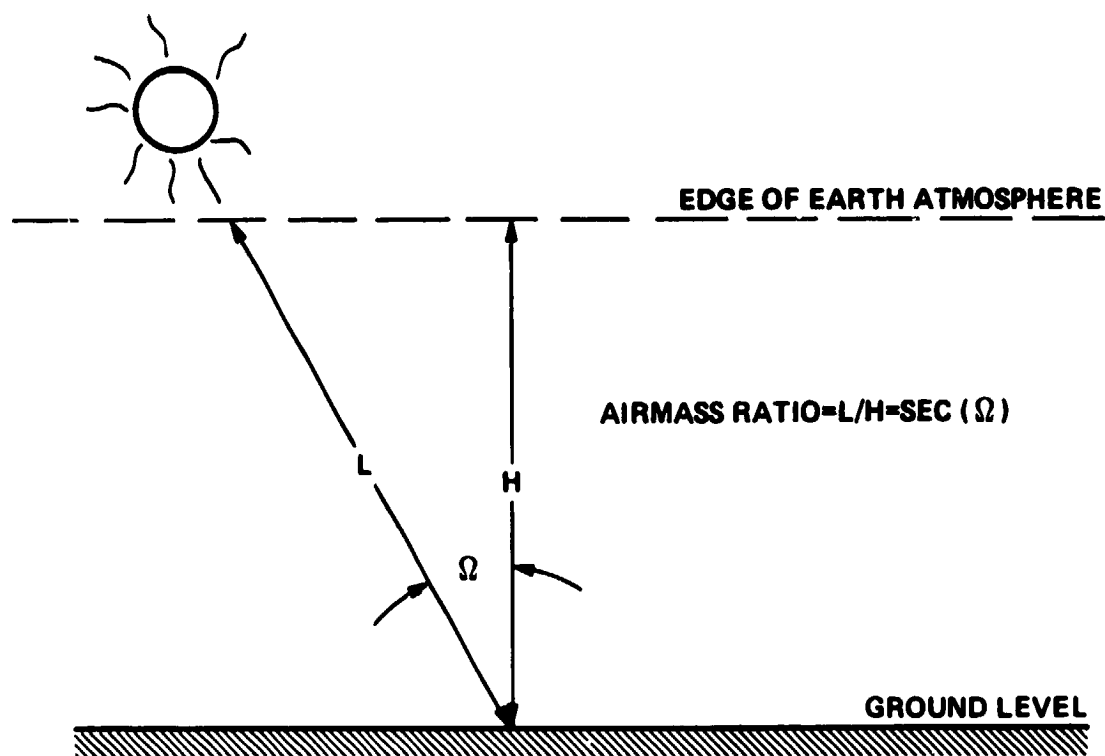


Figure 5-2. Definition of Air Mass Ratio

Now consider a solar cell embedded in an encapsulation system with a spectral transmittance  $T_\lambda$ . The spectral power output of the encapsulated cell,  $PE_\lambda$ , is given by

$$PE_\lambda = A C_\lambda I_\lambda T_\lambda d\lambda \quad (5-4)$$

The total power output of the encapsulated solar cell is the integral of eq. (5-4) over all wavelengths

$$PE = A_c \int_0^\infty C_\lambda I_\lambda T_\lambda d\lambda \quad (5-5)$$

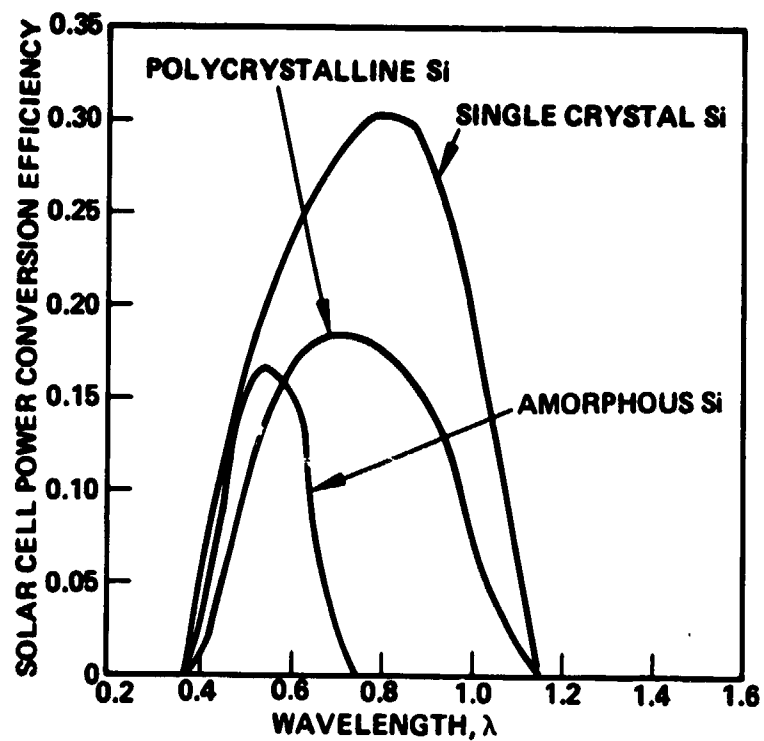


Figure 5-3. Wavelength Dependence of Solar Cell Power Conversion Efficiency

The effective transmittance,  $T_{\text{eff}}$ , of the encapsulation system can now be determined from eqs. (5-3) and (5-5)

$$T_{\text{eff}} = \frac{PE}{P} = \frac{\int_0^{\infty} C_{\lambda} I_{\lambda} T_{\lambda} d\lambda}{\int_0^{\infty} C_{\lambda} I_{\lambda} d\lambda} \quad (5-6)$$

Note that in eq. (5-6) the relative spectral response of the cell may be used in place of spectral power conversion efficiency since this term appears in both integrals. Also, the spectral solar radiation term may be replaced with a relative spectral radiation term. Consequently, we need not know the actual values of power conversion efficiency or solar radiation as a function of wavelength, but merely how these quantities vary with wavelength.

### 5.2.3 Reflection and Refraction

The specular reflection and refraction of light at the interface between two different dielectric materials with different indices of refraction is shown in Figure 5-4. The portion of light reflected from the interface is given by Fresnel's equation [20].

$$\rho(\theta_1) = \frac{1}{2} \left[ \frac{\sin^2(\theta_1 - \theta_2)}{\sin^2(\theta_1 + \theta_2)} + \frac{\tan^2(\theta_1 - \theta_2)}{\tan^2(\theta_1 + \theta_2)} \right] \quad (5-7)$$

where  $\theta_1$  is the angle of incidence,  $\theta_2$  is the angle of refraction, and  $\rho(\theta_1)$  is the reflectivity.\* Snell's law gives the relationship between the angles of reflection and refraction

$$N_1 \sin \theta_1 = N_2 \sin \theta_2 \quad (5-8)$$

where the N's are the indices of refraction for the two materials.

---

\*Reflectivity is the percentage of incident radiation reflected at an interface between two materials. Reflectance is the percentage of incident radiation reflected by a thin film of finite thickness.

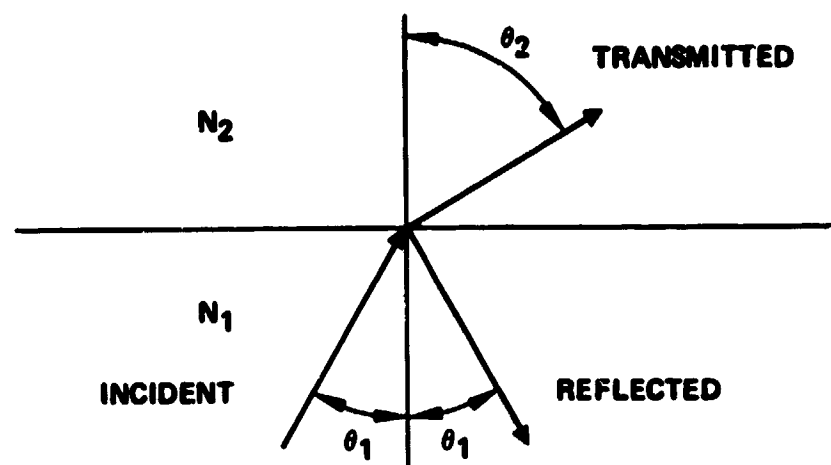


Figure 5-4. Reflection and Refraction at the Interface Between Two Dielectric Materials with Different Indices of Refraction

If  $N_2$  is less than  $N_1$ , then all the incident light is reflected for angles of incidence greater than or equal to the critical angle  $\theta_c$ , where  $\theta_c$  is given by

$$\theta_c = \sin^{-1} \left( \frac{N_2}{N_1} \right) \quad (5-9)$$

This is known as total internal reflection. If  $N_2$  is greater than  $N_1$ , then some portion of the incident light is always transmitted through the interface. As seen in Figure 5-5, the reflectivity of the interface varies with the angle of incidence for  $N_2$  both less than and greater than  $N_1$ . For small angles of incidence, eq. (5-7) can be approximated by the relationship

$$\rho = \left( \frac{N_1 - N_2}{N_1 + N_2} \right)^2 \quad (5-10)$$

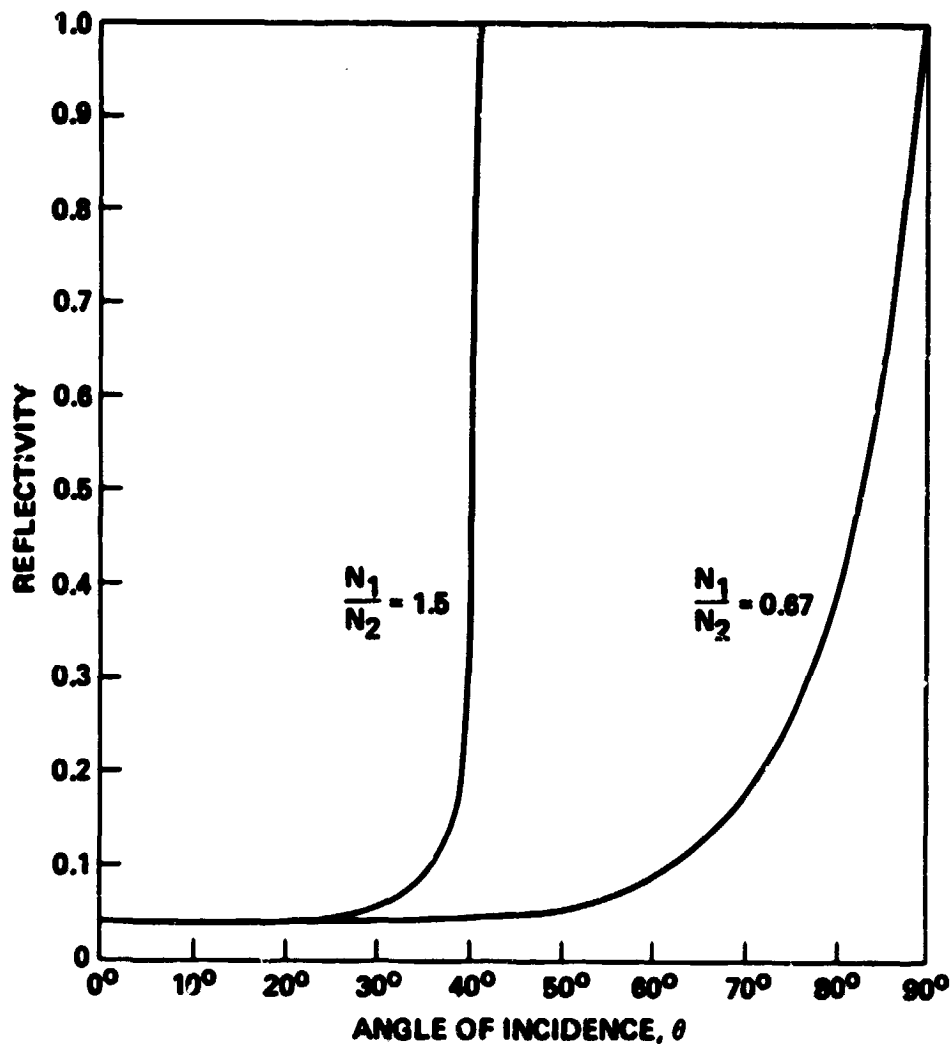


Figure 5-5. Reflectivity from Interface Between Two Materials With Different Indices of Refraction

Due to the wave nature of light, reflections from the surfaces of a very thin layer of material can be made to cancel each other. This is the principle behind AR (antireflection) coatings. Consider a thin layer of thickness,  $t_A$ , and index of refraction,  $N_A$ , sandwiched between two materials of indices,  $N_1$  and  $N_2$ , as shown in Figure 5-6.

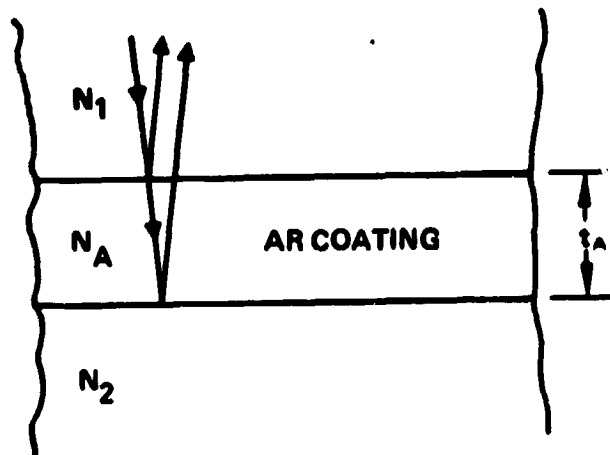


Figure 5-6. Nomenclature for Antireflection Coating

The reflectance of the coating,  $\rho_A$ , depends on the wavelength and indices of refraction in the following manner [20]:

$$\rho_A = \frac{r_1^2 + r_2^2 + 2r_1 r_2 \cos \omega}{1 + r_1^2 r_2^2 + 2r_1 r_2 \cos \omega} \quad (5-11a)$$

where the parameters  $r_1$ ,  $r_2$ , and  $\omega$  are given by

$$r_1 = \frac{N_1 - N_A}{N_1 + N_A} \quad (5-11b)$$

$$r_2 = \frac{N_A - N_2}{N_A + N_2} \quad (5-11c)$$

$$\omega = 4\pi N_A t_A / \lambda \quad (5-11d)$$

If the AR coating has a thickness equal to one-quarter wavelength of the incident light

$$t_A = \frac{\lambda}{4N_A} \quad (5-12)$$

the two reflections are out of phase, and the overall reflection from the AR coating is be greatly reduced. For a quarter-wave thick film, the reflection is zero if

$$N_A = \sqrt{N_1 N_2} \quad (5-13)$$

Use of eqs. (5-12) and (5-13) permit the optimization of an AR coating for normal incidence at a particular wavelength.

Typical AR coatings are optimized for use in air. If a solar cell is encapsulated, the thickness of the AR coating must be chosen on the basis of the indices of refraction of the surrounding materials. Figures 5-7 and 5-8 show the difference in reflectivity for an encapsulated solar cell with an AR coating optimized for an air/cell interface and a coating optimized for a pottant/cell interface. There is a small advantage to optimizing the AR coating on the basis of the indices of refraction of the cell/pottant combination (see Section 6 for further discussion of this matter).

During the course of this study, questions were raised regarding the overall conversion efficiency of the cell and whether this efficiency is applied to a bare cell or to an AR-coated cell. The conventional efficiency for a photovoltaic cell is defined as follows:

$$\eta^* = \text{cell efficiency} = \frac{\text{electrical power out}}{\text{radiant energy incident on cell surface per unit time}} \quad (5-14)$$

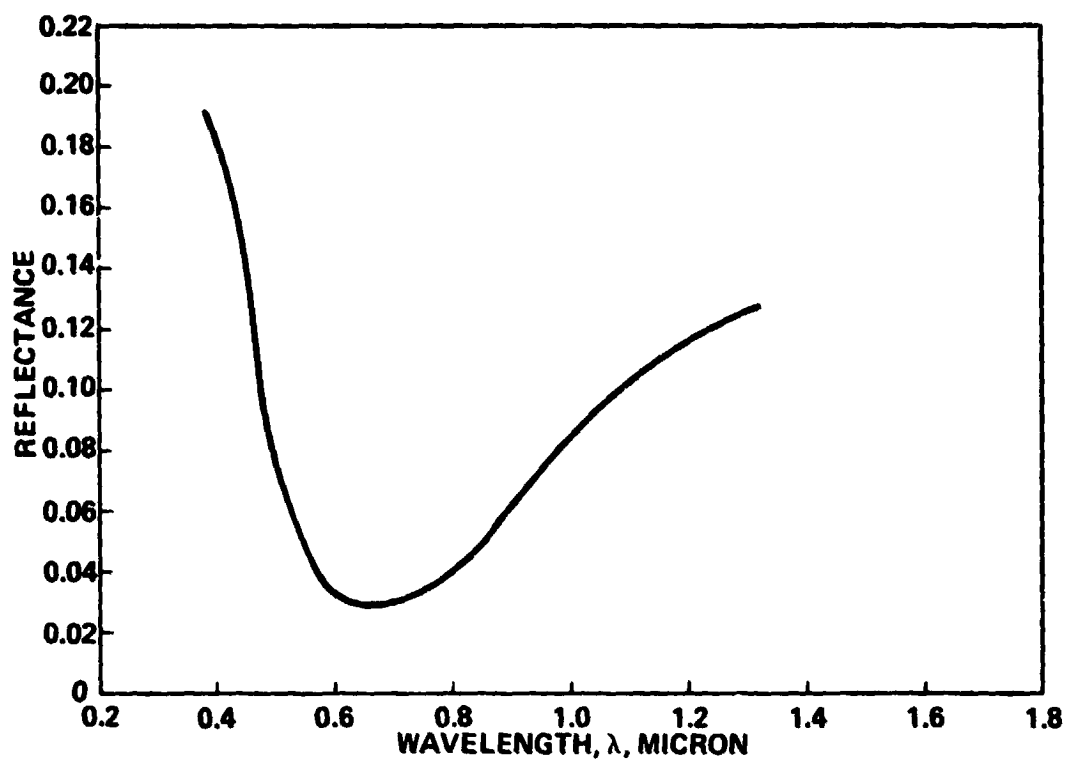


Figure 5-7. AR-Coating Reflectance versus Wavelength for Coating Optimized for Air/Silicon Interface



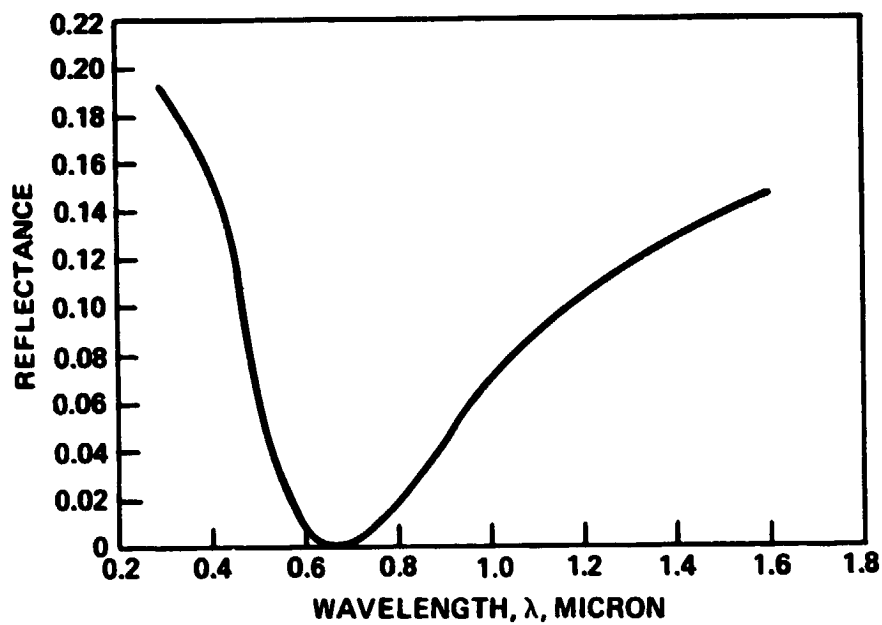


Figure 5-8. AR-Coating Reflectance versus Wavelength  
Coating Optimized for Pottant/Silicon Interface

However, the overall conversion efficiency,  $\eta$ , used in the thermal/optical program described in Section 6 of this report, is defined somewhat differently

$$\eta = \frac{\text{electrical power out}}{\text{radiant energy absorbed by cell per unit time}} \quad (5-15)$$

To determine the required values of  $\eta$ , it is noted that the incident solar radiation,  $Q_i$ , is either reflected ( $Q_r$ ) or absorbed ( $Q_c$ ) at the cell surface, and that the absorbed radiation is converted to both electrical energy ( $P$ ) and heat ( $Q_h$ ).

$$Q_i = Q_r + Q_c = Q_r + P + Q_h \quad (5-16)$$

Noting that the definition of  $\eta^*$  is given by

$$\eta^* = P/Q_i \quad (5-17)$$

and that the definition of  $\eta$  is given by

$$\eta = P/Q_c \quad (5-18)$$

It is seen that  $\eta$  can be obtained as a function of  $\eta^*$  and  $Q_c$  by combination of eqs. (5-17) and (5-18) to give

$$\eta = \eta^* Q_i / Q_c \quad (5-19)$$

An AR-coated, nontexturized silicon cell absorbs approximately 89 percent of the incident solar radiation, hence  $Q_c/Q_i = .89$ . Therefore, eq. (5-19) becomes

$$\eta = \eta^* / .89 \quad (5-20)$$

The corresponding values of  $\eta$  for single crystal, polycrystalline, and amorphous silicon are listed in Table 5-1.

TABLE 5-1. Values of Overall Conversion Efficiencies for Silicon Solar Cells

Cell Type	$\eta^*$	$\eta$
Single Crystal	14.5	16.3
Polycrystalline	8.5	9.6
Amorphous	5.0	5.6

Light reflection at the cell surface can also be reduced by texturizing the cell surface. The simple model shown in Figure 5-9 is used to determine the reflectance for a non AR-coated, texturized cell. Here, it is assumed that an incident light beam impinges twice on the cell before being reflected away.

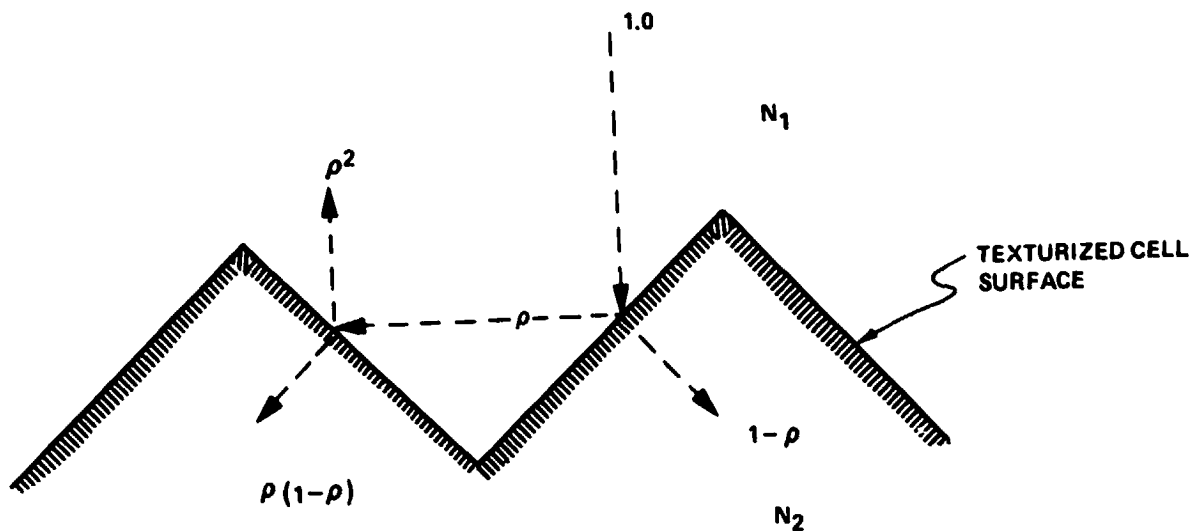


Figure 5-9. Simplified Model of Texturized Cell Surface

In this idealized model, the value of  $Q_c/Q_i$  is

$$Q_c/Q_i = 1 - \rho^2 \quad (5-21)$$

where  $\rho$  is calculated by means of eq. (5-10). It is further assumed that the value of  $Q_c/Q_i$  for nonideal texturized cells is 95 percent of that given in eq. (5-21). Thus, the reflectivity of a texturized cell,  $\rho_T$ , is

$$\rho_T = 1 - .95 \frac{Q_c}{Q_i} = .05 - .95 \rho^2 \quad (5-22)$$

#### 5.2.4 Radiosity-Irradiation Analysis

Consider a gray, nonopaque surface as depicted in Figure 5-10.  $q_1^-$  and  $q_2^-$  are incoming (i.e. toward the surface) radiant fluxes, and  $q_1^+$  and  $q_2^+$  are outgoing (i.e. away from the surface) radiant fluxes. The subscripts 1 and 2 denote which side of the surface the fluxes are referenced to, while the superscripts (-) and (+) denote incoming and outgoing fluxes, respectively. The incoming flux is called the irradiation, and the outgoing flux is called the radiosity.

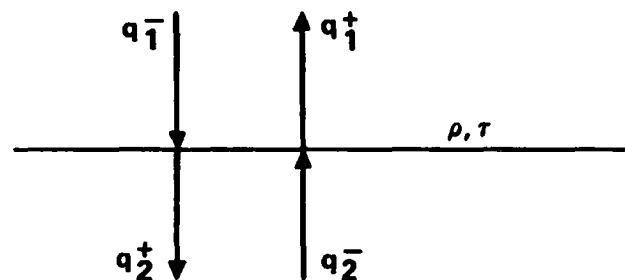


Figure 5-10. Radiant Energy Fluxes at a Surface

Let  $\rho$ , and  $\tau$  stand for the reflectivity, and transmissivity of the surface. Ignoring any radiant energy emission from the surface itself (see Section 6 for further discussion of this assumption) the radiosity can be expressed in terms of the irradiation terms in the following manner

$$q_1^+ = \rho q_1^- + \tau q_2^- \quad (5-23)$$

$$q_2^+ = \tau q_1^- + \rho q_2^- \quad (5-24)$$

The radiosity-irradiation equations are easily applied to radiation exchange involving several surfaces and absorbing media. The transmittance of an absorbing medium of thickness,  $t$ , is given by

$$T = e^{-at} \quad (5-25)$$

where  $a$  is the absorption coefficient of the medium.

A comparison of the radiosity-irradiation method and the classic infinite series (ray tracing) method for solving multireflection radiation problems in a thin film is given in Appendix E. The radiosity-irradiation method is used in this analysis because the resulting set of simultaneous equations for a multilayer system can be easily solved by means of a desk calculator or by digital computer. The classic ray-tracing technique does not offer this convenience.

#### 5.2.5 The Internal Enhancement Phenomenon

As shown in Figure 2-1, the cells rest on a layer of opaque pottant in a photovoltaic module. Due to internal reflections within the encapsulation system, some of the light reflected from the intercell areas strikes the cells. This enhancement of cell irradiation is referred to as the zero-depth concentrator phenomenon by Mark and Volk [12], who investigated this phenomenon for several different cell patterns. Their findings indicate that this effect is negligible for rectangular cells in a close-packed arrangement such as that studied in this report. For this reason, the internal enhancement phenomenon is not discussed here. A summary of Mark's and Volk's work is included in Appendix D along with the necessary equations for correcting the analyses of the next section for modules with different cell arrangements.

### 5.3 ANALYTICAL PROCEDURE AND EQUATIONS

#### 5.3.1 Accounting for Spectral Variations

As discussed in Section 5.1, the required results from this analysis are the effective transmittance of the encapsulation system and the amount of incident radiant energy absorbed as heat in the various layers of the encapsulation system. The effective transmittance is given by eq. (5-6). The spectral power conversion efficiency,  $C_\lambda$ , of a particular cell and the spectral solar (or any other source such as a tungsten lamp) radiation,  $I_\lambda$ , are independent of the encapsulation system. Only the spectral transmittance,  $T_\lambda$ , depends on the encapsulation system under study. Variation in the transmittance with wavelength is due to the absorption

characteristics of the components of the encapsulation system and the spectral characteristics of antireflection coatings if they are used. The spectral transmittance will therefore be a fairly smooth function of wavelength. This allows us to break the integrals in eq. (5-6) into a number of spectral bands and to use values of  $C_\lambda$ ,  $I_\lambda$ , and  $T_\lambda$  that are averaged over each of the bands. Only the averaged values of transmittance need be calculated for each encapsulation system. The integrals in eq. (5-6) can thus be approximated as

$$\int_0^\infty C_\lambda I_\lambda T_\lambda d\lambda = C_{\lambda 1} I_{\lambda 1} T_{\lambda 1} + C_{\lambda 2} I_{\lambda 2} T_{\lambda 2} + \dots + C_{\lambda M} I_{\lambda M} T_{\lambda M} \quad (5-26)$$

$$\int_0^\infty C_\lambda I_\lambda d\lambda = C_{\lambda 1} I_{\lambda 1} + C_{\lambda 2} I_{\lambda 2} + \dots + C_{\lambda M} I_{\lambda M} \quad (5-27)$$

where the subscripts  $\lambda 1$ ,  $\lambda 2$ , ...,  $\lambda M$  refer to  $M$  spectral bands covering the solar spectrum.  $C_{\lambda i}$  and  $T_{\lambda i}$  are the spectral power conversion efficiency and the transmittance of the encapsulation system averaged over spectral band  $\lambda i$ .  $I_{\lambda i}$  is the intensity of incident solar radiation averaged over spectral band  $\lambda i$ .

If the spectral bands are chosen such that the amount of solar radiation in each band is the same, then the solar radiation quantities in each term in eqs. (5-26) and (5-27) cancel out when substituted into eq. (5-6). Setting  $I_{\lambda 1} = I_{\lambda 2} = \dots = I_{\lambda M} = I_\lambda^*$ , eqs. (5-26) and (5-27) become

$$\int_0^\infty C_\lambda I_\lambda T_\lambda d\lambda = I_\lambda^* (C_{\lambda 1} T_{\lambda 1} + C_{\lambda 2} T_{\lambda 2} + \dots + C_{\lambda M} T_{\lambda M}) \quad (5-28)$$

$$\int_0^\infty C_\lambda I_\lambda d\lambda = I_\lambda^* (C_{\lambda 1} + C_{\lambda 2} + \dots + C_{\lambda M}) \quad (5-29)$$

Substituting these results into eq. (5-6) and cancelling the  $I_\lambda^*$ 's gives the following approximate equation for calculating the effective transmittance of an encapsulation system.

$$T_{\text{eff}} = \frac{PE}{P} = \frac{C_{\lambda 1} T_{\lambda 1} + C_{\lambda 2} T_{\lambda 2} + \dots + C_{\lambda M} T_{\lambda M}}{C_{\lambda 1} + C_{\lambda 2} + \dots + C_{\lambda M}} \quad (5-30)$$

For the air mass 1.0 spectrum, the fraction of incident solar energy in wavelength band, 0 to  $\lambda$ , is plotted as a function of  $\lambda$  in Figure 5-11. This data is for clear but polluted air, as might be found near large cities or industrial areas. Listed in Table 5-2 are the wavelengths at five percent total solar radiation intervals. This allows choosing 1, 2, 4, 5, 10, or 20 spectral bands depending on the smoothness of the  $T_{\lambda}$  function or the availability of data on the optical properties of materials making up the encapsulation system.

Once the spectral bands have been chosen, averaged values for  $C_{\lambda}$  and the appropriate optical properties of the materials in the encapsulation system need to be determined. The next step is to use the radiosity-irradiation analysis to determine the amount of incident solar radiation absorbed in each layer of the encapsulation system for each of the chosen spectral bands.

### 5.3.2 Radiosity-Irradiation Equations

The radiosity-irradiation analysis, introduced in Section 5.2.4 and developed in detail below, is straightforward and convenient for analyzing the specular reflections within an encapsulation system. Specular reflections typically account for most of the radiant energy transfer in the module. Analysis of diffuse reflections and scattering within an encapsulation system (including the effect of weathering of the top cover) requires a significant increase in complexity in the radiation-irradiation model and also requires knowledge of the scattering and diffuse reflectivity properties of the encapsulation materials. Since this information is not presently available and may be difficult to determine, it is assumed that all reflections are specular. The subject of diffuse reflections within the encapsulation system has been identified as a technology void in Section 7 of this report.

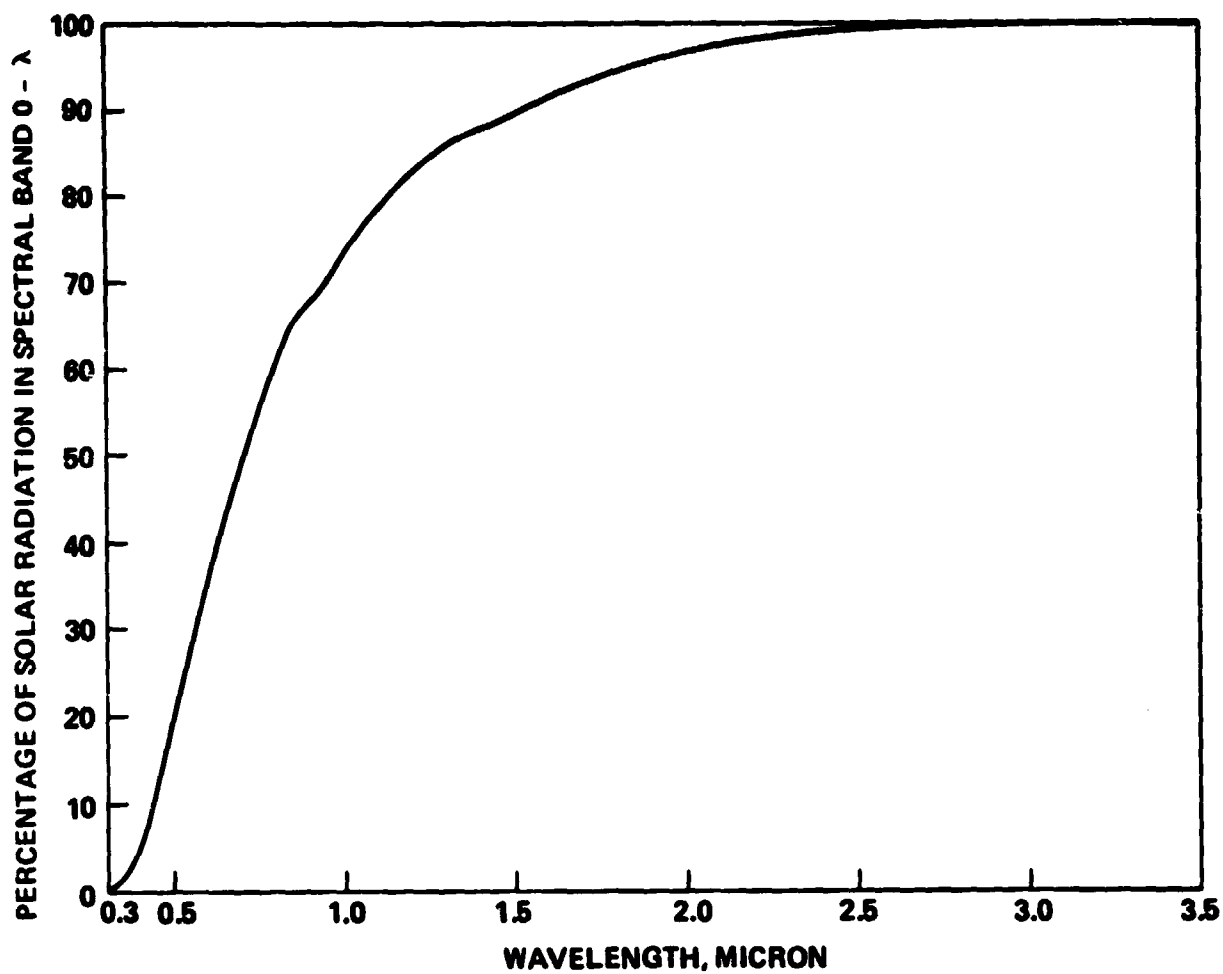


Figure 5-11. Percentage of Solar Radiation in Spectral Band 0-λ for Air Mass One, U.S. Standard Atmosphere, 20 mm Precipitable Water Vapor, and 3.4 mm Ozone



TABLE 5-2. Wavelengths at 5 Percent Intervals for Total Solar Radiation in Spectral Region 0 to  $\lambda$ : Air Mass One, U.S. Standard Atmosphere, 20mm Precipitable Water Vapor, 3.4mm Ozone,  $\alpha = 0.66$ ,  $\beta = 0.085$

$\lambda$  - Wavelength, micron

$F_{0-\lambda}$  - Percentage of solar irradiation in spectral band 0 -  $\lambda$ .

Total solar energy flux =  $890 \text{ W/m}^2$

$\lambda$	$F_{0-\lambda}$	$\lambda$ , micron	$F_{0-\lambda}$
0.403	5	0.752	55
0.443	10	0.798	60
0.475	15	0.851	65
0.505	20	0.964	70
0.537	25	1.044	75
0.570	30	1.154	80
0.603	35	1.277	85
0.638	40	1.573	90
0.673	45	1.892	95
0.711	50	4.32	100

The radiosity-irradiation model and the radiative fluxes involved for a general cross-section through a photovoltaic module are shown in Figure 5-12. The model consists of the front cover, transparent pottant, and a solar cell. This network model takes into account the reflectivity and transmissivity of each surface ( $\rho_1$ ,  $\rho_2$ ,  $\tau_1$ , and  $\tau_2$ ), the thickness and absorption coefficient of each layer ( $t_1$ ,  $t_2$ ,  $a_1$ ,  $a_2$ ), and the reflectivity of the solar cell ( $\rho_c$ ). These quantities should be average values over the spectral bands chosen. The energy absorbed per unit area of module surface in

the two cover layers and in the solar cell are  $q_1$ ,  $q_2$ , and  $q_c$  as indicated in Figure 5-12. The complete set of radiosity-irradiation equations to be solved simultaneously are as follows:

$$\begin{aligned}
 q_1^- &= 1 \text{ (Solar irradiation normalized to one)} \\
 q_1^+ &= \rho_1 q_1^- + \tau_1 q_2^- \\
 q_2^- &= \tau_1 q_1^+ \\
 q_2^+ &= \tau_1 q_1^- + \rho_1 q_2^- \\
 q_3^- &= \tau_1 q_2^+ \\
 q_3^+ &= \rho_2 q_3^- + \tau_2 q_4^- \\
 q_4^- &= \tau_2 q_3^+ \\
 q_4^+ &= \tau_2 q_3^- + \rho_2 q_4^- \\
 q_5^- &= \tau_2 q_4^+ \\
 q_5^+ &= \rho_c q_5^-
 \end{aligned} \tag{5-31}$$

where,

$$\begin{aligned}
 \tau_1 &= e^{-a_1 t_1} \\
 \tau_2 &= e^{-a_2 t_2}
 \end{aligned} \tag{5-32}$$

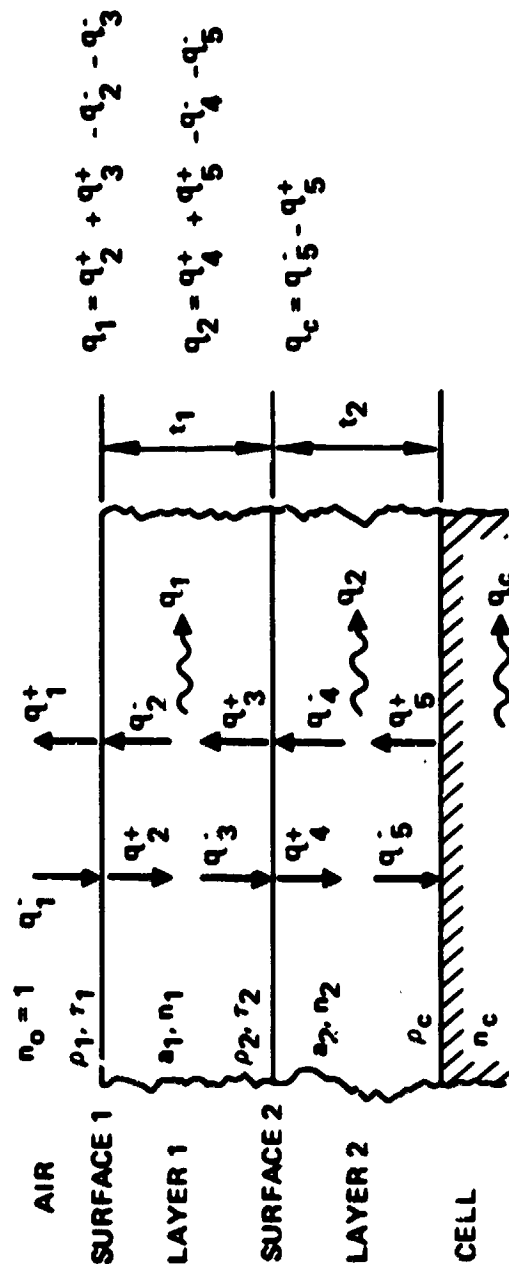


Figure 5-12. Radiosity-Irradiation Network for Front Cover, Transparent Pottant, and Solar Cell.

The simultaneous set of eqs. (5-31) is easily reduced to the following set of equations:

$$\begin{aligned}
 A &= \rho_c \tau_2^2 T_2^2 \\
 B &= 1 - \rho_c \rho_2 \tau_2^2 \\
 q_2^+ &= \frac{1 - \rho_1}{1 - \rho_1 \tau_1^2 \left( \rho_2 + \frac{A}{B} \right)} \quad (5-33) \\
 q_3^+ &= q_2^+ \tau_1 \left( \rho_2 + \frac{A}{B} \right) \\
 q_1^+ &= \rho_1 + \tau_1 \tau_1 q_3^+ \\
 q_4^+ &= \frac{q_2^+ \tau_1 \tau_2}{B} \\
 q_5^+ &= \rho_c \tau_2 q_4^+
 \end{aligned}$$

The fraction of the incident solar energy absorbed in each layer is obtained from the following energy balances:

$$\begin{aligned}
 q_1 &= q_2^+ + q_3^+ - q_2^- - q_3^- \\
 &= (q_2^+ + q_3^+) (1 - \tau_1) \\
 q_2 &= q_4^+ + q_5^+ - q_4^- - q_5^- \quad (5-34) \\
 &= q_4^+ (1 - \tau_2) (1 - \rho_c \tau_2) \\
 q_c &= q_5^- - q_5^+ \\
 &= q_4^+ \tau_2 (1 - \rho_c)
 \end{aligned}$$

Equation sets (5-31), (5-32), and (5-33) are then solved for the specular radiant energy fluxes within the encapsulation system. This analysis is carried out for each of the equal-energy spectral bands of the solar spectrum.

In the absence of antireflection coatings, the reflectivities  $\rho_1$ ,  $\rho_2$ , and  $\rho_c$  can be calculated from eq. (5-35), which are the small-angle approximations of Fresnel's equation (eq. 5-7).

$$\begin{aligned}\rho_1 &= \left( \frac{N_1 - 1}{N_1 + 1} \right)^2 \\ \rho_2 &= \left( \frac{N_2 - N_1}{N_2 + N_1} \right)^2 \\ \rho_c &= \left( \frac{N_c - N_2}{N_c + N_2} \right)^2\end{aligned}\tag{5-35}$$

If surface 1 or the surface of the solar cell have antireflection coatings or special surface preparations, then their actual reflectivity and transmissivity values should be used in lieu of eqs. (5-35).

Once  $q_c$ ,  $q_1$ , and  $q_2$  have been calculated for each spectral band, the effective transmittance of the encapsulation system and the fraction of incident energy absorbed in each layer can be determined. The spectral transmittance of the encapsulation system averaged over spectral band  $\lambda i$  is  $q_c$  calculated for spectral band  $\lambda i$  or  $q_{c\lambda i}$ . Therefore the effective transmittance can be determined from eq. (5-30) with the  $q_{\lambda i}$ 's replacing the  $T_{c\lambda i}$ 's

$$T_{\text{eff}} = \frac{C_{\lambda 1} q_{c\lambda 1} + C_{\lambda 2} q_{c\lambda 2} + \dots + C_{\lambda M} q_{c\lambda M}}{C_{\lambda 1} + C_{\lambda 2} + \dots + C_{\lambda M}}\tag{5-36}$$

### 5.3.3 Summary of Analytical Procedure

1. Required information
  - a). Solar cell spectral power-conversion efficiency or relative spectral response,  $C_\lambda$ .
  - b). Thicknesses of encapsulation layers,  $t_1$  and  $t_2$ .

- c). Absorption coefficients,  $a_1$  and  $a_2$ , as function of  $\lambda$
  - d). Reflectivities of outer layer,  $\rho_1$ , and solar cell,  $\rho_c$ , as functions of  $\lambda$  if they have been specially treated to reduce reflections. Otherwise, they can be calculated from indices of refraction,  $N_1$ ,  $N_2$ , and  $N_c$ .
2. Based upon the wavelength dependence of the above quantities, decide on the number,  $M$ , of equal-energy spectral bands for the solar spectrum. [20 bands are used in the present analysis]. Determine average values of the above quantities for each of these spectral bands.
  3. Solve the radiosity-irradiation equations for each of the  $M$  spectral bands.
    - a). Calculate layer transmittances,  $T_1$  and  $T_2$ , from eq. (5-32).
    - b). Calculate reflectivities,  $\rho_1$ ,  $\rho_2$ , and  $\rho_c$ , if not specified, from eq. (5-35).
    - c). Solve for radiosities,  $q_2^+$ ,  $q_3^+$ , and  $q_4^+$ , from eq. (5-34).
    - d). Solve for fraction of incident energy absorbed in the cell and in each layer,  $q_1$ ,  $q_2$ , and  $q_c$ , from eq. (5-34).
  4. Calculate the effective transmittance,  $T_{eff}$ , of the encapsulation system from eq. (5-36).
  5. Calculate total amount of incident solar radiation absorbed in each layer. For example,

$$Q_1 = A \sum_{i=1}^M q_{1\lambda i}$$

Where  $A$  is the appropriate area of the layer normal to the sunline.

## 6.0 THERMAL ANALYSIS

### 6.1 INTRODUCTION

The electrical power output from a photovoltaic module is strongly influenced by the thermal and optical characteristics of the module encapsulation system. Described in this section are the methodology and computer model for performing fast and accurate thermal and optical evaluations of different encapsulation systems. The computer model is used to evaluate cell temperature, solar energy transmittance through the encapsulation system, and electrical power output in a terrestrial environment. Extensive results are presented for both glass superstrate modules and substrate modules with different types of silicon cell materials, pottants, and anti-reflection coatings.

### 6.2 BASIC EQUATIONS

#### 6.2.1 Overview

As mentioned previously in Section 5, solar radiation incident on a photovoltaic module is partially reflected from and partially absorbed by the module. The radiant energy absorbed by the module is converted partially to heat and partially to electricity. The absorbed solar energy converted to heat leads to a module temperature greater than that of the surrounding environment. At steady-state, the absorbed solar energy is equal to the electrical energy generated by the cells plus the heat lost from the module to the surrounding environment. Heat losses from the module are due to air flow past the module (convection) and to radiation to the ground and sky.\* Since

---

\*There may also be radiant energy exchange between neighboring modules in a large array field. This aspect is not treated in this report but has been identified as a technology void in Section 7.

the conversion efficiency of a solar cell decreases with increasing temperature, it is desirable to minimize the temperature difference between the cell and the surrounding environment.

#### 6.2.2 Assumptions

The optical and thermal aspects of module design are closely related in that the heat absorbed by the module is determined by the optical properties of the encapsulation system and by the conversion efficiency of the cells. These properties are wavelength dependent, and some of these properties (e.g. reflectivity) are directionally dependent as well. The intensity and spectral energy distribution of the illumination source, in this case the sun, are also important factors in the analysis. In addition, solar energy contains both direct and diffuse components. In the light of these complicating factors, the following assumptions were made to simplify the analysis:

- The indices of refraction of the cells, the front cover, and transparent pottant of the encapsulation system are independent of wavelength
- The plane of the module is perpendicular to the sunline
- Absorption-reradiation phenomena in the encapsulation system are ignored
- Optical properties are independent of temperature and direction
- Incident solar radiation is direct (i.e. no diffuse component)

The third assumption permits the decoupling of the optical and thermal analyses by specifying that the radiant energy absorbed in the front cover, the transparent pottant, the cells, and the opaque pottant between cells is not reradiated. This means that conduction is the only mechanism by which heat can flow from the interior to the surface of the module. In addition, this assumption permits the exclusion of thermal radiation from the front surface of the module in the optical analysis (see Section 5.2.4).



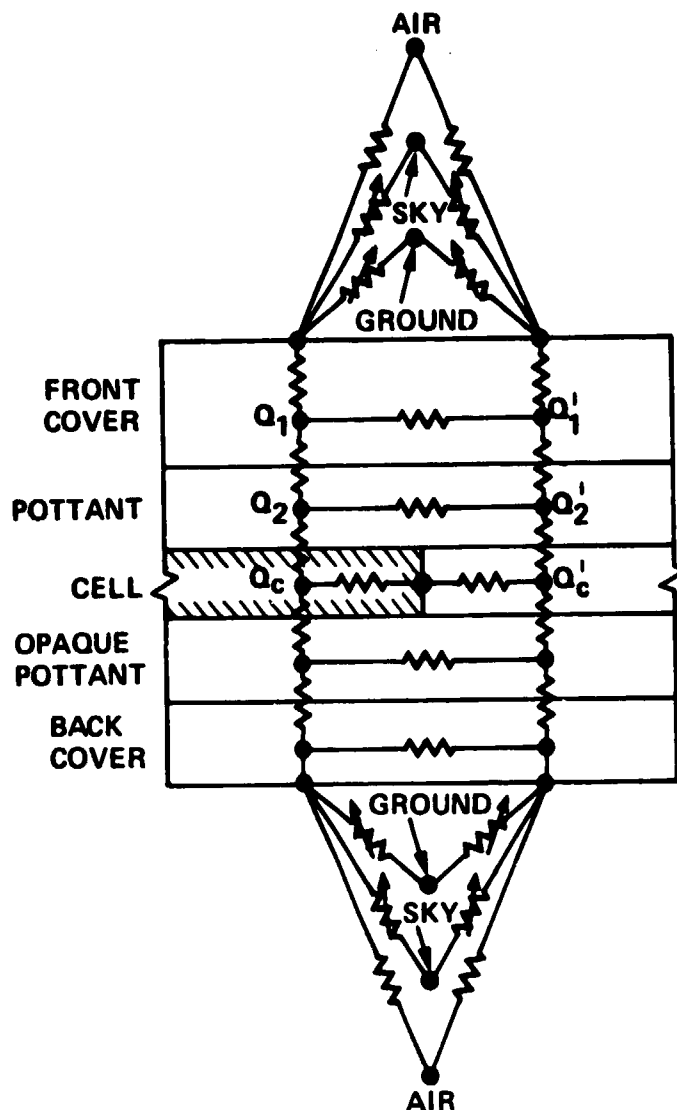


Figure 6-1. Thermal Network for Encapsulated Photovoltaic Cell

### 6.2.3 Basic Equations - Thermal Analysis

A discrete-element thermal model, which is shown in Figure 6-1, was used to determine the temperature distribution around a centrally located cell inside a module. The area to the immediate right of the cell is white-pigmented (opaque) pottant in the interstitial space between neighboring cells. The large black dots inside and on the surface of the module (as shown in Figure 6-1) represent points (nodes) where the temperature was calculated. The large dots external to the module represent constant temperature

boundaries (i.e. the thermal environment); in this case the boundaries are the ground, air, and sky.

The solar energy absorbed by the module is indicated for the appropriate nodes in Figure 6-1. Values of  $Q_1$ ,  $Q_1'$ ,  $Q_2$ ,  $Q_2'$ ,  $Q_c$  and  $Q_c'$  were determined by the method outlined in Section 5.

The nodes are connected by a network of heat flow paths, which are shown as resistors in Figure 6-1. Each path represents a finite "resistance" to heat flow in the model. As mentioned in Section 6.2.2, absorption-reradiation phenomena in the encapsulation system are ignored, and heat flow inside the module is therefore by conduction only. The conduction resistance between adjacent nodes  $i$  and  $j$  is given by

$$R_{ij} = \frac{l_{ij}}{kA} \quad (6-1)$$

where  $l_{ij}$  is the distance between nodes,  $k$  is the thermal conductivity, and  $A$  is the cross-sectional area for conductive heat flow.

Air motion (convection) past the module surfaces helps to remove the solar radiation absorbed as heat. The thermal resistance to this convective heat flow from the surface to air is given by

$$R_{s-air} = 1/(hA) \quad (6-2)$$

where  $h$  is the convective heat transfer coefficient and  $A$  is the cross-sectional area for convective heat flow. The following relation [21, 22, 24] is used to calculate  $h$ :

$$h = 1.247 \times 10^{-4} (\Delta T \cos X)^{1/3} + 2.685 \times 10^{-4} V \quad (6-3)$$

where  $\Delta T = T_{\text{surface}} - T_{\text{air}}$ ,  $X$  is the tilt angle between the backside of the module and the ground, and  $V$  is the air velocity

The module surfaces also radiate to the ground and sky. The thermal resistance to radiation between a module surface node and a radiation boundary is given by [23]

$$R_{s-b} = (A\epsilon_s \sigma F_{s-b})^{-1} \quad (6-4)$$

where  $\epsilon_s$  is the emissivity of the module surface,  $\sigma$  is the Stefan-Boltzman constant,  $F_{s-b}$  is the shape factor for radiation from the module to boundary b, and A is the area for radiative heat flow. Note that the units of eqs. (6-1) and (6-2) are °C/W, and that the units of eq. (6-4) are °K<sup>4</sup>/W. This is the way the thermal resistances are input to the thermal analyzer program which is discussed later in Section 6.3

It is assumed here that the views of the ground and sky from the module are not obscured by other modules in the array field; thus, the shape factors are given by

$$F_{s\text{-ground}} = 1/2 (1 - \cos X) \quad (6-5)$$

$$F_{s\text{-sky}} = 1 - F_{s\text{-ground}} \quad (6-6)$$

where X = angle between module surface and the ground (  $\leq 90^\circ$  for backside;  
 $\geq 90^\circ$  for sunside)

#### 6.2.4 Determination of Electric Power Generation

The electrical energy produced by the cell is given by

$$P = A_c S \int_0^\infty C_\lambda q_c d\lambda \quad (6-7)$$

$$= nQ_c \quad (6-8)$$

where  $C_\lambda$  is the spectral power conversion efficiency of the cell, S is the solar flux,  $n$  is the overall conversion efficiency, and  $A_c$  is the cell area.

The overall conversion efficiency depends on cell temperature in the following manner [16]

$$n = n(28^\circ\text{C}) [1 - .005(T - 28^\circ\text{C})] \quad (6-9)$$

Typical values of  $C_\lambda$  for silicon are shown in Figure 5-3, and typical values of  $n$  at 28°C are listed in Table 5-1.

### 6.3 COMPUTATIONAL SEQUENCE

The core of the thermal/optical model is CINDA-3G, an existing thermal analyzer program modified to accept a subroutine that accounts for reflection, absorption, and transmission of solar radiation in the encapsulation system. The output of the optical subroutine is input directly to the thermal analyzer portion of the program. The program is flexible in that thermal properties of different encapsulation materials and cell materials (e.g. silicon, gallium arsenide, etc.) can be accommodated easily. Input data for the optical portion of the program are the spectral intensity of the light source (e.g. sun, solar simulators, etc.), the appropriate wavelength bands, and material properties that correspond to the midpoint of each band. Values of optical properties versus wavelength are found in Appendix A.

The solar spectrum is divided into a sufficient number of equal-energy intervals to accurately represent the complexity of the spectrum. Twenty equal-energy intervals were used in the present analysis. Corresponding to these energy intervals are 20 wavelength bands of unequal size.

As noted previously, the fluxes  $q_1$ ,  $q_2$ , and  $q_c$  are wavelength dependent due to the wavelength dependence of the incident solar flux and the properties  $\rho$  and  $\tau$ . These fluxes are evaluated at the wavelength corresponding to the midpoint of each of the 20 wavelength bands. Summing these quantities over the 20 equal energy intervals and multiplying by the appropriate nodal area yields values for the heat absorbed in each layer of the encapsulation system and for the radiant energy absorbed by the cell.

To determine electrical power output, the spectral power-conversion efficiency,  $C_\lambda$ , is multiplied by  $A_c S q_c$  prior to summation over all wavelength bands. This quantity represents the electrical power output at the reference temperature of 28°C. Being temperature independent, this quantity is calculated initially and used as input for the remainder of the program execution. The temperature dependence of the overall conversion efficiency,  $\eta$  as well as that of the convective heat transfer coefficient is included in the CINDA iterative solution to determine the temperature distribution within the module.

For open circuit conditions all of the solar energy transmitted to the cell is converted to heat.

#### 6.4 COMPUTER PROGRAM

As noted in Section 6.3, the CINDA-3G thermal analyzer program is used in the present study. The input data for this program consists of data blocks which define nodes, connectors, constants, and property data in addition to other data blocks called EXECUTION, VARIABLES 1, VARIABLES 2, and OUTPUT CALLS.

The EXECUTION block accepts the FORTRAN statements which constitute the optical preprocessor subroutine. Spectral properties of encapsulation materials are stored in the block called ARRAY DATA. The radiative connectors, being temperature independent, are calculated in the EXECUTION block. The convective heat transfer coefficient and the overall conversion efficiency are temperature dependent and are continually updated with each solution iteration in the VARIABLES 1 data block.

The computer code for the thermal/optical model can easily account for spectral and temperature dependant properties of encapsulation materials, solar cell materials, and surface emissivities of the module. Prior to running the computer program, a matrix of layer thickness and thermal conductivity is created and subsequently merged into the program input data. The model can handle module designs containing up to six material layers.

#### 6.5 RESULTS

##### 6.5.1 Encapsulation System Parameters

The encapsulation system parameters investigated in this study are summarized in Table 6-1. A summary of thermal and optical properties is found in Appendix A for different materials used in photovoltaic modules.

##### 6.5.2 Thermal Environment

The thermal environment parameters used in this study are the following:

- Incident solar flux ( $S$ ) =  $0.114 \text{ w/cm}^2$  (normal incidence, AM 1.5 spectrum)

- Air temperature = 20°C
- Ground temperature = 20°C
- Sky temperature = -5.2°C
- Air velocity = 1 meter/sec (parallel to ground)
- Tilt angle = 37° relative to local horizontal

The only difference between the above conditions and those specified by JPL [9, 10] for calculation of the NOCT (Nominal Operating Cell Temperature) is the incident solar flux; JPL specified an incident flux of 0.08 w/cm<sup>2</sup> whereas 0.114 w/cm<sup>2</sup> was used in the present study.\*

### 6.5.3 Discussion

As shown in Tables 6-3 thru 6-5, the output electrical power is greatest for single crystal silicon and least for amorphous silicon. Not surprisingly, the cell temperature is lowest for single crystal silicon and highest for amorphous silicon. For open circuit conditions, cell temperature is the same regardless of cell type. It was also found that backside emissivity of the module exerts a significant influence on cell temperature. For example, increasing backside emissivity from .58 to .92 leads to a 3.1°C decrease in cell temperature. For best performance, the backside emissivity should be .85 or higher. The subject of backside emissivity is discussed further in section 6.6.

The thicknesses of the encapsulation layers do not exert a large influence on cell temperature and electrical power output. In a superstrate module, for example (Table 6-3), a three-fold increase in pottant thickness (from 5 mil to 15 mil) results in a 0.9°C rise in cell temperature and a corresponding 0.02-watt decrease in electrical output. Doubling the thickness of no-iron

---

\*As shown in Appendix C, the radiant energy flux for AM 1.5 is .097 w/cm<sup>2</sup>. This information was not available at the time when the majority of the thermal/optical calculations were performed. A rough numerical integration over 20 equal-energy intervals yielded the high value of 0.114 w/cm<sup>2</sup>. A large number of intervals (>100) is required to obtain the lower value of .097 w/cm<sup>2</sup>.

TABLE 6-1. Summary of Encapsulation System Parameters Studied for Superstrate and Substrate Modules

Superstrate Modules	Substrate Modules
<ul style="list-style-type: none"> <li>• Transparent Load-Bearing Member <ul style="list-style-type: none"> <li>• No-Iron Glass</li> <li>• Medium-Iron Glass</li> <li>• High-Iron Glass</li> </ul> </li> <li>• Pottant <ul style="list-style-type: none"> <li>• EVA</li> <li>• EVA/Craneglass</li> <li>• Other Materials</li> </ul> </li> <li>• Cells (Silicon) <ul style="list-style-type: none"> <li>• Single Crystal (<math>n = 16.3</math> percent)</li> <li>• Polycrystalline (<math>n = 9.9</math> percent)</li> <li>• Amorphous (<math>n = 5.8</math> percent)</li> </ul> </li> <li>• Antireflection Coatings <ul style="list-style-type: none"> <li>• On Cell <ul style="list-style-type: none"> <li>• None</li> <li>• Optimized for Air/Silicon Interface</li> <li>• Optimized for Pottant/Silicon Interface</li> <li>• <math>TiO_2</math></li> <li>• Texturized Only</li> <li>• <math>TiO_2</math> and Texturized Surface</li> </ul> </li> <li>• On Glass <ul style="list-style-type: none"> <li>• Optimized for Air/Glass Interface <ul style="list-style-type: none"> <li>o One Side</li> <li>o Both Sides</li> </ul> </li> </ul> </li> </ul> </li> </ul>	<ul style="list-style-type: none"> <li>• Structural Substrate <ul style="list-style-type: none"> <li>• Mild Steel</li> <li>• Unribbed</li> <li>• Ribbed</li> <li>• Wood</li> <li>• Unribbed</li> <li>• Ribbed</li> </ul> </li> <li>• Transparent Front Cover <ul style="list-style-type: none"> <li>• Korad (<math>\epsilon_s = 0.80</math>)</li> <li>• Tedlar (<math>\epsilon_s = 0.89</math>)</li> </ul> </li> <li>• Pottant <ul style="list-style-type: none"> <li>• EVA</li> <li>• EVA/Craneglass</li> <li>• Other Materials</li> </ul> </li> <li>• Cells (Silicon) <ul style="list-style-type: none"> <li>• Single Crystal (<math>n = 16.3</math> percent)</li> <li>• Polycrystalline (<math>n = 9.9</math> percent)</li> <li>• Amorphous (<math>n = 5.8</math> percent)</li> </ul> </li> <li>• Antireflection Coatings on Cell <ul style="list-style-type: none"> <li>• Optimized for Air/Silicon Interface</li> <li>• Optimized for Pottant/Silicon Interface</li> <li>• <math>TiO_2</math></li> <li>• Texturized Only</li> <li>• <math>TiO_2</math> and Texturized</li> </ul> </li> </ul>

Table 6-3. Thermal/Optical Performance of Glass Superstrate Modules with Silicon Cells.

Cell			Glass				Pottant			Calculated Results(2)		
Type(1)	AR-Coating	Iron Content	Thickness, mil	AR-Coating	Material	Thickness, mil	Backside Emissivity	Open Circuit Power Generation	Cell Temp, °C	Cell Output Power, w		
SC - non text	None	No	125	None	EVA/CG	5	0.92(3)	53.5	49.0	1.33		
SC - non text	None	No	125	None	EVA/CG	10	0.92	54.1	49.5	1.32		
SC - non text	None	No	125	None	EVA/CG	10	0.58(4)	57.2	52.4	1.30		
SC - non text	None	No	125	None	EVA/CE	15	0.92	54.4	49.9	1.31		
SC - non text	None	No	187.5	None	EVA/CG	10	0.92	54.5	50.0	1.31		
SC - non text	None	No	250	None	EVA/CG	10	0.92	54.9	50.4	1.30		
SC - non text	None	Medium	125	None	EVA/CG	10	0.92	54.3	50.0	1.27		
SC - non text	None	High	125	None	EVA/CG	10	0.92	54.9	50.8	1.19		
SC - non text	None	No	125	None	EVA/CG	10	0.92	58.2	53.2	1.47		
PC - non text	None	No	125	None	EVA/CG	10	0.92	54.1	51.4	0.78		
A - non text	None	No	125	None	EVA/CG	10	0.92	54.1	52.4	0.50		
SC - non text	None	No	125	Opt. for air/glass; air side only	EVA/CE	10	0.92	54.7	50.1	1.35		
SC - non text	None	No	125	Opt. for air/glass; both sides	EVA/CG	10	0.92	54.2	49.7	1.33		
SC - non text	Opt. for air/silicon	No	125	None	EVA/CG	10	0.92	58.5	53.4	1.53		
SC - non text	Opt. for pottant/silicon	No	125	None	EVA/CG	10	0.92	59.2	53.9	1.56		
SC - non text	TiO2	No	125	None	EVA/CG	10	0.92	58.3	53.2	1.52		
SC - non text	Opt. for pottant/silicon	No	125	Opt. for air/glass; both sides	EVA/CG	10	0.92	59.4	54.2	1.57		
SC - texturized	TiO2	No	125	None	EVA/CG	10	0.92	59.3	54.3	1.52		

Notes: (1) SC - single crystal silicon (efficiency = 16.3%)  
PC - polycrystalline silicon (efficiency = 9.9%)  
A - amorphous silicon (efficiency = 5.8%)

(2) Operational environment  
T<sub>air</sub> = 20°C  
T<sub>sky</sub> = -5.2°C  
T<sub>ground</sub> = 20°C  
Ground emissivity = 0.9  
Tilt angle = 37°  
Insolation = Air Mass 1.5 (normal incidence at 37° tilt)

(3) Aluminum foil with white Mylar on outside surface  
(4) Aluminized Mylar; Mylar is 0.5 mil thick



Table 6-4. Thermal/Optical Performance of Wood-Product Substrate Modules with Silicon Cells.

Cell		Front Cover			Pottant		Substrate			Back Cover			Calculated Results (2)	
Type (1)	AR-Coating	Material	Thickness, mil	Emissivity	Material	Thickness, mil	Material	Thickness, mil	Film (3)	Material	Thickness, mil	Emissivity	Open Circuit Voltage, V	Cell Output Power, W
SE - non test	None	Barred	3	0.06	EW/CS	5	Wood P.	125	0.4 in. x 2.0 in. spaced 8 in. apart	White EVA	30	0.09	56.5	1.32
SE - non test	None	Barred	3	0.06	EW/CS	10	Wood P.	125	-	White EVA	30	0.09	56.0	1.20
SE - non test	None	Barred	3	0.06	EW/CS	15	Wood P.	125	-	White EVA	30	0.09	56.3	1.29
SE - non test	None	Barred	3	0.06	EW/CS	5	Wood P.	250	None	White EVA	30	0.09	57.5	1.30
SE - non test	None	Barred	3	0.06	EW/CS	10	Wood P.	250	None	White EVA	30	0.09	58.2	1.29
SE - non test	None	Barred	3	0.06	EW/CS	15	Wood P.	250	None	White EVA	30	0.09	58.6	1.28
SE - non test	None	Teflon	3	0.09	EW/CS	5	Wood P.	125	0.4 in. x 2.0 in. spaced 8 in. apart	White EVA	30	0.09	55.2	1.31
SE - non test	None	Teflon	3	0.09	EW/CS	10	Wood P.	125	-	White EVA	30	0.09	55.8	1.30
SE - non test	None	Teflon	3	0.09	EW/CS	15	Wood P.	125	-	White EVA	30	0.09	56.1	1.29
SE - non test	None	Teflon	3	0.09	EW/CS	5	Wood P.	250	None	White EVA	30	0.09	57.4	1.30
SE - non test	None	Teflon	3	0.09	EW/CS	10	Wood P.	250	None	White EVA	30	0.09	58.0	1.29
SE - non test	None	Teflon	3	0.09	EW/CS	15	Wood P.	250	None	White EVA	30	0.09	58.3	1.28
PC - non test	None	Barred	3	0.06	EW/CS	10	Wood P.	125	0.4 in. x 2.0 in. spaced 8 in. apart	White EVA	30	0.09	55.0	0.77
PC - non test	None	Teflon	3	0.09	EW/CS	10	Wood P.	125	-	White EVA	30	0.09	55.0	0.77
A - non test	None	Barred	3	0.06	EW/CS	10	Wood P.	125	-	White EVA	30	0.09	56.0	0.69
A - non test	None	Teflon	3	0.09	EW/CS	10	Wood P.	125	-	White EVA	30	0.09	56.0	0.69

Notes: (1) SE - Single crystal silicon (efficiency = 16.3%)  
 PC - Polycrystalline silicon (efficiency = 9.9%)  
 A - Amorphous silicon (efficiency = 5.8%)

(2) Operational environment  
 T<sub>air</sub> = 20°C  
 T<sub>sky</sub> = -5.2°C  
 T<sub>ground</sub> = 20°C  
 Ground emissivity = 0.9  
 Tilt angle = 37°  
 Insolation = Air Mass 1.5 (normal incidence at 37° tilt)

(3) Film substrate matching to heat dissipation capability of module with used product substrate

Table 6-5. Thermal/Optical Performance of Steel Substrate Modules with Silicon Cells.

Cell		Front Cover			Postant		Substrate			Back Cover			Calculated Results (2)	
Type (1)	IR Coating	Material	Thickness, mil	Emissivity	Material	Thickness, mil	Material	Thickness, mil	Fins (3)	Material	Thickness, mil	Emissivity	Open Circuit Voltage, V	Power, W
SC - non test	None	Corad	3	0.06	EM/CS	5	P1 Steel	200	None	Porcelain	10	0.03	51.0	46.9
SC - non test	None	Corad	3	0.06	EM/CS	10	P1 Steel	200	None	Porcelain	10	0.03	52.0	46.3
SC - non test	None	Corad	3	0.06	EM/CS	15	P1 Steel	200	None	Porcelain	10	0.03	53.4	46.9
SC - non test	None	Tedlar	3	0.09	EM/CS	5	P1 Steel	200	None	Porcelain	10	0.03	51.6	46.9
SC - non test	None	Tedlar	3	0.09	EM/CS	10	P1 Steel	200	None	Porcelain	10	0.03	52.6	46.1
SC - non test	None	Tedlar	3	0.09	EM/CS	15	P1 Steel	200	None	Porcelain	10	0.03	53.7	46.7
SC - non test	None	Corad	3	0.06	EM/CS	10	P1 Steel	200	None	White EMI	10	0.09	53.0	46.5
SC - non test	None	Tedlar	3	0.09	EM/CS	10	P1 Steel	200	None	White EMI	10	0.09	52.9	46.4
SC - non test	None	Corad	3	0.06	EM/CS	5	P1 Steel	70	0.2 in. x 1.5 in. spaced 8 in. apart	Porcelain	10	0.03	48.9	44.6
SC - non test	None	Corad	3	0.06	EM/CS	10	P1 Steel	70	-	Porcelain	10	0.03	50	45.0
SC - non test	None	Corad	3	0.06	EM/CS	15	P1 Steel	70	-	Porcelain	10	0.03	50.6	46.3
SC - non test	None	Tedlar	3	0.09	EM/CS	5	P1 Steel	70	-	Porcelain	10	0.03	49.2	44.6
SC - non test	None	Tedlar	3	0.09	EM/CS	10	P1 Steel	70	-	Porcelain	10	0.03	50.2	46.0
SC - non test	None	Tedlar	3	0.09	EM/CS	15	P1 Steel	70	-	Porcelain	10	0.03	50.7	46.5
SC - non test	None	Corad	3	0.06	EM/CS	10	P1 Steel	70	-	White EMI	10	0.09	50.2	46.0
SC - non test	None	Tedlar	3	0.09	EM/CS	10	P1 Steel	70	-	White EMI	10	0.09	50.1	45.9

Notes: (1) SC - Single crystal silicon (efficiency = 16.3%)

(2) Operational environment

Ground emissivity = 0.9

Tilt angle = 37°

Insulation = Air Mass 1.5 (normal) for balance at 37° tilt)

T<sub>air</sub> = 20°C

T<sub>sky</sub> = -5.2°C

T<sub>ground</sub> = 20°C

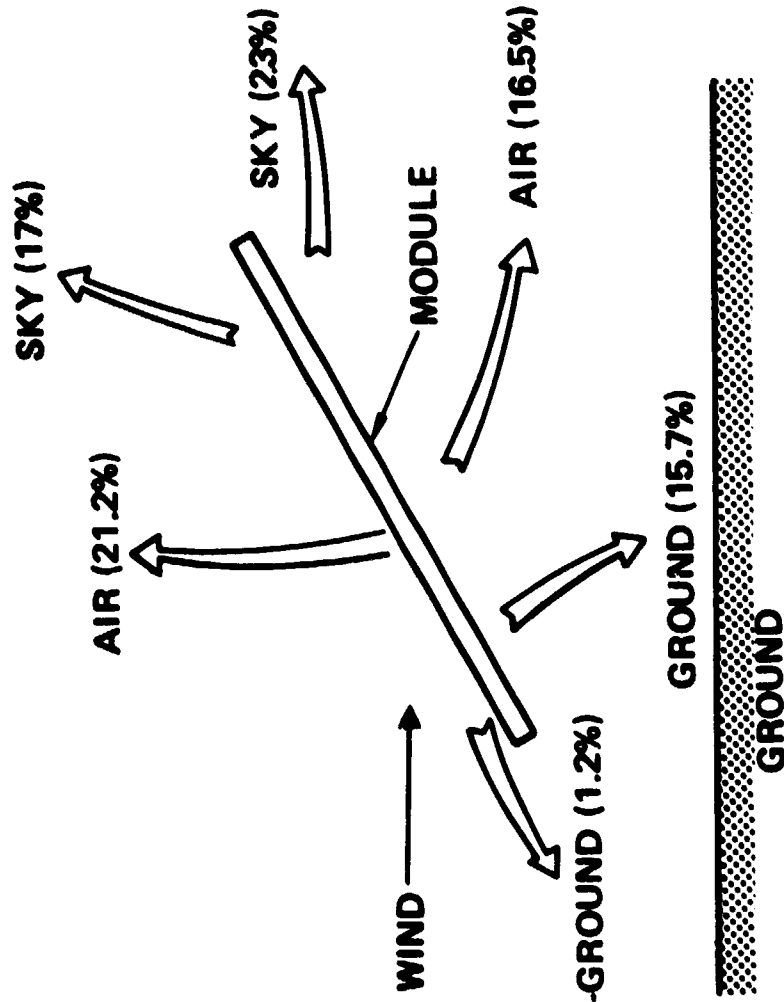
glass (from 125 mil to 250 mil) results in a modest  $.9^{\circ}\text{C}$  increase in cell temperature and a 0.02-watt decrease in electrical power output. These results indicate that the cell temperature and electrical power output are rather insensitive to large variations in the thermal resistance between the cell and module surface. Similar results were found for substrate modules, as indicated in Tables 6-4 and 6-5. The absence of Craneglas in the pottant layer above the cell did not significantly alter the above results (see Table 6-7).

Increasing the iron content of the glass leads to an increase in the solar energy absorbed by the glass and thus to a decrease in solar energy reaching the cell surface. As seen the Table 6-3, increasing the iron content can lead to about a 10 percent (from 1.32 watts to 1.19 watts) decrease in electrical output.

Module energy balances are shown in Figures 6-2 thru 6-6. Figures 6-2 through 6-4 show energy balances for superstrate modules using single-crystal, polycrystalline, and amorphous silicon cells. Figures 6-5 and 6-6 show energy balances for wood substrate and steel substrate modules using single crystal silicon cells. In those modules using low-efficiency, amorphous silicon cells, the radiative and convective heat losses off the module are roughly equal at 37.2 percent of the incident solar energy; approximately 21.5 percent of the incident solar energy is reflected off the modules, and 4.1 percent is converted to electric power. For a  $37^{\circ}$  tilt, about 5 percent more energy is lost from the front side than from the back side of the module. As the cell efficiency is increased, most of the heat lost from the modules occurs by radiation, as shown in Figures 6-5 and 6-6. The important conclusion drawn from Figures 6-2 through 6-6 is that cell temperature is influenced mainly by the external environment, not by materials used in the construction of the module.

The incorporation of ribs results in a cell temperature about  $2^{\circ}\text{C}$  less than that for an unribbed steel substrate module. Ribs have no effect on cell temperature for wood substrate modules.

# AMORPHOUS CELL

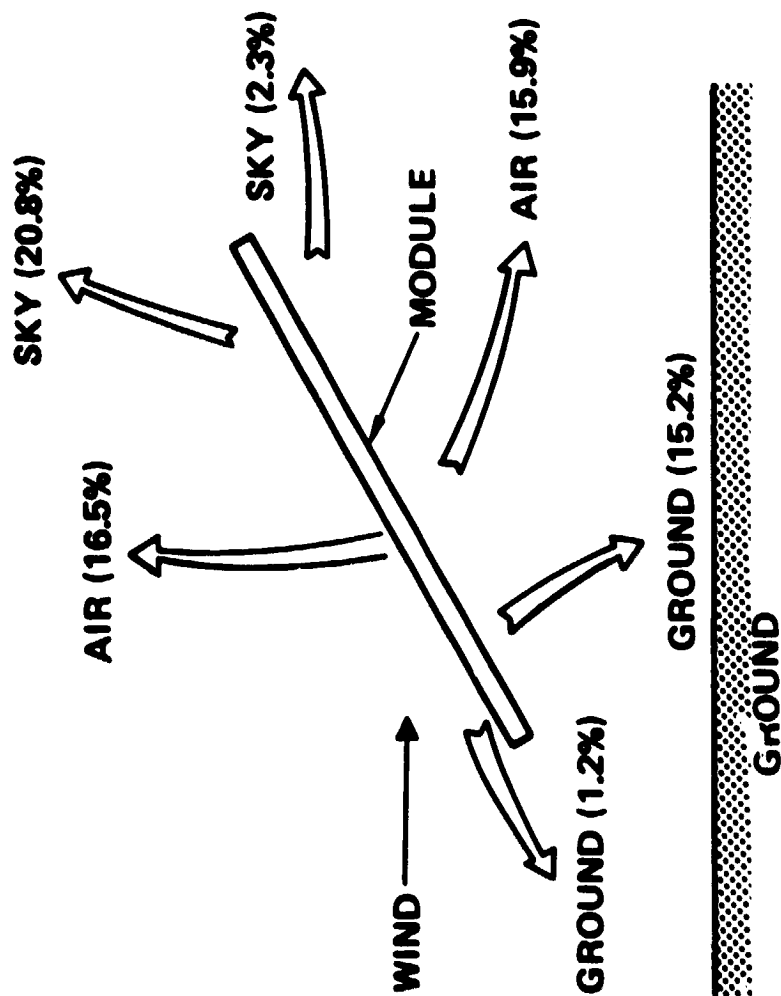


## GLASS COVER LAYE NO IRON

	POWER (w)	%
ELECTRICAL OUTPUT	0.50	4.1
ABSORBED (HEAT)	9.00	74.4
REFLECTED	2.59	21.5
TOTAL	12.09	100.0

Figure 6-2. Energy Balance for Glass Superstrate Module with Amorphous Silicon Cells

# POLYCRYSTALLINE CELL



GLASS COVER LAYER  
NO IRON

	POWER (w)	%
ELECTRICAL OUTPUT	0.78	6.5
ABSORBED (HEAT)	8.71	72.0
REFLECTED	<u>2.59</u>	<u>21.5</u>
TOTAL	12.08	100.0

Figure 6-3. Energy Balance for Glass Superstrate Module with Polycrystalline Silicon Cells

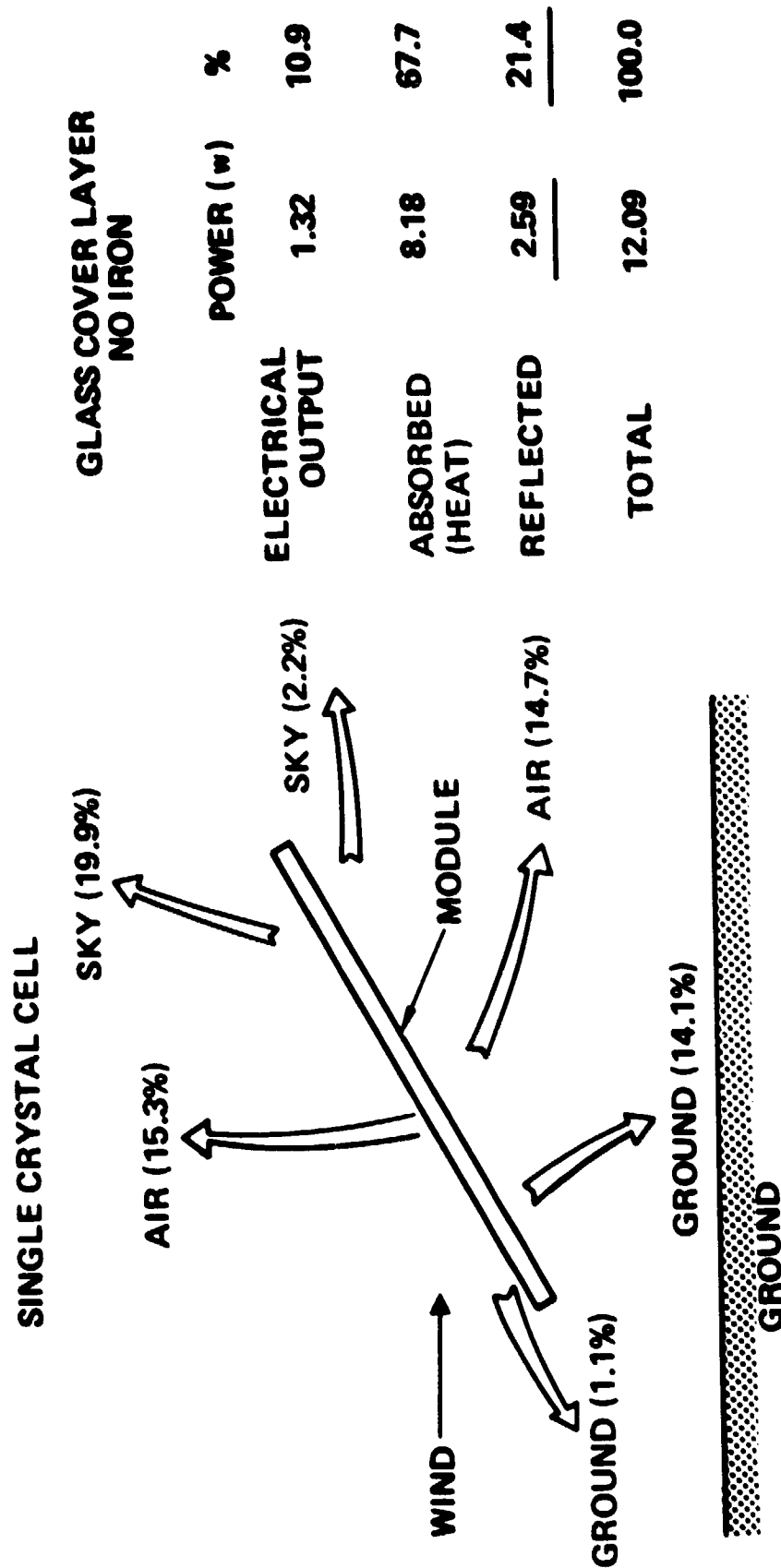


Figure 6-4. Energy Balance for Glass Superstrate Module with Single Crystal Silicon Cells

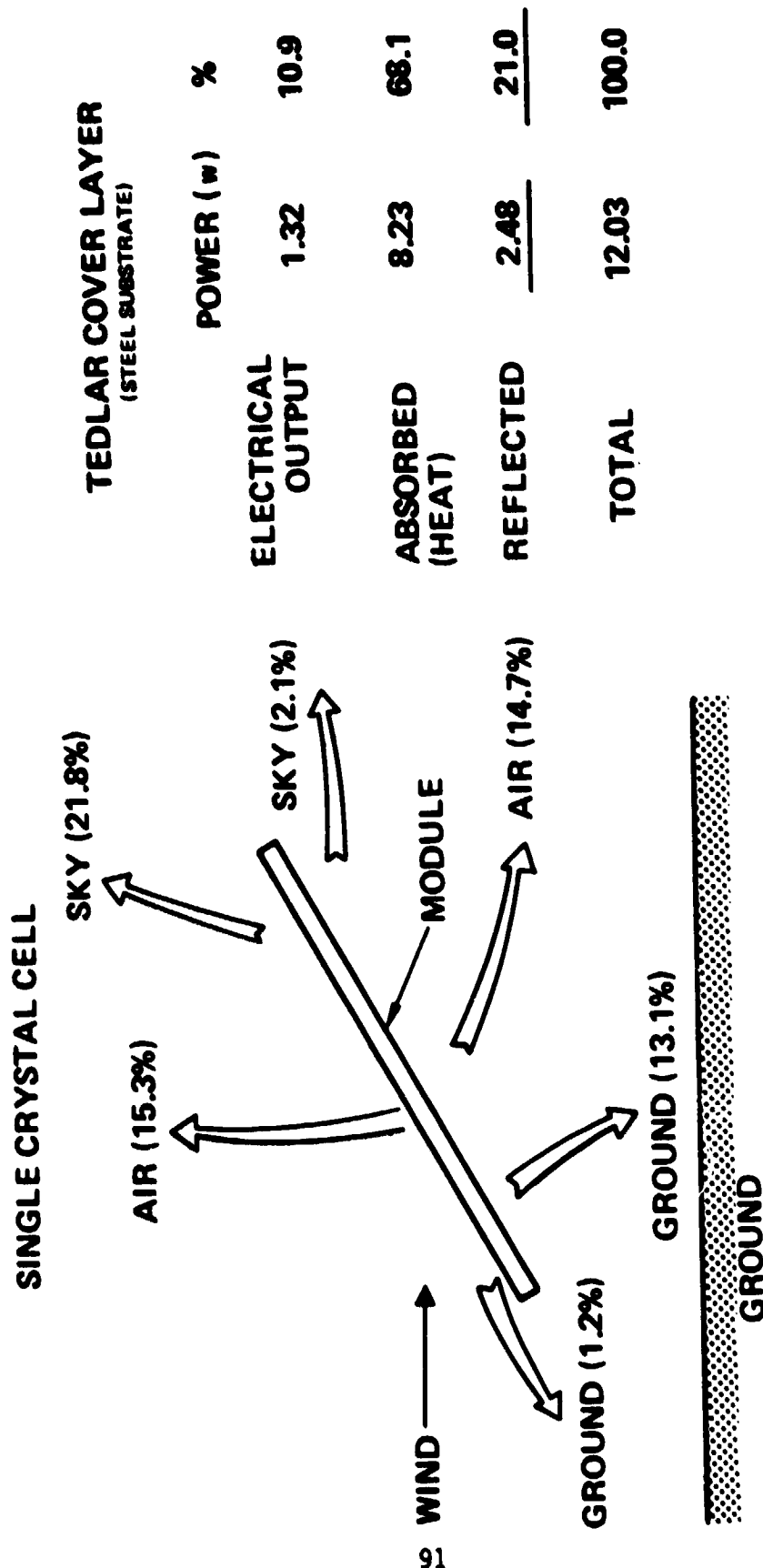


Figure 6-5. Module Energy Balance for Steel Substrate Module with Single-Crystal Silicon Cells

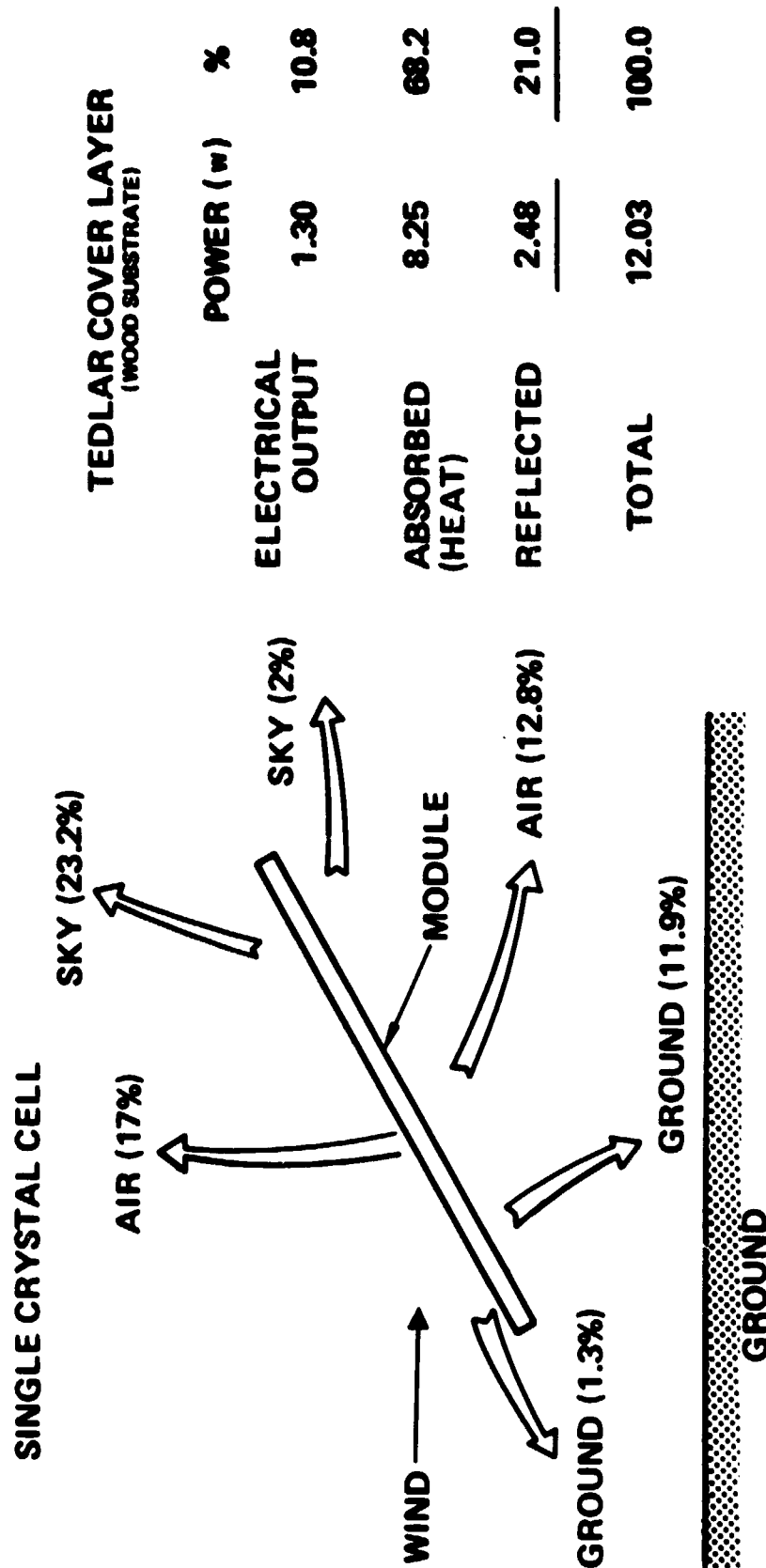


Figure 6-6. Module Energy Balance for Wood-Product Substrate Module with Single-Crystal Silicon Cells



The results for different AR-coating schemes are summarized in Table 6-3 for superstrate modules and in Table 6-6 for substrate modules. In some cases, reference is made to an "optimized" coating. This means that the refractive index of the coating,  $N_A$ , situated between two dielectric layers with indices  $N_1$  and  $N_2$  is given by eq. (5-12). In all cases, the coating thickness was chosen to yield minimum reflectance at 0.6 micron.

For a superstrate module, an optimized AR coating on the air side of the cover glass yields a .03-watt (~2.3 percent) improvement in cell electrical output when compared to the same module with no AR coating. Coating both sides of the glass yields a slightly lower improvement in performance.

TABLE 6-6. Thermal/Optical Performance of Substrate Modules with Texturized and/or AR-Coated Silicon Cells

Substrate Material	Cell Surface Treatment	Calculated Results*	
		Cell Temp, °C	Power, w
Wood	None	51.0	1.30
Wood	AR coating, opt. for cell/pottant	55.6	1.54
Wood	AR coating, opt. for cell/air	55.0	1.51
Wood	AR coating, $TiO_2$	54.8	1.50
Wood	Texturized cell with $TiO_2$ AR coating	55.8	1.50
Wood	Texturized cell	54.8	1.45
Steel	None	48.4	1.32
Steel	AR coating, opt, for cell/pottant	52.6	1.57
Steel	AR coating, opt, for cell/air	52.1	1.54
Steel	Air coating, $TiO_2$	51.9	1.53
Steel	Texturized cell with $TiO_2$ AR coating	52.7	1.53
Steel	Texturized cell	51.8	1.48
* Front Cover: Tedlar, 3-mil thick Pottant: EVA/Craneglas, 10-mil thick Substrate: Steel (unribbed, 200-mil thick), wood (ribbed, 125-mil thick) Back Cover: White-pigmented EVA ( $\epsilon_s=0.89$ ), 10-mil thick			

Three coating schemes for the cell surface were investigated. In the first scheme, an optimized coating at the cell-pottant interface yielded a .24-watt increase in electrical performance over that of a cell with no coating. In the second scheme, titanium dioxide is the coating material; this resulted in a .2-watt increase in electrical power. Electrical output can be increased by .15-watts (i.e. by 11 percent) by using texturized cells. Several cases were investigated for different combinations of AR-coatings on the cell and glass surfaces. As expected, the best combination (for non-texturized cells) is an optimized coating on the cell surface and an optimized coating on the air side of the glass. The calculated results clearly show that AR coating or texturizing the cell surface significantly improves module electrical output.

Similar trends for AR-coated cells in substrate modules are shown in Table 6-6. The maximum improvement is achieved for an optimized AR coating at the cell/pottant interface.

Thermal/optical performance of glass superstrate, ribbed wood substrate, and unribbed steel substrate modules using different pottants is shown in Table 6-7. The pottants studied are EVA, EVA/Craneglas, PVC plastisol and polyurethane. From the information in Table A-5, the absorption coefficients for these pottants can be ranked in the following order: a (polyurethane) < a (EVA) < a (EVA/Craneglas) < a (PVC Plastisol). With this ranking of pottants, it is expected that the cell temperature and power output would be greatest for polyurethane and least for PVC plastisol. This, indeed, is the trend shown in Table 6-7. Since PVC plastisol has a natural yellow tinge, it is concluded that yellowing or discoloration of the pottant due to weathering leads to a marked decrease in power output from a photovoltaic module.

## 6.6 SENSITIVITY STUDIES

As mentioned earlier in Section 6.5.3, the cell temperature is relatively insensitive to pottant thickness and thermal conductivity. On the other hand, the cell temperature decreases significantly with increasing backside emissivity. The sensitivities of cell temperature to pottant thermal resistance and module backside emissivity are discussed in greater detail in this section.

Table 6-7. Thermal/Optical Performance of Superstrate and Substrate Modules using Different Potants and Single Crystal Silicon Cells.

Module Type	Lead-Bearing Number		Potant		Front Cover			Back Cover			Calculated Results(2)		
	Material	Thickness, mil	Material	Thickness, mil	Material	Thickness, mil	Efficiency	Material	Thickness, mil	Efficiency	Temp, °C	Power Generation	Cell Output Power, W
Superstrate	Re-iron glass	125	EVA	10	Re-iron glass	125	0.8	Al foil/white Mylar	.5	.92	53.9	49.4	1.33
Superstrate	Re-iron glass	125	EVA/CS	10	Re-iron glass	125	0.8	Al foil/white Mylar	.5	.92	54.1	49.5	1.32
Superstrate	Re-iron glass	125	PVC plastic	10	Re-iron glass	125	0.8	Al foil/white Mylar	.5	.92	53.6	49.2	1.26
Superstrate	Re-iron glass	125	Polycarbonate	10	Re-iron glass	125	0.8	Al foil/white Mylar	.5	.92	54.5	49.9	1.35
Substrate	Etched and p.(1)	125	EVA	10	Tedlar	3	0.89	White EVA	10	.89	56.7	50.9	1.31
Substrate	Etched and p.	125	EVA/CS	10	Tedlar	3	0.89	White EVA	10	.89	55.8	51.0	1.30
Substrate	Etched and p.	125	PVC plastic	10	Tedlar	3	0.89	White EVA	10	.89	56.2	50.7	1.24
Substrate	Etched and p.	125	Polycarbonate	10	Tedlar	3	0.89	White EVA	10	.89	56.3	51.5	1.33
Substrate	Etched and p. (1)	200	EVA	10	Tedlar	3	0.89	White EVA	10	.89	52.7	48.3	1.33
Substrate	Etched and p. (1)	200	EVA/CS	10	Tedlar	3	0.89	White EVA	10	.89	52.9	48.4	1.32
Substrate	Etched and p. (1)	200	PVC plastic	10	Tedlar	3	0.89	White EVA	10	.89	52.4	48.1	1.26
Substrate	Etched and p. (1)	200	Polycarbonate	10	Tedlar	3	0.89	White EVA	10	.89	53.3	48.8	1.26

(1) Effs on used-product substrate modules are 0.4 in. thick x 2.0 in. high and spaced 8 in. apart

(2) Operational environment

T<sub>air</sub> = 20°C

T<sub>sky</sub> = -5.2°C

T<sub>ground</sub> = 20°C

Ground emissivity = 0.9

Tilt angle = 37°

Insulation = Air Mass 1.5 (normal incidence at 37° tilt)

As mentioned in Section 6.5, the module backside emissivity exerts a significant influence on cell temperature. This is to be expected, because 14 percent to 18 percent of the solar energy absorbed by a module is radiated to the environment off the backside when the backside emissivity is 0.92. Radiation off the front side of the module accounts for about 18 percent to 24 percent of the solar energy absorbed by the module. Decreasing the backside emissivity increases the thermal resistance to radiative heat transfer from the module (see Figure 6-1) and thus leads to higher cell temperatures for the same amount of absorbed solar energy. This behavior is shown graphically in Figure 6-7. Thus, a backside emissivity greater than 0.85 is recommended for module design.

It was also mentioned that cell temperature is relatively insensitive to changes in pottant thickness and thermal conductivity. This trend is shown in Figure 6-8, where the cell temperature is plotted against the conductive thermal resistance between cell and module back surface for several values of conductive thermal resistance between cell and module front surface. The emissivity of both front and back surfaces is 0.9. For the module designs discussed in Section 6.5, the frontside thermal resistance varied from about  $9^{\circ}\text{C cm}^2/\text{watt}$  to about  $45^{\circ}\text{C cm}^2/\text{watt}$ , and the backside thermal resistances ranged from  $4^{\circ}\text{C cm}^2/\text{watt}$ , to about  $170^{\circ}\text{C cm}^2/\text{watt}$ . This range of thermal resistances is indicated by the cross-hatched region in Figure 6-8. For glass superstrate modules, the frontside thermal resistance is significantly higher than the backside thermal resistance; thus these modules fall in the lower left portion of the cross-hatched region of Figure 6-8. For steel substrate modules, frontside and backside thermal resistances are approximately equal; therefore, these modules fall in the middle section of the cross-hatched region. The frontside thermal resistance is less than the backside thermal resistance of wood substrate modules; hence these modules fall in the upper right portion of the cross-hatched region. As seen in Figure 6-8, a ten-fold increase in frontside conductive resistance leads to about a  $3^{\circ}\text{C}$  rise in cell temperature while a ten-fold increase in backside conductive resistance leads to about a  $2.5^{\circ}\text{C}$  rise in cell temperature. Thus, the cell temperature level is determined primarily by the thermal resistance between the module surfaces and the external thermal environment.

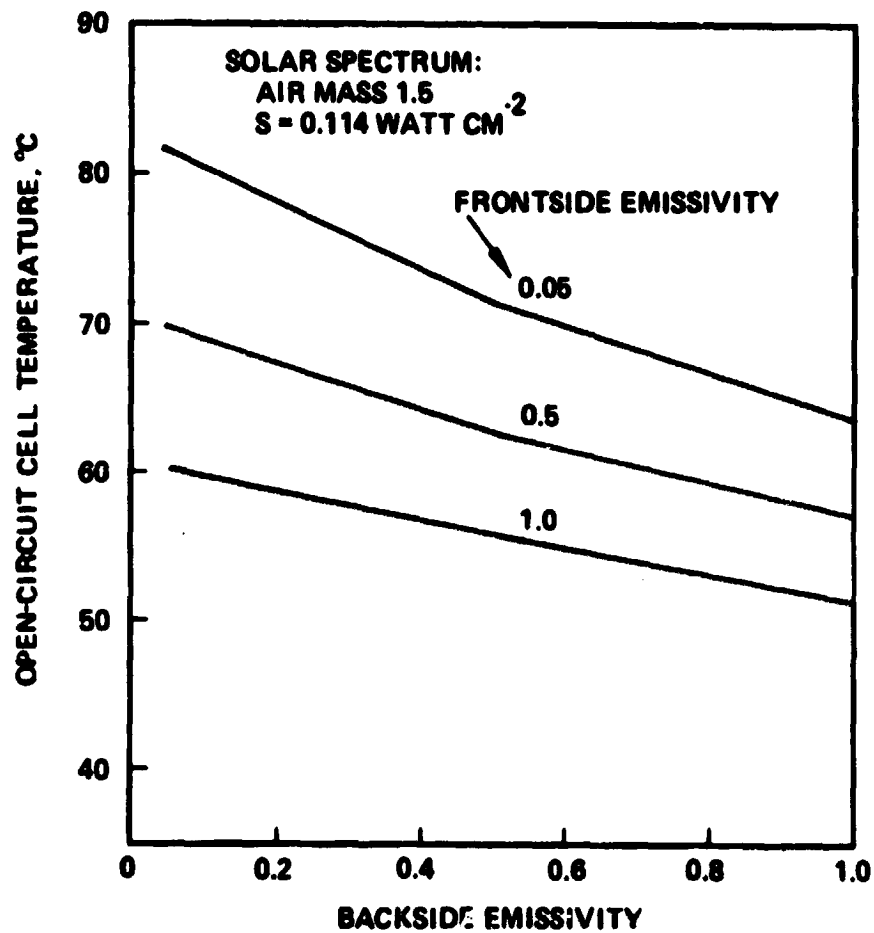


Figure 6-7. Open-Circuit Cell Temperature versus Backside Emissivity for a Glass Superstrate Module

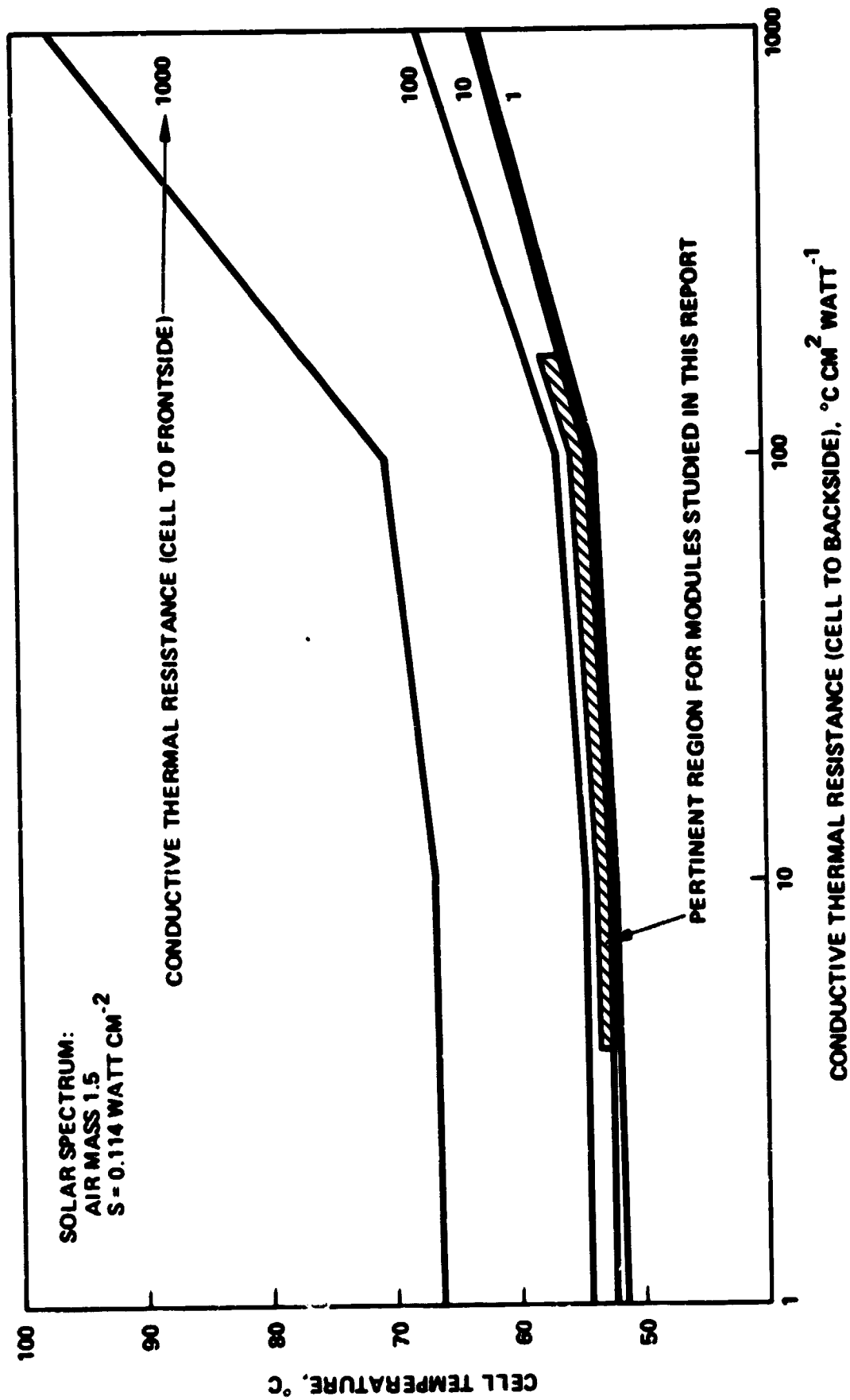


Figure 6-8. Open-Circuit Cell Temperature versus Thermal Resistance (Cell-to-Backside) for a Glass Superstrate Module

## 6.7 CONCLUSIONS

The results of the analysis in this section indicate that the following items are of significance in module thermal/optical design:

- Cell temperature and electrical power output are relatively insensitive to the thermal resistance of the module encapsulation system.
- The emissivities of the front and back surfaces of a module should be greater than 0.85.
- An AR coating is most effective on the cell surface. It is not necessary to match the refractive index of the coating for the pottant/cell interface; a refractive index matched for an air/cell interface will do.
- An AR coating on the exterior surface of a glass superstrate module increases the electrical power output from the module. An AR coating on both sides of the glass degrades this improvement somewhat.
- Yellowing or discoloration of the pottant leads to a reduction in electrical power output from the module.

## 7.0 TECHNOLOGY VOIDS

### 7.1 INFLUENCE OF POTTANT MODULUS AND THICKNESS ON SOLAR CELL STRESS

To guarantee an adequate margin of safety against cell breakage, cell stress must be predictable for expected loading conditions.

Unfortunately, due to the complexity of the layered module construction, structural analyses to determine solar cell stress can be costly and time consuming. This is especially true for analyses to determine the solar cell stress due to normal pressure loads and the sensitivity of this stress to pottant modulus and thickness. The analysis must account for the transverse shear flexibility and thickness stretch provided by the pottant. The problem is further complicated by the fact that module deflection due to pressure loading is large compared to the module thickness; this necessitates the use of large deflection theory in order to avoid excessively conservative design.

In the analysis described in Section 3, a relatively simple approach was used to investigate the sensitivity of cell stress to pottant modulus and thickness. This analysis utilized a two-dimensional finite-element model, wherein one-half of a cell and the additional layers through the thickness of the module were modeled in detail. The model accounted for the shear flexibility and thickness stretch provided by the pottant. It was assumed that small deflection theory was valid in the localized area of each cell. Enforced displacements were applied to the load-bearing layer and the resulting ratio of strain in the cell to strain in the load-bearing layer was determined for various pottant moduli and thicknesses. Utilizing the strain ratio for a given configuration, solar cell stress was then determined for a given maximum design stress in the load-bearing layer.

The accuracy of the analysis can be improved by extending the model to three dimensions. However, computing costs will increase with increased model



complexity. Also, large deflection theory must be considered if the model incorporates many cells. Computing costs for large deflection analyses can be extremely high. These factors must be weighed against the benefits of improved accuracy and increased understanding of the behavior of the encapsulated solar cell.

## 7.2 ALLOWABLE FATIGUE STRENGTH FOR SILICON

The solar cells are subjected to cyclical fatigue loads due to fluctuating wind velocity and daily temperature excursions. Unfortunately, available data for the fracture strength of silicon [3] pertain only to static loading conditions. Since cell breakage is a critical consideration in module design, the allowable fatigue strength for silicon should be determined. Optimum module design cannot be achieved unless the allowable strengths of the constituent elements are accurately known.

In the present analysis, allowable fatigue strengths for silicon solar cells were estimated from fatigue strength data for annealed glass panels [14]. Since glass and silicon are both brittle materials, it was assumed that they both would exhibit similar behavior under fatigue loading. Fatigue strength "knockdown" factors of 0.5 for thermal loading and 0.8 for wind loading were developed. The allowable fatigue strength for each loading condition was determined by multiplying the allowable static strength by the appropriate knockdown factor.

## 7.3 EFFECTS OF HUMIDITY ON MODULE DESIGN

As mentioned in Sections 3 and 4, water absorption in the different polymer layers of a photovoltaic module will exert a strong influence on module lifetime and performance. The presence of moisture leads to polymer swelling and to changes in values of physical properties (i.e., dielectric constant, thermal conductivity, etc.) of polymers as well. In most cases, values of thermal, structural, optical, and electrical properties of polymers as a function of water content are not available in the literature.

Determination of the amount and distribution of water absorbed in a photovoltaic module as a function of humidity is a relatively straightforward analytical task. A method for using conventional thermal analyzer programs for this task is described in reference 6. A method for the direct measurement of moisture concentration in polymers and composites is described in reference 18. However, a number of additional physical properties such as diffusion coefficients and distribution coefficients, both of which are temperature dependent, are required. At present, these properties are not available for the material systems currently under consideration and cannot be made available in the allowed time frame for this program.

#### 7.4 DATA BASE FOR MATERIAL ELECTRICAL PROPERTIES

As shown in Table A-3, there is a great deal of uncertainty in the values of electrical properties to be used in the design of adequate electrical isolation for photovoltaic modules. The property values shown in this table were taken from several literature sources which also indicated that electrical properties of organic materials are strongly influenced by temperature, water content, frequency, and material thickness. Since the provision of adequate electrical isolation must also account for material flaws, such as bubbles and cracks, it is necessary to establish a data base in which the uncertainties in the electrical properties are substantially reduced and the effects of temperature, water content, frequency, and thickness on these properties are better understood.

#### 7.5 EFFECT OF OFF-NORMAL SOLAR INCIDENCE ON THERMAL/OPTICAL PERFORMANCE

The results presented in Section 6 are for the sunline perpendicular to the module surface. This condition occurs only once during the day for a short time each year.

Realistic economic calculations require the realistic calculation of the cumulative electric power generation of a module over a one-year period (assuming there is no degradation in module performance due to weathering). Thus the calculations in Chapter 6 should be extended to include off-normal incidence of the sunline.

The theoretical framework for accomplishing this task has been outlined in Section 5.2.3. However, the reflectivity of each material as a function of incidence angle is required for the calculations. These reflectivities are not available at the present time. An initial approach to this problem would be to use the relations developed in Section 5.2.3 and a constant reflectivity. The extinction coefficient would be taken as that used in the present work, but the path length for sunlight passing through the materials would be greater for off-normal incidence.

#### 7.6 EFFECT OF DIFFUSE SUNLIGHT ON THERMAL/OPTICAL PERFORMANCE

The solar radiation reaching the Earth's surface is part specular and part diffuse. In Section 6, cell temperature and module power output were calculated by assuming that the incident solar flux is entirely specular. As shown in Appendix C, a large percentage of the incident solar flux is diffuse, and in addition, the diffuse component is nonisotropic. Brandemuehl and Beckman [2] have outlined a method for computing the transmittance of incident diffuse radiation through a transparent flat plate. However, the reflectivities and transmissivities of the material interfaces must be known as a function of incidence angle. This data is not presently available in the literature. In addition, the analyses in references 19 and 27 must be expanded to cover multilayer systems such as those encountered in photovoltaic modules.

#### 7.7 EFFECT OF ARRAY PERFORATIONS ON COOLING EFFECTIVENESS

This report treats individual modules which are densely packed with solar cells. The use of module perforations (slots) to provide airflow into what would otherwise be dead air regions behind the modules should improve module thermal performance by introducing cool, fresh air to these regions. The perforation size, aspect ratio, cell packing density (and thus, the module power output) should be considered to improve air circulation and lower cell temperatures. If fins are required for structural integrity, the influence of these fins on air circulation patterns must also be considered.

## 7.8 EFFECT OF NEIGHBORING MODULES IN ARRAY FIELD ON THERMAL/OPTICAL PERFORMANCE

In Section 6, an individual module was treated with no thermal interaction with other modules. Both radiative and convective heat transfer mechanisms are affected by the presence of other modules. While placing identical modules within view of one another can reduce radiative losses from a module to the sky and ground, proper array spacing can minimize this loss in radiative cooling while promoting air circulation in the array field. The criteria for array spacing need to be determined.

## REFERENCES

1. Brady, G.S. and H.R. Clauser, Materials Handbook, 11th ed., McGraw-Hill, 1977, p. 616.
2. Brandemuehl, M.H. and W.A. Beckman, "Transmission of Diffuse Radiation Through CPC and Flat-Plate Collector Glazings," Solar Energy, 24, 511 (1980).
3. Chen, C.P., "Low-Cost Solar Array Project: Fracture Strength of Silicon Solar Cells," JPL Report 5101-137, 15 October 1979.
4. Cuddihy, E.F., "Low-Cost Solar Array Project: Encapsulation Material Trends Relative to 1986 Cost Goals," JPL Report 5101-61, 13 April 1978.
5. Cuddihy, E.F., B. Baum, and P. Willis, "Low-Cost Encapsulation Materials for Terrestrial Solar Cell Modules," Solar Energy, 22, 389 (1979).
6. Haines, J.R., "Application of a Numerical Thermal Analyzer to Three-Dimensional Moisture Absorption Analyses," AIAA Paper No. 80-0215, presented at 18th AIAA Aerospace Sciences Meeting, Pasadena, California, 14-16 January 1980.
7. Halliday, David and Robert Resnik, Physics, Parts I and II, New York, John Wiley & Sons, 1966, pp. 741-763.
8. Jones, R.M., Mechanics of Composite Materials, New York, McGraw-Hill, 1975.
9. LSA Engineering Area, "Low-Cost Solar Array Project: Photovoltaic Module Design, Qualification and Testing Specification," JPL Report 5101-65, 24 March 1978.
10. LSA Engineering Area, "Low-Cost Solar Array Project: Block IV Solar Cell Module Design and Test Specification for Residential Applications," JPL Report 5101-83, 1 November 1978.
11. Mahoney, B.P. and J.M. Kallis, "Efficiency of Solar Cells in Selected Spectral Bands," IDC No. 704220/136, Hughes Aircraft Company, Culver City, California, 1978.
12. Mark, J.G. and C.H. Volk, "Low-Cost Solar Array Project: The Zero-Depth Concentrator Phenomenon," JPL Report 5101-136, 6 August 1979.
13. Mon, Gordon R., "Electrical Isolation Design Considerations," JPL/LSA Module Durability and Life Testing Workshop, 23 September 1980.

14. Moore, D.M., "Low-Cost Solar Array Project: Proposed Method for Determining the Thickness of Glass in Solar Collector Panels," JPL Report 5101-148, 1 March 1980.
15. MSC/NASTRAN User's Manual, The MacNeil-Schwendler Corporation, Pasadena, California, May 1979.
16. Rauschenback, Hans S., Solar Cell Array Design Handbook, Van Nostrand Reinhold Co., New York, 1980.
17. Roark, Raymond J. and Warren C. Young, Formulas for Stress and Strain, 5th ed., McGraw-Hill, New York, 1975, p. 386.
18. Ryan, L.E. and R.W. Vaughan, "Analyses of Moisture in Polymers and Composites," NASA CR-159745 (Contract NAS 3-20406), 11 January 1980.
19. Siegel, Robert, "Net Radiation Method for Transmission Through Partially Transparent Plates," Solar Energy, 15, 273 (1973).
20. Smith, W.J., Modern Optical Engineering, McGraw-Hill, New York, 1966, p. 167.
21. Sparrow, E.M. and K.K. Tien, "Forced Convection Heat Transfer at an Inclined and Yawed Square Plate-Application to Solar Collectors," Trans. ASME (J. Heat Transfer), 99, 507 (1977).
22. Sparrow, E.M., J.W. Ramsey, and E.A. Mass, "Effect of Finite Width on Heat Transfer and Fluid Flow about an Inclined Rectangular Plate," Trans. ASME (J. Heat Transfer), 101, 199 (1979).
23. Steinberg, Dave S., Cooling Techniques for Electronic Equipment, John Wiley & Sons, New York, 1980, p. 136.
24. Stultz, J.W. and L.C. Wen, "Low-Cost Silicon Solar Array Project: Thermal Performance Testing and Analysis of Photovoltaic Modules in Natural Sunlight," JPL Report 5101-31, 29 July 1977.
25. Stultz, J.W., "Low-Cost Solar Array Project: Thermal and Other Tests of Photovoltaic Modules Performed in Natural Sunlight," JPL Report 5101-76, 31 July 1978.
26. Thekaekara, M.P., "Data on Incident Solar Energy," The Energy Crises and Energy from the Sun, Institute of Environmental Sciences, Mount Prospect, Illinois, 1974.
27. Wijesundera, N.E., "A Net Radiation Method for the Transmittance and Absorptivity of a Series of Parallel Regions," Solar Energy, 17, 75 (1975).

**APPENDIX A**

**MATERIAL PROPERTIES**

## APPENDIX A: MATERIAL PROPERTIES

### A.1 INTRODUCTION

Material properties used in the analyses described previously in this report are tabulated in this appendix. Structural properties are discussed in Section A.2. Electrical properties are discussed in Section A.3. Optical properties are discussed in Section A-4, and thermal properties are discussed in Section A-5.

### A.2 STRUCTURAL PROPERTIES

#### A.2.1 Glass Breakage Stress

Breakage stresses for annealed and tempered glass were determined from design curves contained in reference 14. The following factors were considered:

- Plate size
- Duration of load
- Moisture content

Glass fails in tension at stress concentrations at the edges of surface flaws. The breakage stress decreases as plate size increases, because a large plate has more surface flaws than a smaller plate; this increase in the number of flaws increases the probability of failure. It is also known that glass can eventually fail under a long-duration load even though the glass could sustain the same load for a short period of time. Finally, experiments have shown that the relatively small amount of moisture normally present in air is sufficient to greatly reduce the strength of glass relative to levels attained in a dry vacuum.



Figures A-1 and A-2 (from reference 14) show reduction factors for load duration and plate area, respectively. Figure A-3, also from reference 14, presents the recommended design values for breakage strength as a function of probability of failure. These recommended design values apply to a 1 meter square plate simply supported along the edges and subjected to a uniform normal pressure load of one-minute duration. The design curves implicitly reflect the effect of moisture.

Glass breakage stresses were determined for both thermal loading and normal pressure (wind) loading. Consistent with current thinking at JPL, the pressure load was assumed to act for a total of 15 minutes, and the thermal cycling load was assumed to act for a total of seven years or about a third of the design lifetime of LSA modules. The breakage values were derived for a 1.2 m x 1.2 m plate, which is the LSA module baseline, and a one percent failure probability. The allowable breakage stresses for glass plates and the reduction factors for plate area and load duration are listed in Table A-1.

#### A.2.2 Silicon Solar Cell Breakage Stress

The silicon solar cell allowable stresses reflect fatigue knockdown factors for thermal cycling and wind pressure loading. Since available fracture strength data [3] pertain to static loading conditions, the fatigue limits were derived under the assumption that silicon behaves like annealed glass. Fatigue strength knockdown factors of 0.5 for thermal cycling and 0.8 for wind loading were derived from Figure 9 of reference 14 for an assumed static strength of 10,000 psi.

#### A.2.3 Porcelain/Steel Allowable Stress

Several suppliers and manufacturers of porcelain-coated steel were contacted, but they were unable to provide the required design data. Therefore, the allowable design stress for porcelainized steel was derived from simple strength of materials considerations assuming an allowable strength of 5000 psi for porcelain [1].

#### A.2.4 Other Structural Properties

Other structural properties such as thermal expansion coefficient, modulus of elasticity, and allowable stress are listed in Table A-2 for different materials used in module construction.

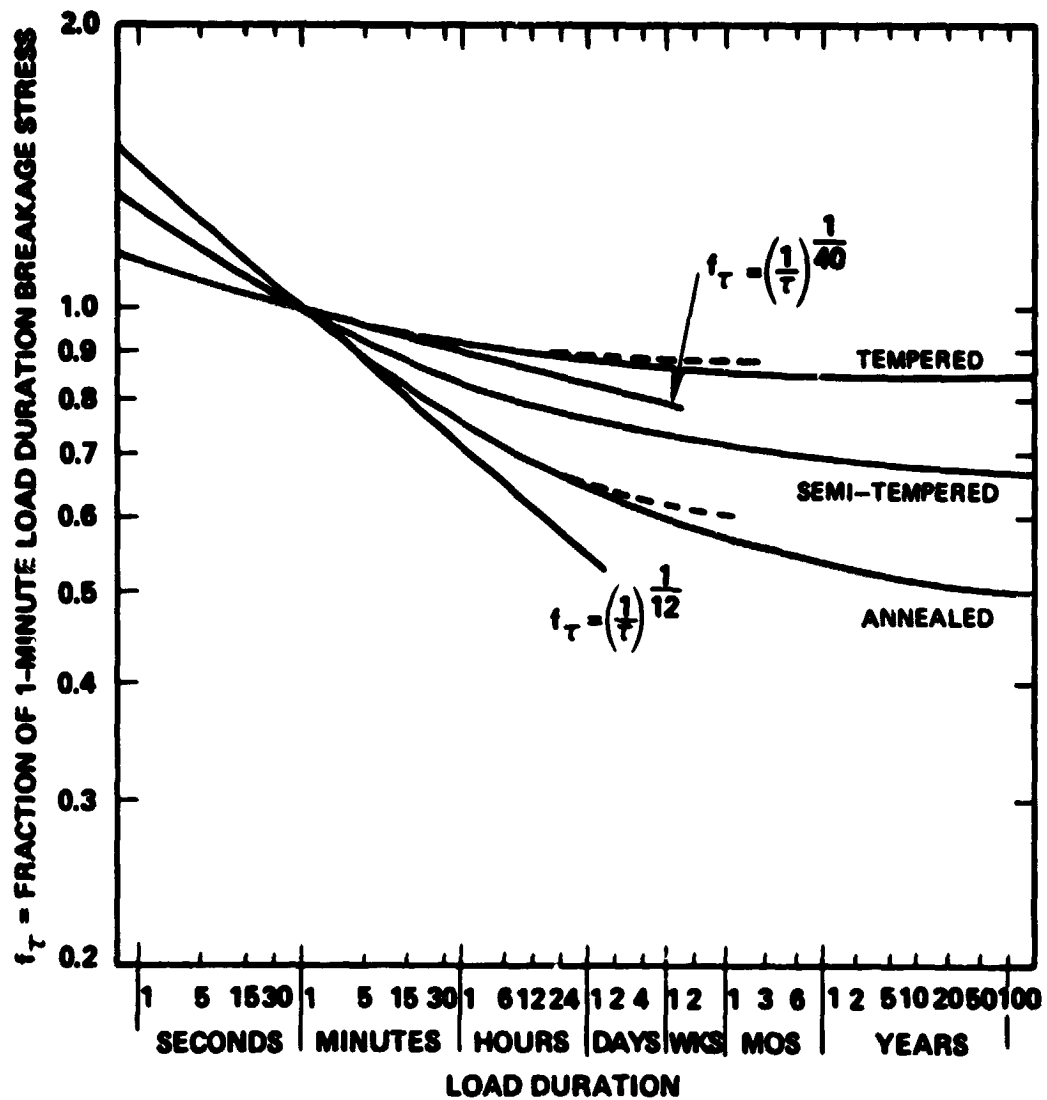


Figure A-1. Fraction of 1-Minute Load Duration Breakage Stress for Glass versus Load Duration

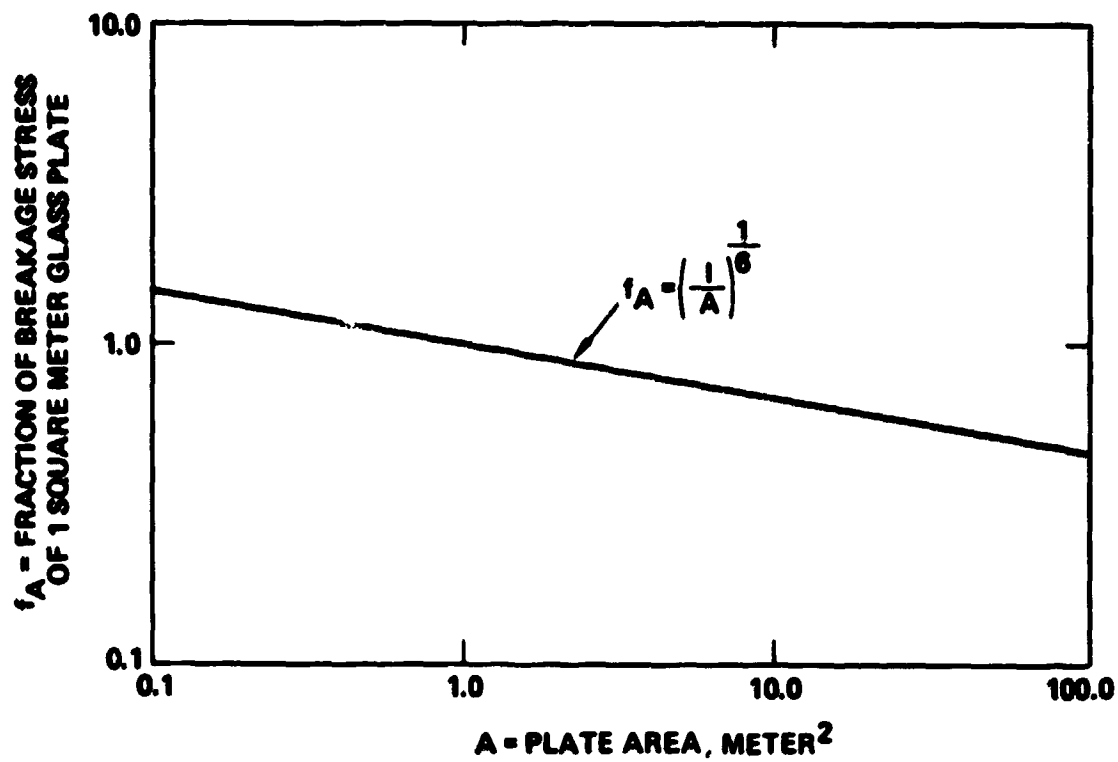


Figure A-2. Fraction of Breakage Strength of 1.0 Meter Square Glass Plates versus Plate Area

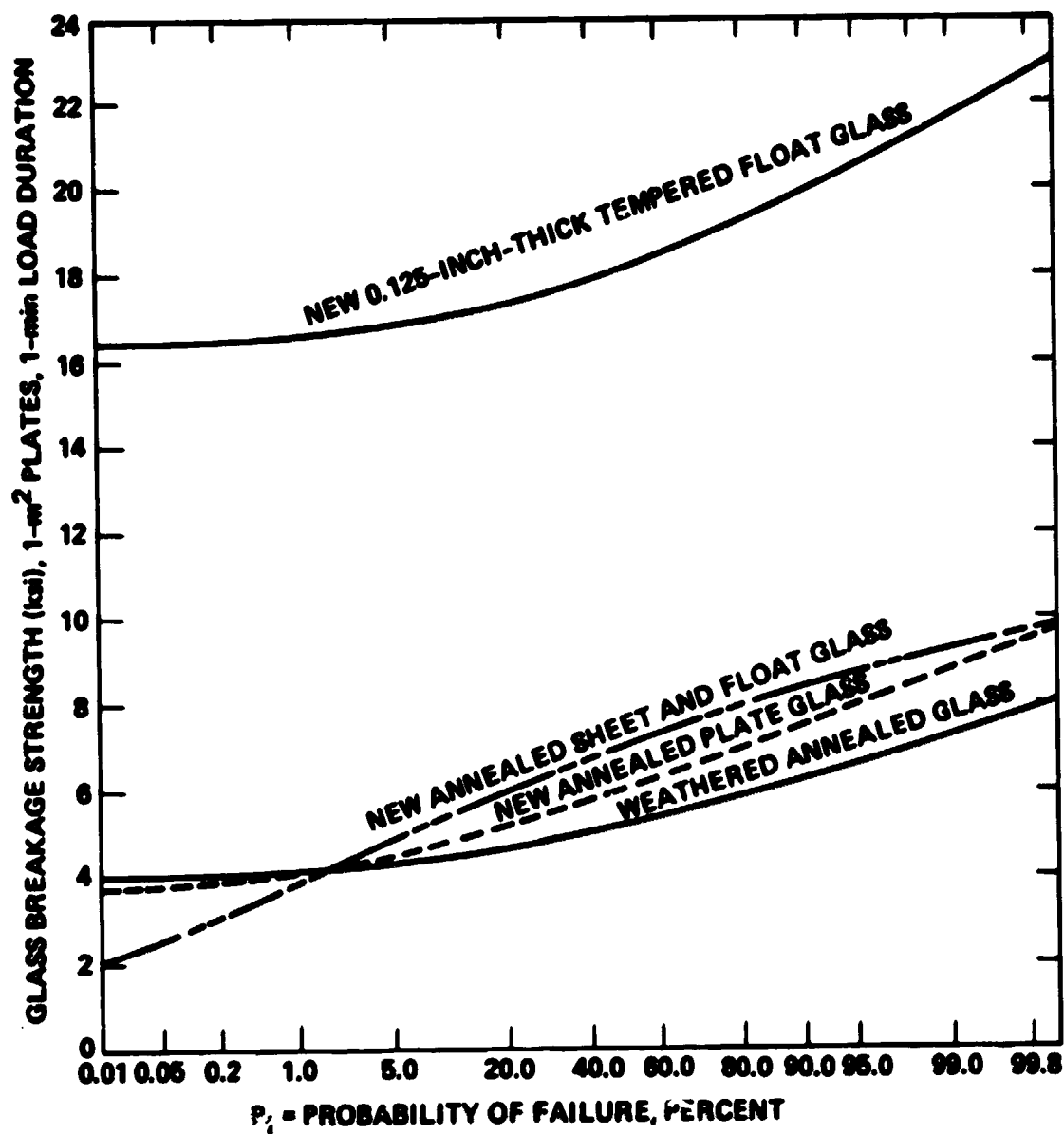


Figure A-3. Recommended Design Values for Breakage Strength versus Probability of Failure for a One Meter Square, Simply-Supported, Glass Plate Subjected to a Uniform Normal Pressure Load of 1-Minute Duration

**TABLE A-1. Allowable Breakage Stresses for 1.2 Meter x 1.2 Meter Glass Plates Subject to Wind Pressure and Thermal Cyclic Loading**

Glass Type	Area Reduction Factor, $f_A$	Load Duration Reduction Factor, $f_T$		$\sigma_A, \text{psi}^{(1)}$	Allowable Breakage Stress, $\text{psi}^{(2)}$	
		Wind	Thermal		Wind	Thermal
Annealed	0.936	.83	.52	4200	3662	2044
Tempered	0.936	.94	.85	16500	13590	13127

(1) Allowable breakage stress for 1 meter<sup>2</sup>, 1 minute load duration, and 1 percent failure probability

(2) Allowable breakage stress =  $f_A f_T \sigma_A$

**TABLE A-2. Structural Properties of Silicon Solar Cells, Glass, Wood Product, and Steel**

Material	E, psi	$\alpha, (\text{in}^\circ\text{C})^{-1}$	Allowable Stress, psi
Glass			
Tempered	$10 \times 10^6$	$9.2 \times 10^{-6}$	13000
Annealed	$10 \times 10^6$	$9.2 \times 10^{-6}$	2000-3600
Wood Product	$0.8-1.2 \times 10^6$	$7.2 \times 10^{-6}$	2500
Silicon Cell	$17 \times 10^6$	$4.4 \times 10^{-6}$	5000-6000
Porcelainized Steel	$30 \times 10^6$	$10.8 \times 10^{-6}$	5000
Uncoated Steel	$30 \times 10^6$	$10.8 \times 10^{-6}$	28000
Aluminum (6061-T4)	$10 \times 10^6$	$23.4 \times 10^{-6}$	16000

### A.3 ELECTRICAL PROPERTIES

Electrical properties such as resistivity, dielectric constant, and dielectric strength are listed in Table A-3. The wide ranges in property values are due to the fact that these properties are strongly dependent on moisture content, frequency, temperature, and thickness. These influencing factors were usually not specified in the literature sources from which the data were obtained.

### A.4 OPTICAL PROPERTIES

#### A.4.1 Reflectance and Transmittance

Spectral variation of reflectance and transmittance for different front cover materials and for some candidate pottants are contained in this section. Relevant data for front cover materials, such as Korad and Tedlar, are presented in Figures A-4 thru A-6. Data for glass are presented in Figures A-7 through A-9. Data for pottants are presented for EVA (Figure A-10), EVA/Craneglas (Figure A-11), white-pigmented EVA (Figure A-12), polyurethane (Figure A-13), and PVC plastisol (Figure A-14). All data, except that for Tedlar, were measured at Hughes; data for Tedlar was provided by E.I. DuPont and Company.

#### A.4.2 Absorption Coefficient.

The optical equations of Appendix E can be used to interpret experimentally determined values of total transmittance and reflectance of thin films. These quantities differ from the reflectivity, the transmittance (T), and the transmissivity ( $\tau$ ) defined in Section 5. Applying eq. (E-10) to a single layer with the media on either side being the same, the following expression can be derived:

$$\frac{q_4^+}{q_1^-} = \frac{T (1-\rho)^2}{(1-\rho^2 T^2)} \quad (A-1)$$

The expression on the left hand side is the total transmittance shown in Figures A-4 thru A-14. As shown in eq. (E-11), the reflectivity,  $\rho$ , and total

TABLE A-3. Electrical Properties For Wood Product, Different Pottants, and Organic Cover Films

Material	Dielectric Constant $\gamma$	Dielectric Strength S(volt/mil)	Resistivity $\rho$ (ohm-cm)
Korad	3.5-4.4	2200	$10^{13}$
Tedlar	7.4-9.9	1700-3500	$2 \times 10^{10}$ - $7 \times 10^{14}$
EVA	2.7-3.2	620	$10^9$ - $10^{12}$
EPR	2.2-3.0	500-1000	---
Polyurethane	4.7-9.5	330-700	---
PNBA	2.7-4.5	800	---
PVC Plastisol	4-8	300	$10^{11}$ - $10^{13}$
Wood product	2.1	175	---

reflectance are related to a good approximation by letting the total reflectance equal two times the reflectivity. Values of total transmittance and reflectance versus wavelength can be obtained from Figures A-4 thru A-14. These values in turn can be used in the above quadratic expression to obtain values for the spectral transmittance,  $T$ , of the layer and the absorption coefficient,  $a$ , of the material.

Absorption coefficients for a number of front cover and pottant materials are presented in Tables A-4 and A-5.

#### A.4.3 Index of Refraction

Indices of refraction for different pottants and front cover materials are listed in Table A-6.

#### A.5 THERMAL PROPERTIES

The thermal conductivities of different module construction elements are listed in Table A-7.

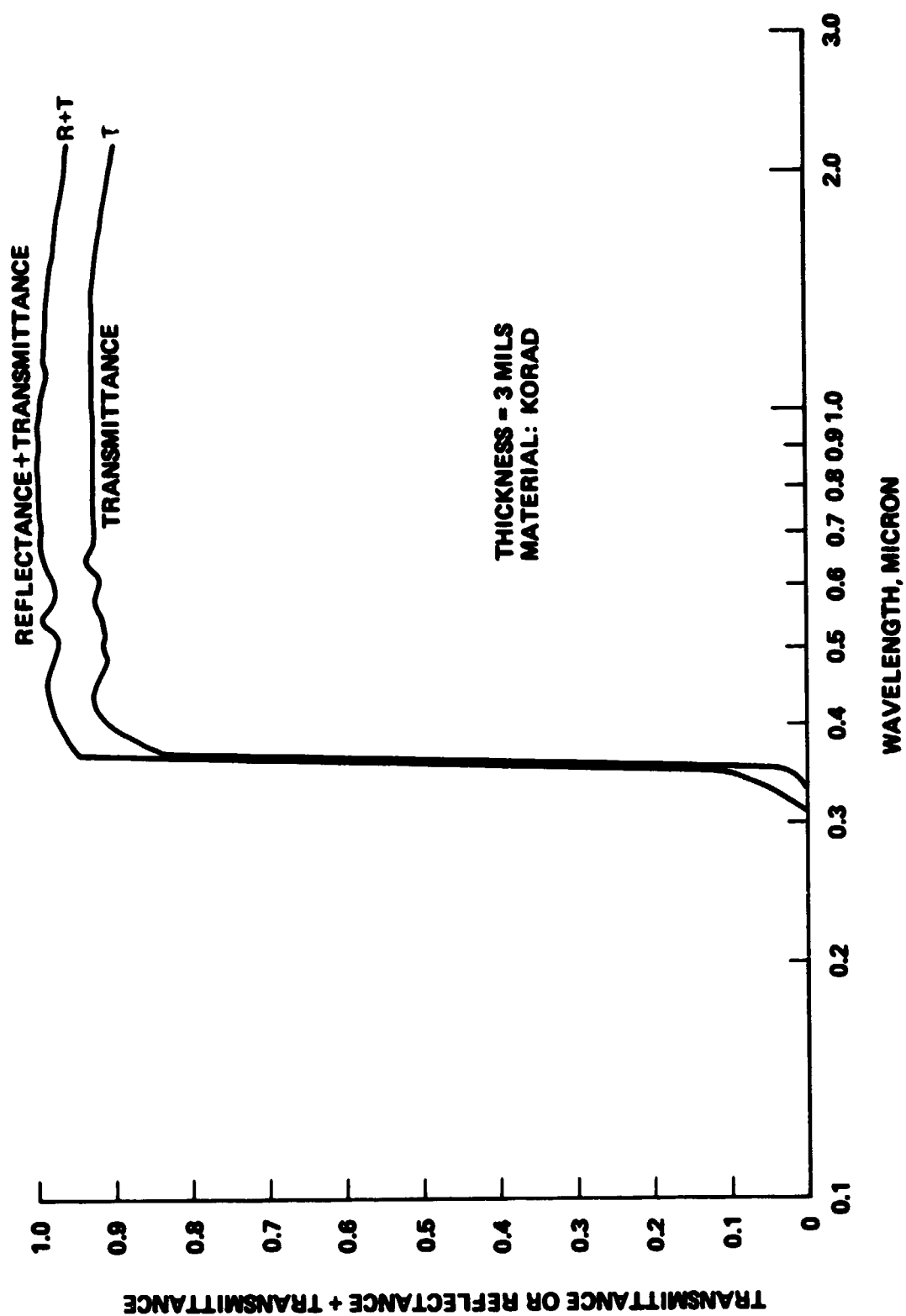


Figure A-4. Transmittance and Reflectance Plus Transmittance versus Wavelength for Korad



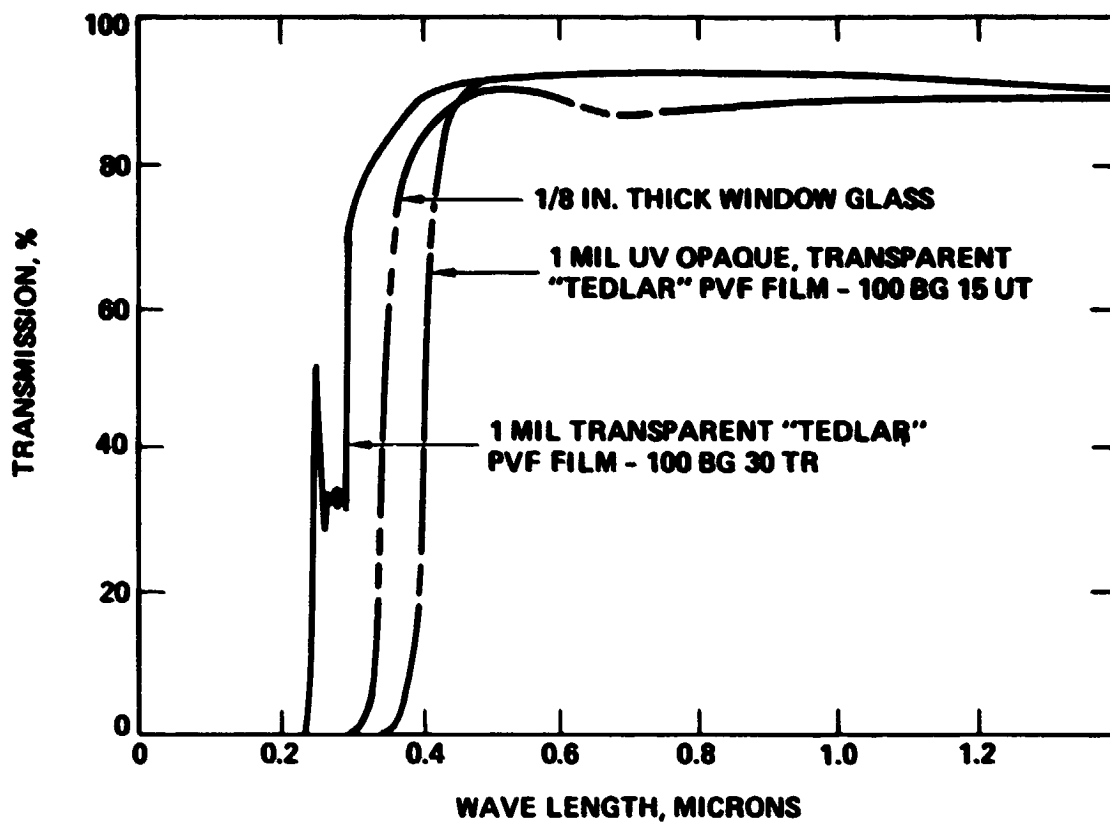


Figure A-5. Transmittance versus Wavelength ( $.2\mu$ - $1.2\mu$ ) for Tedlar

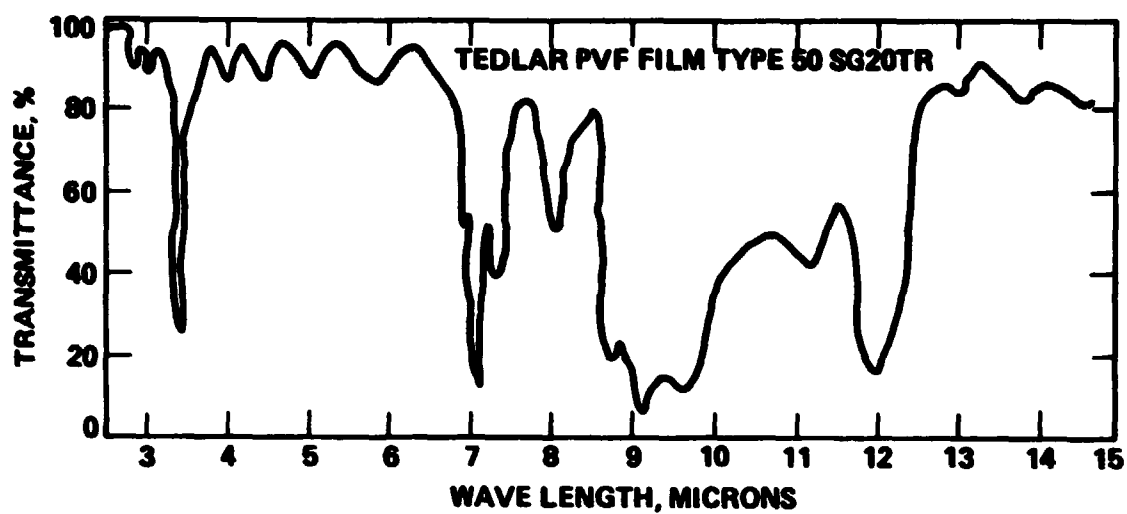


Figure A-6. Transmittance versus Wavelength ( $3\mu$ - $15\mu$ ) for Tedlar

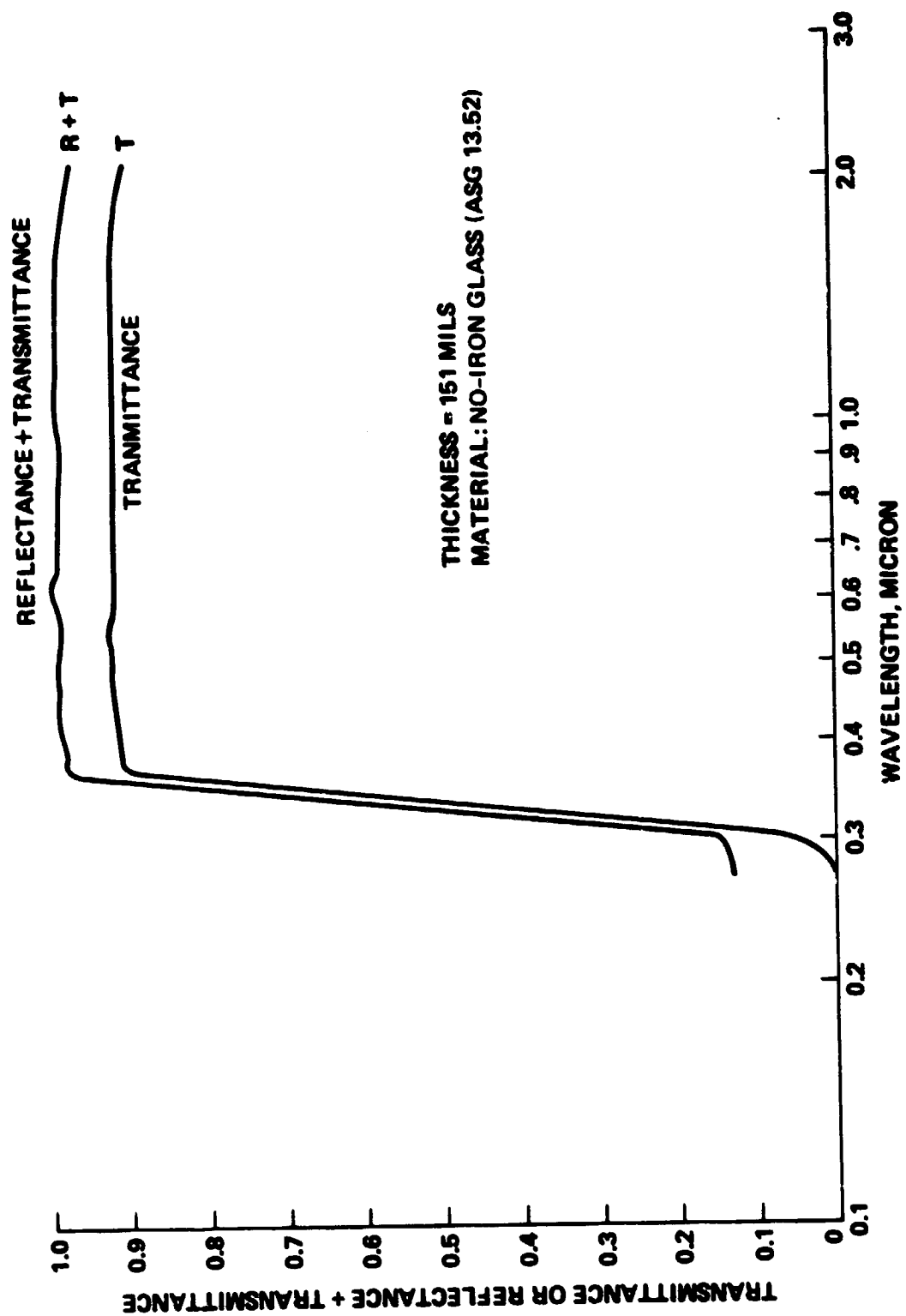


Figure A-7. Transmittance and Transmittance Plus Reflectance versus Wavelength for No-Iron Glass

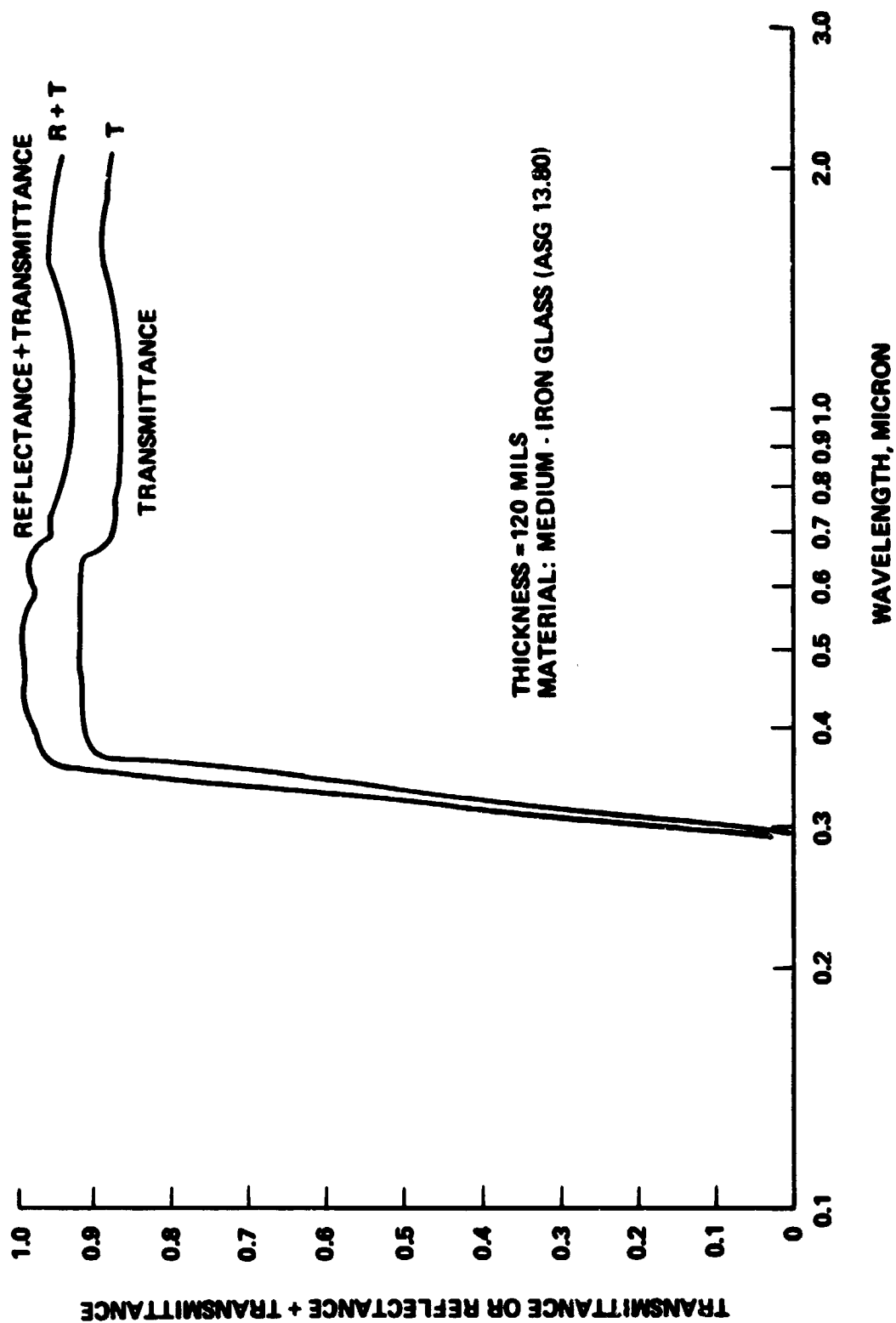


Figure A-8. Transmittance and Transmittance Plus Reflectance versus Wavelength for Medium-Iron Glass

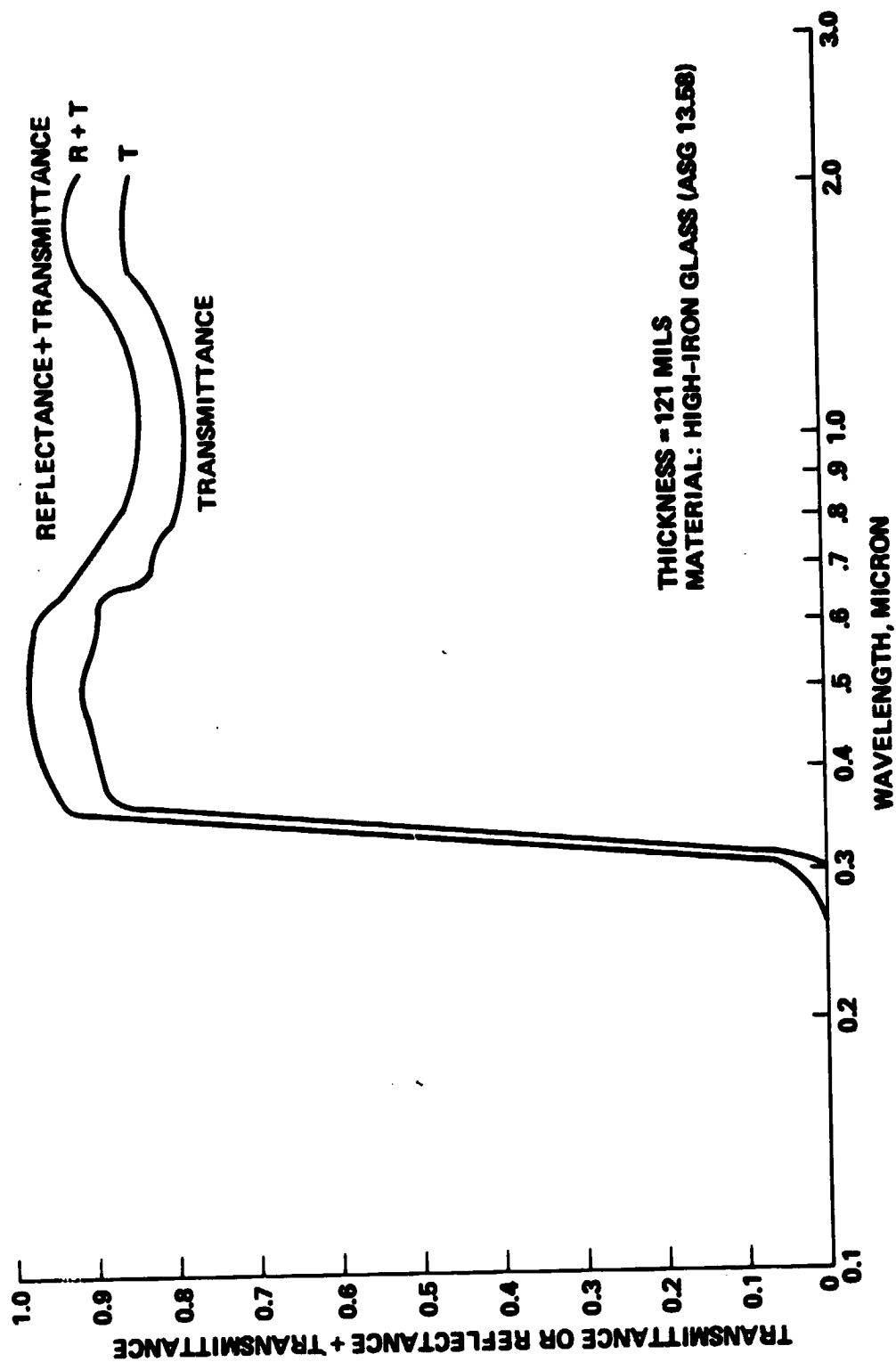


Figure A-9. Transmittance and Transmittance Plus Reflectance versus Wavelength for High-Iron Glass

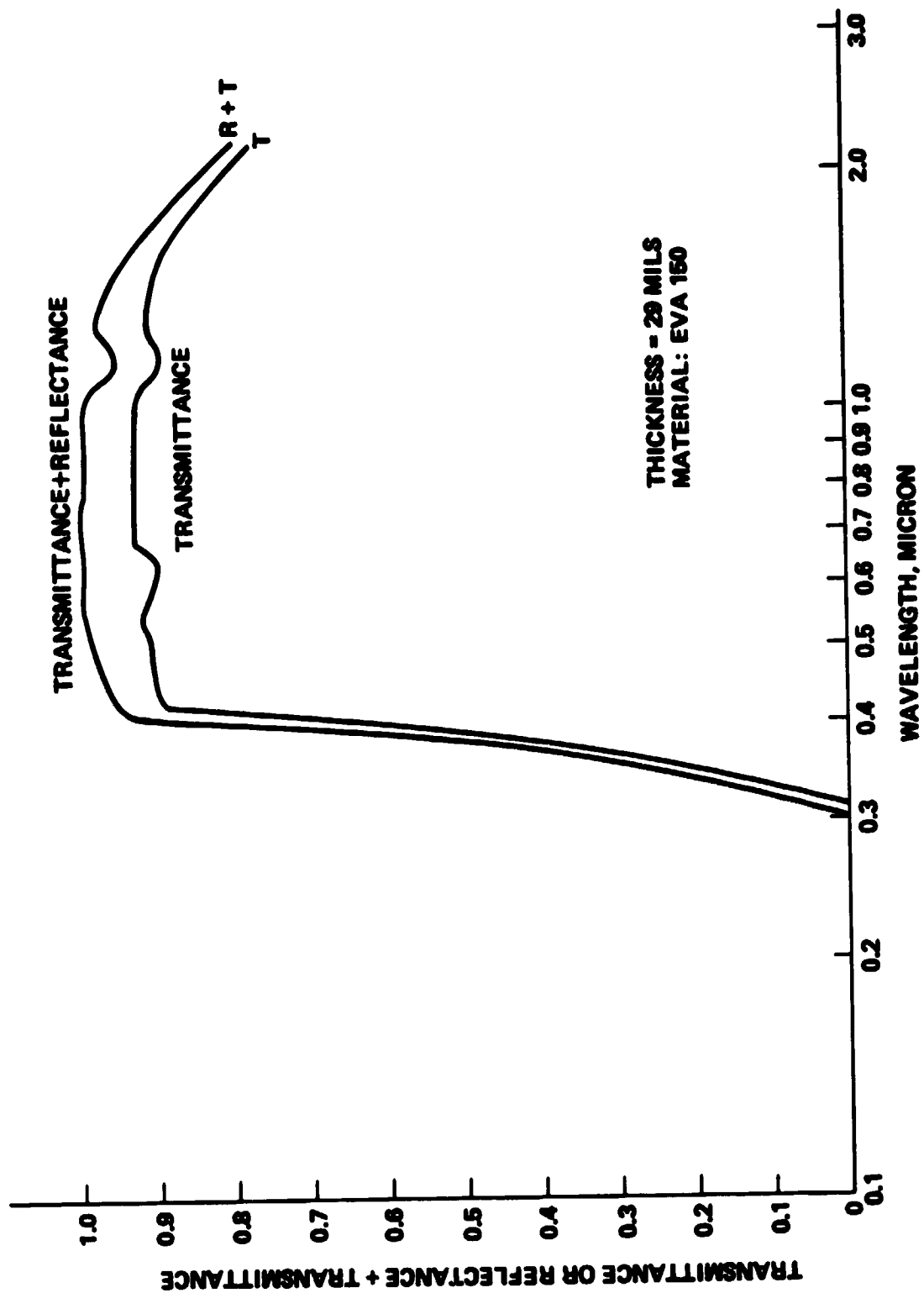


Figure A-10. Transmittance and Transmittance Plus Reflectance versus Wavelength for EVA

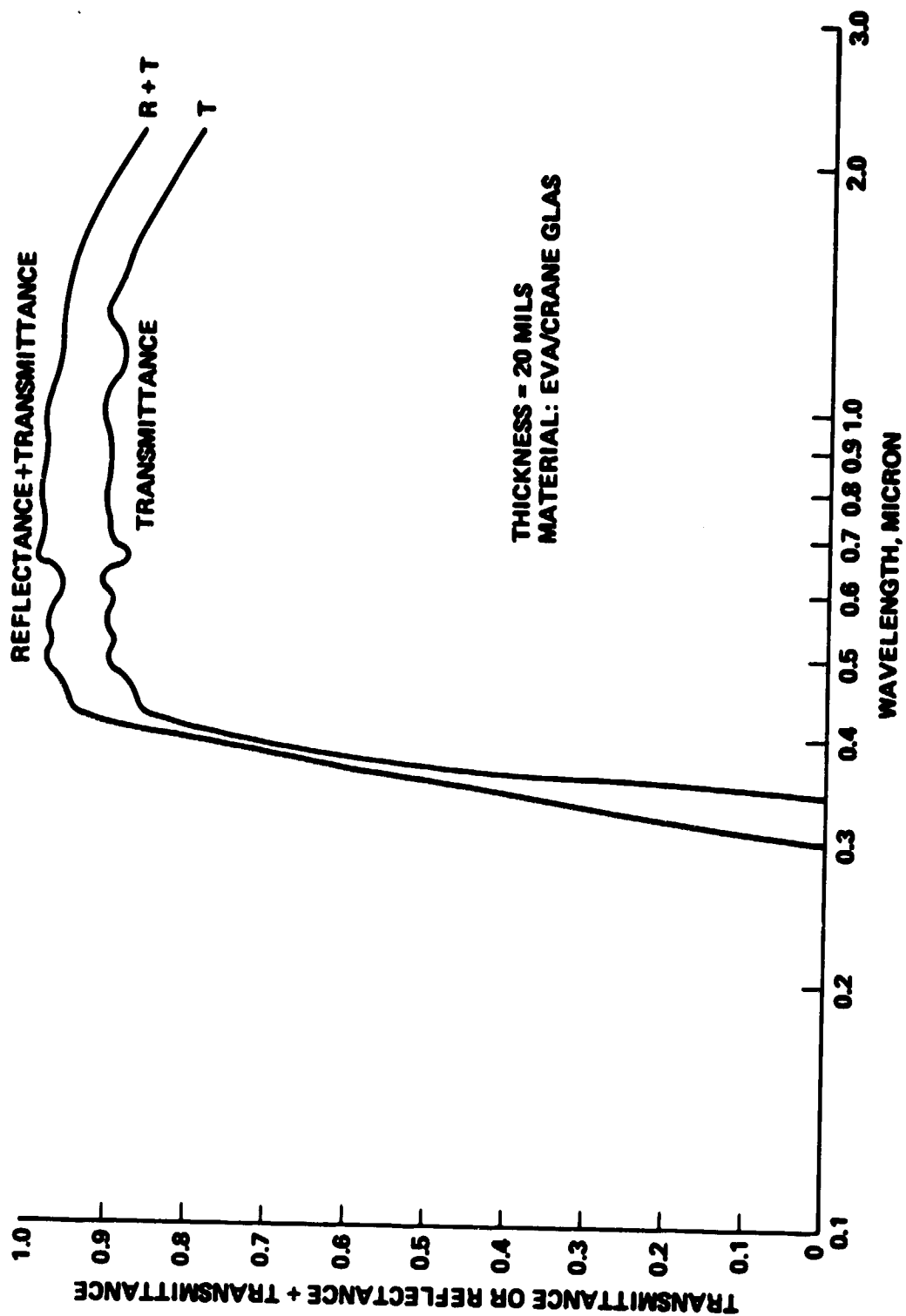


Figure A-11. Transmittance and Transmittance Plus Reflectance versus Wavelength for EVA/Craneglas

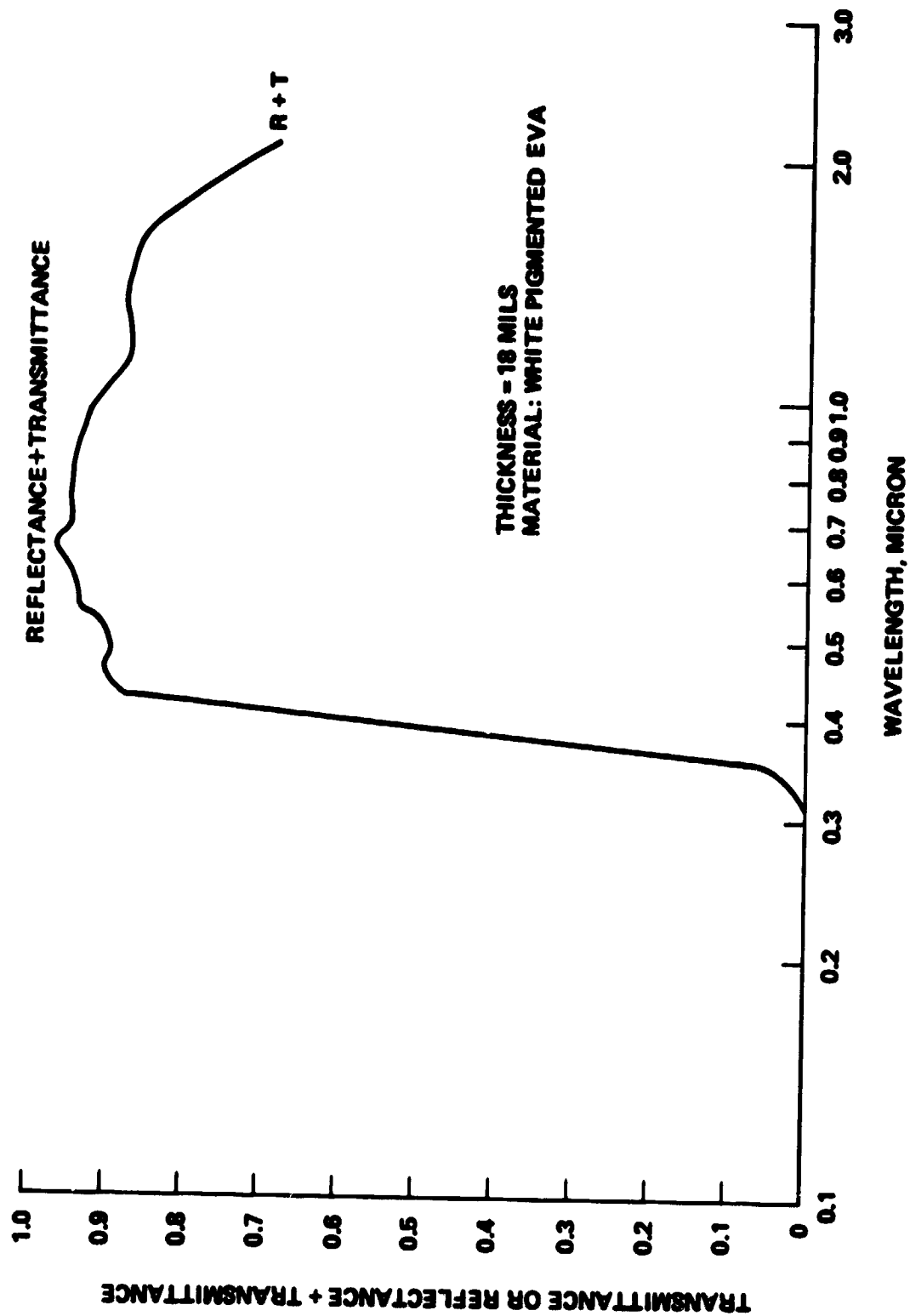


Figure A-12. Transmittance Plus Reflectance versus Wavelength for White-Pigmented EVA



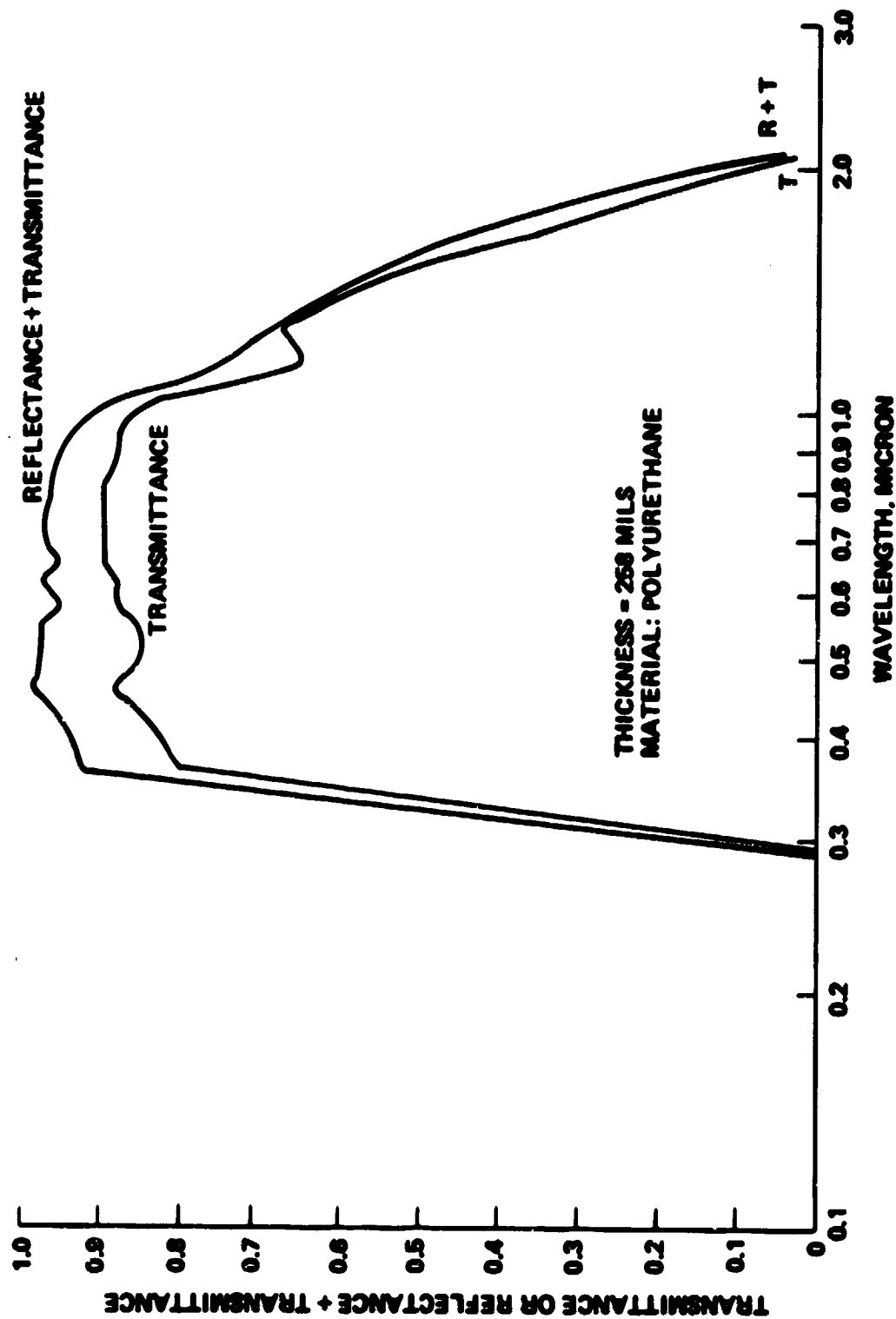


Figure A-13. Transmittance and Transmittance Plus Reflectance versus Wavelength for Polyurethane

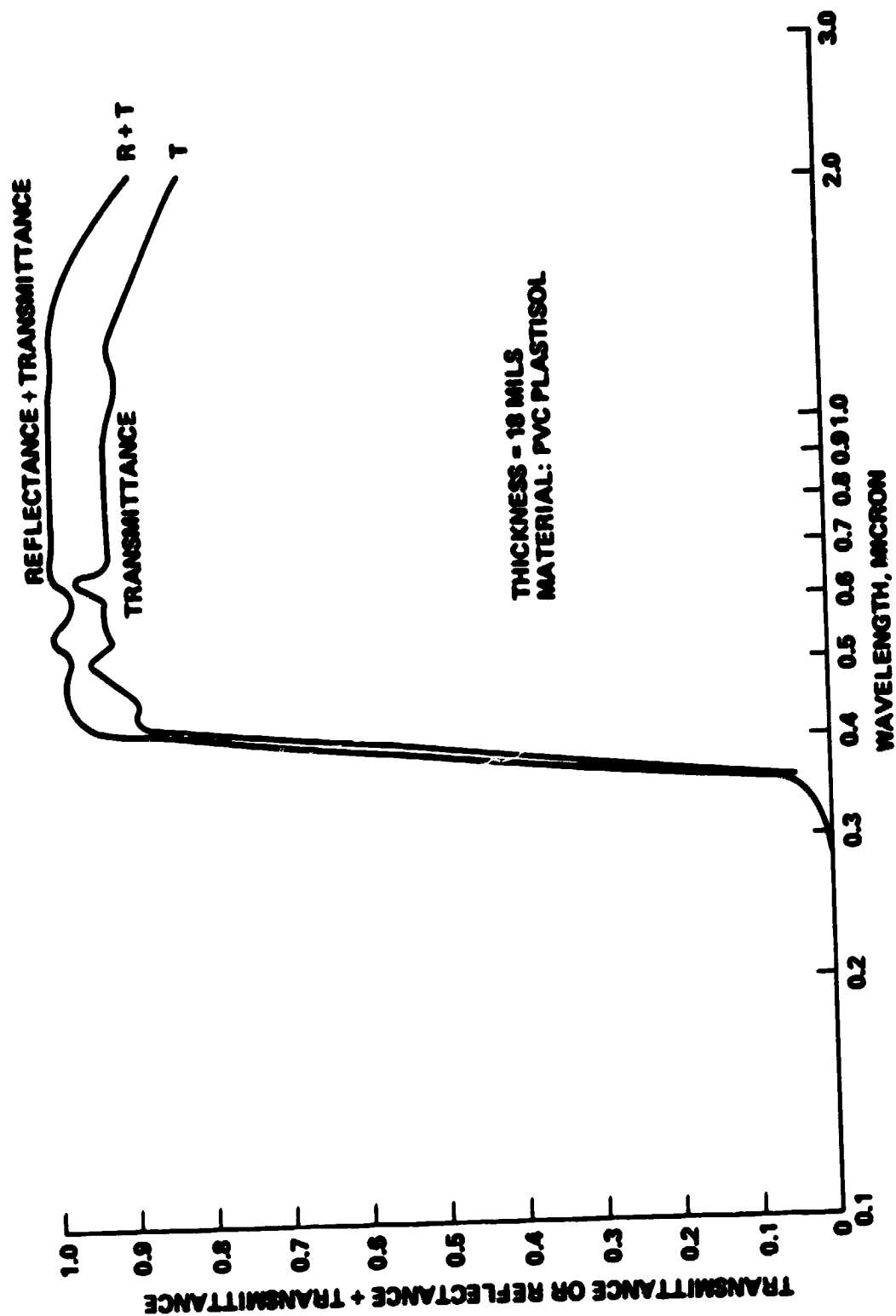


Figure A-14. Transmittance and Transmittance Plus Reflectance versus Wavelength for PVC Plastisol

TABLE A-4. Spectral Absorption Coefficients  
for Glass, Tedlar, and Korad\*

Wavelength, micron	Absorption Coefficient, $\text{cm}^{-1}$				
	Glass No Iron (151 mil)	Glass Med. Iron (120 mil)	Glass High Iron (121 mil)	Tedlar (5 mil)	Korad (3 mil)
.367	.0746	.129	.230	36.3	9.63
.422	.0387	.065	.118	11.7	2.98
.457	.0402	.052	.197	7.4	2.81
.485	.0351	.051	.086	5.2	3.78
.514	.0402	.051	.086	3.1	4.49
.544	.0397	.054	.095	3.1	1.58
.577	.0402	.081	.123	1.0	3.42
.613	.245	.078	.138	1.0	3.15
.649	.0354	.072	.256	1.0	1.60
.688	.0354	.152	.325	1.0	1.57
.731	.0354	.171	.397	1.0	1.44
.778	.0350	.202	.481	1.0	1.45
.829	.0380	.231	.543	1.0	1.46
.882	.0406	.255	.588	3.1	1.46
.967	.0406	.266	.622	3.1	1.45
1.036	.0354	.270	.630	5.2	1.72
1.149	.0354	.265	.614	5.2	1.98
1.273	.0354	.243	.558	7.4	2.10
1.585	.0402	.163	.356	9.5	3.19
2.091	.10	.224	.358	9.5	6.28

\* Data obtained at Hughes Aircraft. Specimen thickness shown in parentheses

TABLE A-5. Spectral Absorption Coefficients for EVA, EVA/Craneglas, PVC Plastisol, and Polyurethane\*

Wavelength, micron	Absorption Coefficient, $\text{cm}^{-1}$			
	EVA (29 mil)	EVA/ Craneglas (20 mil)	PVC Plastisol (18 mil)	Polyurethane (258 mil)
.367	8.659	11.20	38.6	.36
.422	.7	1.33	3.13	.22
.457	.53	.96	2.04	.08
.485	.35	.49	1.53	.12
.514	.32	.55	1.87	.13
.544	.32	.48	.76	.15
.577	.32	.76	1.50	.25
.613	.34	.74	2.05	.12
.649	.33	.18	.59	.19
.688	.15	.29	.63	.14
.731	.15	.33	.69	.13
.778	.18	.28	.69	.15
.829	.18	.33	.69	.18
.882	.19	.33	.69	.21
.967	.18	.36	.63	.30
1.036	.23	.28	.76	.46
1.149	.82	.77	1.06	1.42
1.273	.47	.75	1.00	1.07
1.585	1.12	1.22	2.70	2.93
2.091	3.31	3.02	7.77	13.9

\* Data obtained at Hughes Aircraft. Specimen thickness shown in parentheses

TABLE A-6. Refractive Index for Module Construction Materials\*

Material	Index of Refraction
No-Iron glass (ASG 13.80)	1.57
Medium-Iron glass (ASG 13.52)	1.57
High-Iron glass (ASG 13.58)	1.56
Korad	1.45
Tedlar	1.46
PVC Plastisol	1.31
Polyurethane	1.46
EVA/Craneglas	1.39-1.43
EVA	1.4

\* Properties measured at Hughes Aircraft

TABLE A-7. Thermal Conductivity of Typical Module Construction Materials

Material	Thermal Conductivity, watt (cm <sup>2</sup> C) <sup>-1</sup>
Glass	.01
Tedlar	.00167
Korad	.00167
EVA	.0035
PNBA	.00167
Polyurethane	.0035
PVC Plastisol	.0035
Silicon	.835
Aluminum	2.1
Wood product	.002
Mild steel	.58
Mylar	.00018

**APPENDIX B**  
**NOMENCLATURE**

## B.1 STRUCTURAL ANALYSIS NOMENCLATURE

$E$  = Young's modulus of elasticity, lb/in<sup>2</sup>

$\sigma$  = Normal stress, lb/in<sup>2</sup>

$\epsilon$  = Strain, in/in

$\nu$  = Poisson's ratio

$\alpha$  = Coefficient of thermal expansion, in(in°C)<sup>-1</sup>

$b$  = Width of plate, in

$\delta$  = Deflection of plate normal to surface, in

$t$  = Thickness of plate, in

$D$  = Flexural modulus of plate =  $\frac{Et^3}{12(1-\nu^2)}$

$P$  = Uniform normal pressure load, lb/in<sup>2</sup>

## B.2 ELECTRICAL ANALYSIS NOMENCLATURE

$E$  = Electric field, volt/mil

$E_i$  = Electric field in material layer  $i$ , volt/mil

$i_L$  = Leakage current, amp

$R_i$  = Electrical resistance of material layer  $i$ , ohm

$S_i$  = Dielectric strength of material layer  $i$ , volt/mil

$t_i$  = Thickness of material layer  $i$ , mil

$V_i$  = Electric potential difference across material layer  $i$ , volt

$V_0$  = Electric potential difference across encapsulation system, volt

$\gamma_i$  = Dielectric constant of material layer  $i$

$\beta_i$  = Electric resistivity of material layer  $i$ , ohm-cm

### B.3 THERMAL ANALYSIS NOMENCLATURE

- $A$  = Cross-sectional area for conductive, convective, or radiative heat flow,  $\text{cm}^2$
- $A_c$  = Cell area illuminated by sun,  $\text{cm}^2$
- $F_{s-b}$  = Shape factor for radiation from surface  $s$  to radiation boundary  $b$  ( $b$  = ground, sky)
- $l_{ij}$  = Distance between nodes  $i$  and  $j$  in thermal model,  $\text{cm}$
- $P$  = Electrical power produced by cell, watt
- $Q_1, Q_1'$  = Solar energy absorbed as heat in front cover of module, watt
- $Q_2, Q_2'$  = Solar energy absorbed as heat in pottant between cell and front cover, watt
- $Q_c$  = Solar energy absorbed in cell, watt
- $Q_c'$  = Solar energy absorbed in opaque pottant adjacent to cell, watt
- $R_{s\text{-air}}$  = Thermal resistance to convective heat flow from module surface to air,  $^\circ\text{C}/\text{watt}$
- $R_{s-b}$  = Thermal resistance to radiative heat flow from module to radiation boundary  $b$  ( $b$  = ground, sky),  $^\circ\text{K}^4/\text{watt}$
- $S$  = Solar flux at ground level,  $\text{watt cm}^{-2}$
- $T$  = Temperature,  $^\circ\text{C}$  or  $^\circ\text{K}$
- $V$  = Air velocity, meter/sec
- $\epsilon_s$  = Emissivity of module surface
- $X$  = Angle between module and ground, degree
- $\eta$  = Overall conversion efficiency of cell
- $\sigma$  = Stefan-Boltzman constant =  $5.67 \times 10^{-12}$  watt ( $\text{cm}^2 \text{ } ^\circ\text{K}^4$ )

### B.4 OPTICAL ANALYSIS NOMENCLATURE

- $A_c$  = Cell area illuminated by sun,  $\text{cm}^2$



$a$	= Absorption coefficient, $\text{cm}^{-1}$
$C_\lambda$	= Spectral power conversion efficiency of cell
$C_{\lambda i}$	= Power conversion efficiency of cell averaged over wavelength band $\lambda_i$
$F_{0-\lambda}$	= Percentage of solar irradiation in wavelength band $0-\lambda$
$I_\lambda$	= Spectral solar intensity at ground level, watt $(\text{cm}^2 \text{ micron})^{-1}$
$I_{\lambda i}$	= Average solar irradiation for wavelength band $\lambda_i$ , watt $\text{cm}^{-2}$
$I_{0\lambda}$	= Spectral solar intensity at edge of terrestrial atmosphere, watt $(\text{cm}^2 \text{ micron})^{-1}$
$k$	= Absorption constant for terrestrial atmosphere
$M$	= Number of equal-energy wavelength bands used to represent solar spectrum
$m$	= Air mass ratio
$N_A$	= Refractive index of antireflection coating
$N_1$	= Refractive index of layer 1
$N_2$	= Refractive index of layer 2
$P_\lambda$	= Electric power generated by bare cell at wavelength $\lambda$ , watt
$P$	= Total electric power generated by bare cell, watt
$PE_\lambda$	= Electric power generated by encapsulated cell at wavelength $\lambda$ , watt
$PE$	= Total electric power generated by encapsulated cell, watt
$Q_c$	= Solar radiation absorbed at cell surface, watt
$Q_h$	= Solar radiation absorbed in cell and converted to heat, watt
$Q_i$	= Incident solar radiation, watt
$Q_r$	= Reflected solar radiation, watt
$q^+$	= Radiant energy flux leaving a surface (radiosity), watt $\text{cm}^{-2}$
$q^-$	= Radiant energy flux impinging on a surface (irradiation), watt $\text{cm}^{-2}$

$T_{\lambda}$	= Spectral transmittance of encapsulation system
$T_{\lambda i}$	= Transmittance of encapsulation system averaged over wavelength band $\lambda i$
$T_{eff}$	= Effective transmittance of encapsulation system
$t$	= Thickness of material layer in encapsulation system, cm
$t_A$	= Thickness of AR coating, micron
$\eta$	= Cell efficiency = Electrical power output/(radiant energy absorbed by cell per unit time)
$\eta^*$	= Cell efficiency = Electrical power output/(radiant energy incident on cell surface per unit time)
$\lambda$	= Wavelength, micron
$\theta_1$	= Angle of incidence
$\theta_2$	= Angle of refraction
$\theta_c$	= Critical angle
$\rho$	= Reflectivity of a surface
$\rho_A$	= Reflectivity of an AR coated surface
$\rho_T$	= Reflectivity of texturized cell surface
$\tau$	= Transmissivity of an interface
$\omega$	= Defined in eq. (5.11d)

## APPENDIX C

### SOLAR SPECTRUM FOR AIR MASS 1.5

## APPENDIX C: SOLAR SPECTRUM FOR AIR MASS 1.5

The U.S. Standard Atmosphere Model with a rural aerosol was used to produce the data for this standard.\* This atmospheric model exhibits the following parameters for a vertical path from sea level to the top of the atmosphere:

Precipitable water vapor = 1.42 cm

Total ozone = 0.34 cm

Turbidity (base e) = 0.27

Atmospheric parameters, such as temperature, pressure, aerosol density, air density, and the density of nine molecular species are defined at 33 levels within the atmosphere. These parameters vary exponentially between these 33 levels. The absorption and scattering properties of the aerosol were calculated by means of MIE theory. A bi-model, log-normal, aerosol size distribution with a complex index of refraction that varies with wavelength was used to define the aerosol. The turbidity used corresponds to a sea level meteorological range of 23 km.

The standard data presented here was generated for a solar zenith angle of 48.19 degrees (AM 1.5) and a surface albedo of 0.2. The surface was assumed to have a cosine distribution for reflection or to obey Lambert's Law.

---

\*The information in this Appendix was provided by Dr. Roger Estey of JPL.

TABLE C-1. Solar Spectral Irradiance - Standard Curves for 0.2  
Ground Albedo and a Horizontal Surface

- $\lambda$  = Wavelength, micron
- $D_{\lambda}$  = Direct normal spectral irradiance averaged over  
20  $\text{cm}^{-1}$  centered at  $\lambda$ , watt ( $\text{meter}^2 \text{ micron}$ ) $^{-1}$
- $S_{\lambda}$  = Scattered (diffuse) horizontal spectral irradiance  
averaged over 20  $\text{cm}^{-1}$  centered at  $\lambda$ ,  
watt ( $\text{meter}^2 \text{ micron}$ ) $^{-1}$
- $G_{\lambda}$  = Total (global) horizontal spectral irradiance aver-  
aged over 20  $\text{cm}^{-1}$  centered at  $\lambda$ , watt ( $\text{meter}^2$   
micron) $^{-1}$

Total Solar Energy Flux = 650 watt meter $^{-2}$

$\lambda$	$D_{\lambda}$	$S_{\lambda}$	$G_{\lambda}$	$\lambda$	$D_{\lambda}$	$S_{\lambda}$	$G_{\lambda}$
.3050	3.76	7.83	10.33	.5400	1027.00	336.43	1021.09
.3100	17.65	34.53	46.28	.5500	1006.00	315.62	986.29
.3150	45.66	84.03	114.47	.5700	1006.00	229.27	899.93
.3200	78.88	136.38	188.97	.5900	983.00	212.93	868.26
.3250	123.70	200.51	282.98	.6000	1023.00	226.60	904.60
.3300	162.30	221.23	329.43	.6300	999.50	208.66	874.99
.3350	188.70	241.34	367.14	.6500	999.00	200.52	866.52
.3400	207.80	249.36	387.89	.6700	1008.00	198.21	870.21
.3450	224.80	253.37	403.24	.6900	841.80	159.00	726.86
.3500	246.30	261.67	425.87	.7100	958.80	178.19	817.39
.3600	272.00	303.25	484.58	.7184	718.10	184.79	583.52
.3700	333.50	336.53	558.86	.7218	900.90	135.48	736.08
.3800	345.90	318.31	548.91	.7240	738.50	108.50	600.38
.3900	367.70	309.98	555.11	.7400	921.10	138.38	752.44
.4000	513.60	399.31	741.71	.7525	922.40	138.43	753.36
.4100	670.30	482.96	929.82	.7575	916.60	137.09	748.15
.4200	708.30	474.68	946.88	.7625	513.90	72.26	414.86
.4300	698.90	437.74	903.67	.7675	817.50	119.72	664.72
.4400	807.50	474.33	1012.66	.7800	844.70	130.50	720.30
.4500	933.10	515.44	1137.50	.8000	838.90	121.21	680.47
.4600	995.40	490.94	1154.54	.8157	644.00	71.78	501.11
.4700	1015.00	472.11	1148.77	.8210	799.00	91.88	624.54
.4800	1064.00	467.82	1177.15	.8234	608.30	67.00	472.53
.4900	1029.00	238.82	1114.82	.8251	774.10	88.58	604.64
.5000	1046.00	414.21	1111.54	.8319	724.30	81.66	564.52
.5100	1035.00	389.90	1079.90	.8400	785.50	98.80	613.46
.5200	1027.00	368.86	1053.52	.8600	771.90	87.96	602.56
.5300	1045.00	358.34	1055.00	.8800	743.40	83.99	579.58

TABLE C-1. Solar Spectral Irradiance - Standard Curves for 0.2  
Ground Albedo and a Horizontal Surface (Continued)

$\lambda$	$D_\lambda$	$S_\lambda$	$G_\lambda$	$\lambda$	$D_\lambda$	$S_\lambda$	$G_\lambda$
.9000	499.00	53.02	385.68	1.4770	94.35	3.95	66.85
.9150	565.40	60.09	437.02	1.4970	160.40	7.05	113.98
.9250	609.20	62.45	468.58	1.5200	227.70	10.48	162.28
.9340	150.40	13.73	113.99	1.5390	244.30	11.52	174.38
.9403	483.00	48.19	370.18	1.5580	240.50	11.36	171.69
.9500	268.60	25.35	204.42	1.5780	217.50	10.12	155.12
.9550	280.00	26.44	213.11	1.5920	227.80	9.63	161.49
.9650	476.40	47.10	364.70	1.6100	206.70	8.64	146.43
.9800	559.30	56.66	425.52	1.6300	213.10	8.97	151.04
.9935	628.70	65.25	484.38	1.6460	205.80	8.64	145.84
1.0400	576.50	59.34	443.67	1.6780	193.40	8.08	137.01
1.0700	533.60	54.22	409.95	1.7400	152.20	6.22	107.68
1.1000	364.70	26.56	269.69	1.8000	26.48	.96	18.62
1.1200	97.69	6.57	71.70	1.8600	1.74	.86	1.22
1.1230	59.58	3.95	43.67	1.9200	1.01	.04	.71
1.1319	241.30	17.00	177.86	1.9600	17.86	.64	12.55
1.1351	23.92	1.56	17.51	1.9850	72.70	1.81	50.28
1.1610	285.80	20.32	210.85	2.0050	22.47	.53	15.51
1.1800	392.50	28.87	290.53	2.0350	83.79	2.14	58.00
1.2350	396.00	29.47	293.47	2.0650	54.45	1.36	37.65
1.2900	330.80	23.99	244.52	2.100	80.38	2.08	55.67
1.3200	203.50	14.08	149.74	2.1480	78.12	2.04	54.12
1.3500	27.40	1.08	19.35	2.1980	70.27	1.82	48.67
1.3950	1.36	.05	.96	2.2700	68.36	1.80	47.38
1.4425	49.53	2.00	35.01	2.3600	58.32	1.51	40.39
1.4625	93.13	3.90	65.99	2.4500	23.37	.56	16.14

TABLE C-2. Solar Spectral Irradiance - Standard Curves for 0.2  
Ground Albedo and a 37° Tilted Surface

- $\lambda$  = Wavelength, micron  
 $D_{\lambda}$  = Direct normal spectral irradiance averaged over  
 $20 \text{ cm}^{-1}$  centered at  $\lambda$ , watts (meter<sup>2</sup> micron)<sup>-1</sup>  
 $S_{\lambda}$  = Scattered (diffuse) horizontal spectral irradiance on  
 $37^{\circ}$  tilted surface averaged over  $20 \text{ cm}^{-1}$  centered at  
 $\lambda$ , watt (meter<sup>2</sup> micron)<sup>-1</sup>  
 $G_{\lambda}$  = Total (global) horizontal spectral irradiance on a  $37^{\circ}$   
tilted surface averaged over  $20 \text{ cm}^{-1}$  centered at  $\lambda$ ,  
watt(meter<sup>2</sup> micron)<sup>-1</sup>

Total Solar Energy Flux = 970 watt meter<sup>-2</sup>

$\lambda$	$D_{\lambda}$	$S_{\lambda}$	$G_{\lambda}$	$\lambda$	$D_{\lambda}$	$S_{\lambda}$	$G_{\lambda}$
.3050	3.76	6.78	10.47	.5100	1035.00	625.20	1640.52
.3100	17.64	30.20	47.50	.5200	1027.00	594.80	1602.28
.3150	45.66	74.11	118.90	.5300	1045.00	580.39	1606.12
.3200	78.88	121.15	198.53	.5400	1027.00	548.31	1555.79
.3250	123.70	179.30	300.65	.5500	1006.00	516.95	1503.82
.3300	162.30	242.93	402.14	.5700	1006.00	367.36	1354.23
.3350	188.70	267.11	452.22	.5900	983.00	339.34	1303.65
.3400	207.80	278.15	482.00	.6100	1023.00	357.15	1360.70
.3450	224.80	284.15	505.38	.6300	999.50	334.49	1314.99
.3500	246.30	296.49	538.11	.6500	999.00	321.07	1301.08
.3600	272.00	305.44	572.27	.6700	1008.00	318.03	1306.87
.3700	333.50	341.89	669.05	.6900	851.80	253.83	1089.44
.3800	345.90	326.24	665.56	.7100	958.80	285.23	1225.80
.3900	367.70	320.73	681.44	.7184	718.10	166.46	870.91
.4000	513.60	416.96	920.80	.7218	900.90	216.02	1099.79
.4100	670.30	509.01	1166.57	.7240	738.50	171.80	896.26
.4200	708.30	505.12	1199.95	.7400	921.10	220.83	1124.42
.4300	698.90	470.15	1155.76	.7525	922.40	220.99	1125.85
.4400	807.50	514.17	1306.32	.7575	916.60	218.85	1118.02
.4500	933.10	564.00	1479.36	.7625	513.90	114.98	619.11
.4600	996.20	762.65	1739.91	.7675	817.50	191.00	992.96
.4700	1015.00	737.84	1733.54	.7800	884.70	208.33	1076.21
.4800	1064.00	736.26	1780.03	.8000	838.90	193.43	1016.38
.4900	1029.00	679.23	1688.67	.8167	644.00	125.47	757.23
.5000	1046.00	660.23	1686.34	.8210	799.00	164.75	948.56

TABLE C-2. Solar Spectral Irradiance - Standard Curves for 0.2  
Ground Albedo and a 37° Tilted Surface (Continued)

$\lambda$	$D_\lambda$	$S_\lambda$	$G_\lambda$	$\lambda$	$D_\lambda$	$S_\lambda$	$G_\lambda$
.8234	608.30	116.35	713.09	1.3950	1.36	.10	1.44
.8251	774.10	158.49	917.87	1.4425	49.53	3.83	52.42
.8319	724.30	144.90	855.43	1.4625	93.13	7.43	98.79
.8400	785.50	161.47	932.04	1.4770	94.35	7.53	100.08
.8600	771.90	158.95	916.18	1.4970	160.40	13.38	170.73
.8800	743.40	151.70	880.97	1.5200	227.70	20.02	243.39
.9000	499.00	91.95	581.46	1.5390	244.30	22.18	261.83
.9150	565.40	104.72	659.37	1.5580	240.50	21.93	257.86
.9250	609.20	126.87	724.49	1.5780	217.50	19.41	232.78
.9340	150.40	25.37	172.91	1.5920	227.80	24.80	248.27
.9403	483.00	96.01	569.83	1.6100	206.70	22.06	224.83
.9500	268.60	48.29	311.79	1.6300	213.10	23.10	232.15
.9550	280.00	50.44	325.12	1.6460	205.80	22.23	224.11
.9650	476.40	93.67	561.01	1.6780	193.40	20.73	210.45
.9800	559.30	115.54	664.21	1.7400	152.20	15.65	164.96
.9935	628.70	136.41	753.16	1.8000	26.48	2.10	28.08
1.0400	576.50	124.43	689.97	1.8600	1.74	.12	1.83
1.0700	533.60	113.08	636.54	1.9200	1.01	.07	1.06
1.1000	364.70	36.45	394.22	1.9600	17.86	1.41	18.93
1.1200	97.69	7.58	103.41	1.9850	72.70	5.92	77.24
1.1230	59.58	4.41	62.86	2.0050	22.47	1.77	23.81
1.1319	241.30	21.84	258.66	2.0350	83.79	6.91	89.11
1.1351	23.92	1.67	25.13	2.0650	54.45	4.42	57.84
1.1610	285.80	27.18	307.55	2.1000	80.38	6.68	85.53
1.1800	392.50	42.13	427.16	2.1480	78.12	6.52	83.16
1.2350	396.00	45.15	433.62	2.1980	70.27	5.84	74.78
1.2900	330.80	35.35	359.86	2.2700	68.36	5.74	72.80
1.3200	203.50	18.75	218.38	2.3600	58.32	4.84	62.05
1.3500	27.40	2.10	28.98	2.4500	23.37	1.85	24.78



APPENDIX D.

SUNLIGHT CONCENTRATION IN FLAT-PLATE PHOTOVOLTAIC MODULES

## APPENDIX D

### SUNLIGHT CONCENTRATION IN FLAT-PLATE PHOTOVOLTAIC MODULES

#### D.1 BACKGROUND

The basic photovoltaic module consists of solar cells embedded in a pottant. Some of the incident sunlight is reflected from the opaque pottant between the cells, is reflected within the encapsulation system, and eventually impinges on the cells. This enhancement of solar cell irradiation is referred to as the zero-depth concentrator phenomenon by Mark and Volk [12], who investigated this enhancement effect for several different cell patterns. Their findings that are applicable to this analysis are discussed in this appendix.

Mark and Volk made the following assumptions:

- The direction of the incident sunlight is normal to the module surface.
- The light reflected from the intercell areas is of a Lambertian form, with a hemispherical reflectivity of one.
- The module has a single, homogeneous, nonabsorbing top cover. No consideration is made of any pottants or spacer materials between the top cover and the solar cell or the intercell areas.

- Fresnel's equation, eq. (5-6), is approximated by its small-angle approximation, eq. (5-8), for angles less than the critical angle. The error introduced by this approximation is small.

The results of their analysis indicate that the enhancement effect in the module occurs primarily along the edges of the cells. To show this, consider two semi-infinite sheets, one a white reflector and the other a solar cell, under a top cover of thickness,  $t$ , as shown in Figure D-1. The incident light is of unit intensity. Due to internal reflections (and the assumption of a nonabsorbing top cover), the light intensity within the module will be greater than one. The increase in light intensity in the array is shown as a function of normalized distance in Figure D-2; here it is seen that the enhancement effect is limited almost entirely to a depth of  $6t$  units ( $N$  = index of refraction of front cover). This enhancement effect increases with increasing top cover index of refraction, since the critical angle decreases for an increase in the index of refraction. The smaller the critical angle, the greater the amount of light reflected diffusely from the intercell areas being internally reflected off the top cover and back toward the cells.

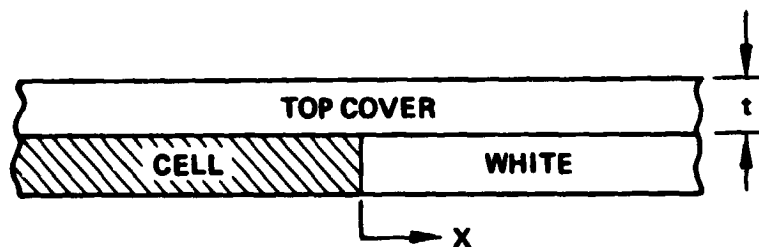


Figure D-1. Slice Through Infinite Module Consisting of Semi-Infinite Cell and Semi-Infinite White Reflecting Region.

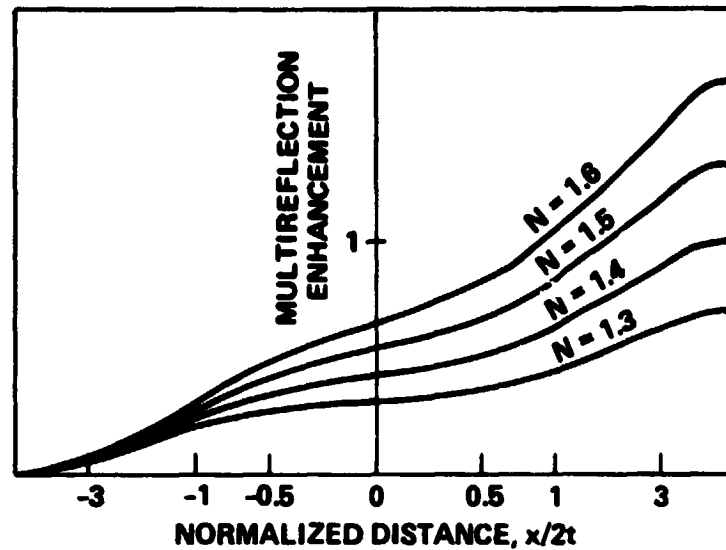


Figure D-2. Enhancement Effect Due to Multiple Internal Reflections in Module Configuration Shown in Figure D-1.

Now consider the module configuration shown in Figure D-3. This configuration consists of an infinitely-long, white reflecting strip between two semi-infinite solar cells. For rectangular cells, the width of the space between cells is much smaller than the cell dimensions. Thus, the intercell areas can be treated as infinitely-long strips, and the results for the configuration shown in Figure D-3 are directly applicable to the optical analysis developed in Section 5.

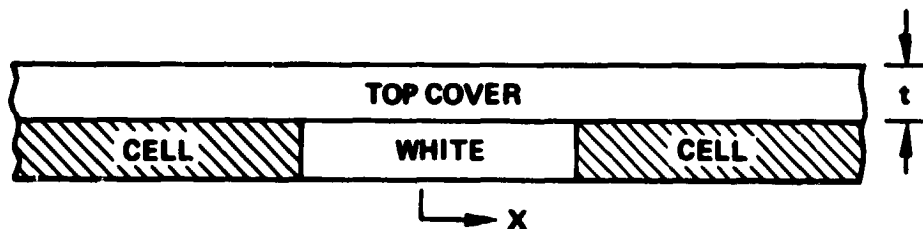


Figure D-3. Slice Through Infinite Area Consisting of Two Semi-Infinite Solar Cells Separated by an Infinitely-Long, White Reflecting Strip.

The enhancement is shown in Figure D-4 as a function of normalized distance for the infinite strip configuration pictured in Figure D-3. The vertical bars on each curve represent the width of the white reflecting area. These results are for a top cover index of refraction of 1.5. As shown before, the enhancement effect in the solar cells is concentrated in the first few normalized units. It is also seen in Figure D-4 that the enhancement effect initially increases for wider reflecting regions but then levels off as a saturation point is reached. As the reflecting strip becomes very wide, the limiting case shown in Figure D-2 is reached.

Mark and Volk also analyzed the case of a circular cell surrounded by an infinite, white reflecting surface as shown in Figure D-5. The results for this geometry are shown in Figure D-6, where the integrated enhancement in the solar cell is plotted as a function of cell radius in normalized units, for a top-cover refractive index of 1.5. The integrated enhancement in the cell decreases as the radius of the cell increases. This is to be expected since the enhancement effect occurs only along the edge of the cell. As the radius of the cell increases, the area of the cell increases as the square of the radius, but the enhanced area is only linearly proportional to the radius. As a consequence, the integrated enhancement decreases as the inverse of the radius.

## D.2 CORRECTION FOR SUNLIGHT CONCENTRATION EFFECTS

After the radiosity-irradiation network is analyzed, the results obtained need to be adjusted to account for internal reflections between the intercell areas and the solar cells. The assumptions listed in Section D.1 still apply, but with the following exceptions:

- In Section D.1, the hemispherical reflectivity of the area between cells was assumed to equal one. In this section, the effect of imperfect (i.e. reflectivity  $< 1$ ) reflecting areas between cells is approximated by multiplying the enhancement effect calculated in Section D.1 by the square of the actual hemispherical reflectance,  $\rho_i$ . The power of two for  $\rho_i$  is

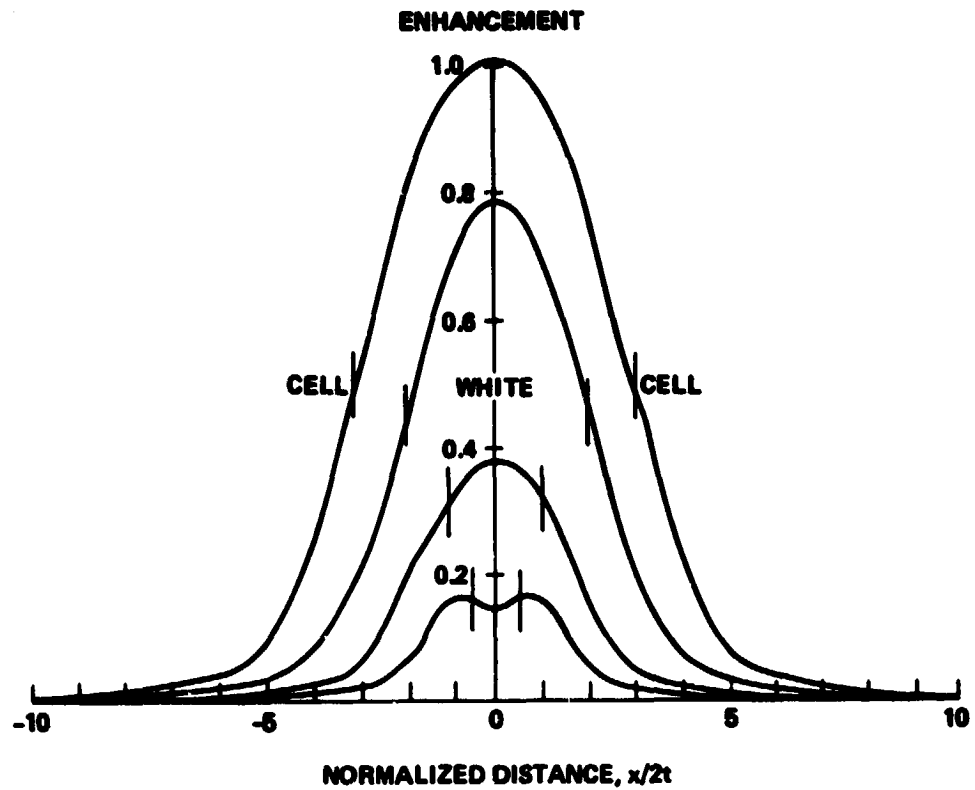


Figure D-4. Enhancement Effect Due to Multiple Internal Reflections in the Module Configuration Shown in Figure D-3.

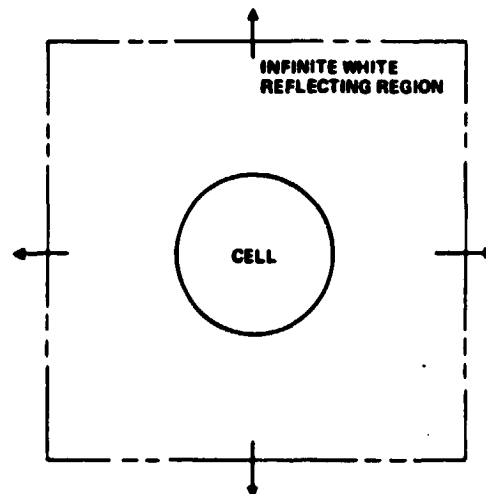


Figure D-5. Circular Solar Cell Surrounded by Infinite White Reflecting Region Under Top Cover of Thickness  $t$ .

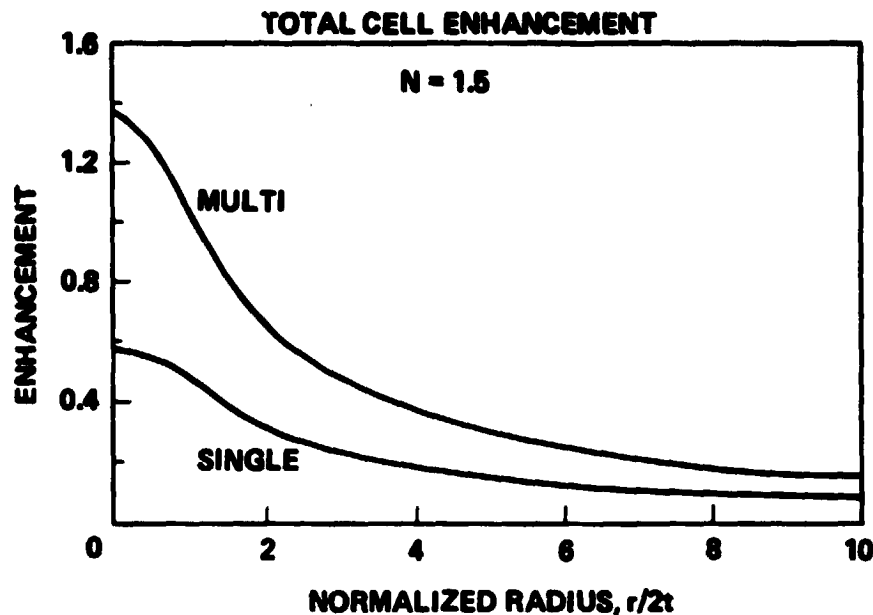


Figure D-6. Average Enhancement Over Entire Cell for Circular Cell Surrounded by Infinite Reflecting Region

an approximation based on the reasonable assumption that the power must be greater than one since the enhancement effect, which is due to multiple internal reflections, is about twice that due to a single reflection. In other words, much of the light is reflected off the intercell areas more than once.

- Allowance is made for more than one material layer above the cell by assuming a top cover thickness equal to the sum of the thicknesses of the actual layers above the cell.

In addition, the index of refraction of the top cover is the highest for any material layer above the cell. As seen in Figure D-7, this is a reasonable approximation if there is no antireflection coating on the top cover. The effect of an antireflection coating would be to greatly reduce the internal reflections that give rise to the enhancement effect. Consequently, if the top cover has an antireflection coating, it is safe to assume that

there is no enhancement effect, and the results from the radiosity-irradiation analysis presented in Section 5 can be used without modification.

Absorption of internally reflected light by the encapsulation layers will reduce the enhancement effect. This can be taken into account by multiplying the energy absorbed in the cell,  $Q_c$ , by the term  $(1+E_i)$ , where  $E_i$  has been calculated for a nonabsorbing medium, (for square cells,  $i = sq$ ; for circular cells,  $i = cir$ ). This has the effect of applying the absorption effects calculated in the radiosity-irradiation analysis, and inherent in  $Q_c$ , to the enhancement effect term.

Two equations will now be derived to account for the enhancement phenomenon - one for modules using rectangular cells, and one for modules using circular cells. One term common to both equations is a correction factor for the index of refraction of the cover material. Both equations will be derived from results based on an index of refraction of 1.5 for the top cover. The following correction factor,  $C$ , based on Figure D-2 is used

$$C = 2(N-1) \quad (D-1)$$

where  $N$  is the index of refraction of the top cover material.

A cross section of a module using rectangular cells is shown in Figure D-8, which also shows the principle dimensions. This module is characterized by intercell areas that are relatively long and narrow, and consequently, the results given in Figure D-4 are applicable to this configuration. The results of Figure D-4 were put into a more usable form, by calculating the areas under the curves in the cell regions for each of the reflecting region widths. These areas are plotted as a function of the reflecting strip width in Figure D-9. The upper limit on the enhancement effect as the reflecting strip becomes very wide is the case shown in Figure D-2 for a semi-infinite reflecting area. The following equation has been derived to predict the irradiation enhancement,  $IE$ , as a function of reflecting strip width and top cover thickness.

$$IE = 1.4t (1 - e^{-.22 w/t}) \quad (D-2)$$



To determine the average increase in solar irradiation for the entire solar cell,  $E_{sq}$ , it is necessary to multiply the above fractional increase by the ratio of solar cell perimeter to cell area. The average enhancement for the whole cell is then

$$\begin{aligned} E_{sq} &= IE \ (4s/s^2) \\ &= 5.6 \ \frac{t}{s} \left(1 - e^{-.22w/t}\right) \end{aligned} \quad (D-3)$$

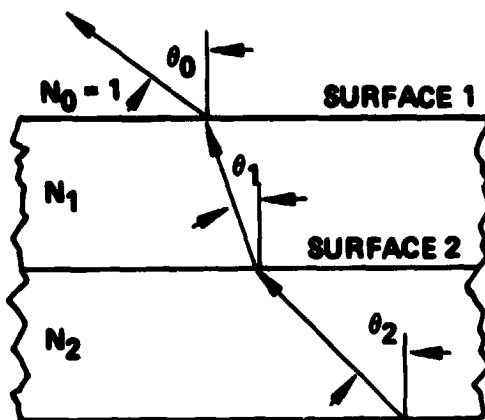
Including the correction factor,  $C$ , for a top cover index of refraction,  $N$ , and the square of the reflectivity of the intercell area, the fractional increase in cell irradiation for square cells is thus

$$E_{sq} = 11.2 \ \rho_i^2 \ \frac{t}{s} \ (N-1) \left(1 - e^{-.22w/t}\right) \quad (D-4)$$

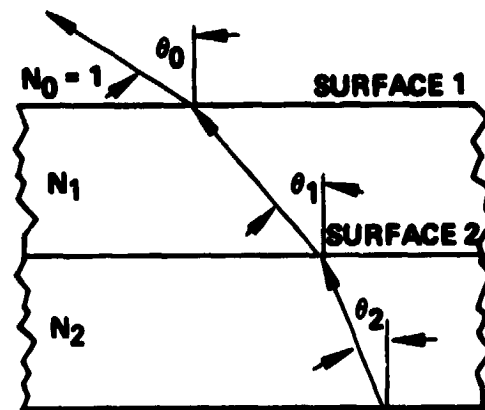
To obtain the total fraction of solar irradiation absorbed in the solar cell, the enhancement term,  $E_{sq}$ , must be added to the result obtained from the irradiation-radiosity analysis for  $Q_c$

$$Q_c = Q_c (1 + E_{sq}) \quad (D-5)$$

The average enhancement for a single circular solar cell surrounded by an infinite reflecting region is shown in Figure D-6. In an actual arrangement of circular cells, the enhancement is less than that shown in Figure D-6, because there is less reflecting area. It is recommended here that the enhancement shown in Figure D-6 be multiplied by the ratio of intercell area to total module area to account for this reduction in reflecting area. Based on Figure D-6, the following equation relates the average increase in irradiation for the entire cell,  $E_{cir}$ , to the cell radius, top cover thickness, and cell layout;  $A_i$  is the area of the intercell spaces, and  $A_m$  is the area of the whole module. Adding the correction factors for the refractive index of the top cover and the intercell area reflectivity, the fractional increase in cell irradiation in an array of circular solar cells becomes



$$N_1 > N_2$$



$$N_2 > N_1$$

$$N_2 \sin \theta_2 = N_1 \sin \theta_1 = \theta_0$$

**FOR TOTAL INTERNAL REFLECTION  
AT SURFACE 1**

$$\theta_{IC} = \sin^{-1}\left(\frac{1}{N_1}\right)$$

**THERE IS NO INTERNAL REFLECTION  
AT SURFACE 2. THEREFORE,  $N_1$   
DETERMINES WHEN TOTAL INTERNAL  
REFLECTION OCCURS**

**FOR TOTAL INTERNAL REFLECTION  
AT SURFACE 1**

$$\theta_{IC} = \sin^{-1}\left(\frac{1}{N_1}\right)$$

**THE ANGLE  $\theta_2$  TO GIVE  $\theta_1 = \theta_{IC}$  IS**

$$\theta_2 / \theta_{IC} = \sin^{-1}\left(\frac{N_1}{N_2} \sin \theta_{IC}\right)$$

$$= \sin^{-1}\left(\frac{N_1}{N_2} \frac{1}{N_1}\right)$$

$$\theta_2 / \theta_{IC} = \sin^{-1}\left(\frac{1}{N_2}\right)$$

**FOR TOTAL INTERNAL REFLECTION  
AT SURFACE 2**

$$\theta_{2C} = \sin^{-1}\left(\frac{N_1}{N_2}\right)$$

**SINCE  $\theta_{2C} / \theta_{1C} \leq \theta_{2C}$ ,  $N_2$  ALONE**

**DETERMINES  
WHEN TOTAL INTERNAL REFLECTION  
OCCURS**

Figure D-7. Total Internal Reflection for Two-Layer Encapsulation System

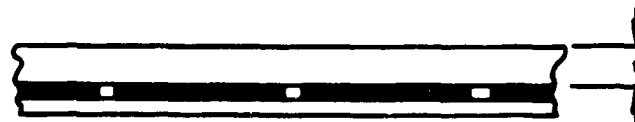
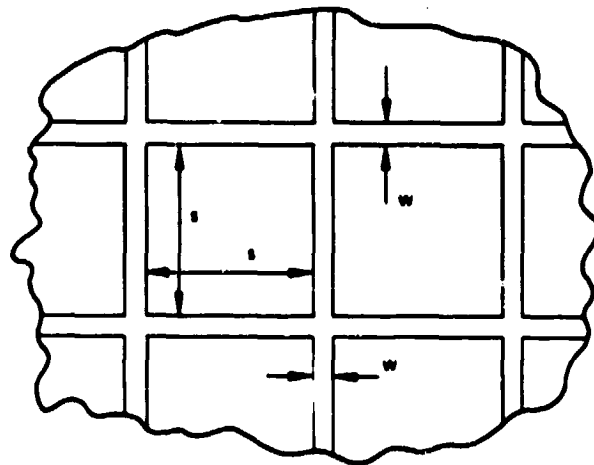


Figure D-8. Section of Module Using Square Solar Cells.

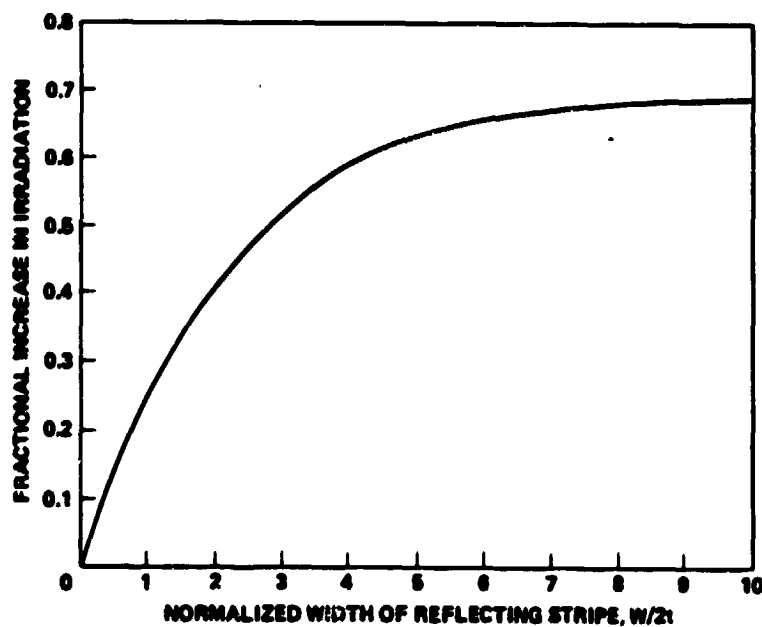


Figure D-9. Increase in Irradiation as a Function of Reflecting Strip Width for Results Shown in Figure D-1.

$$E_{cir} = 6.4 \rho_1^2 (N-1) \left( \frac{A_1}{A_m} \right) \frac{t}{R} \quad (D-6)$$

These results are valid for  $R/t > 2$ . To obtain the fraction of the total incident energy absorbed in the solar cell, eq. (D-5) is used with  $E_{cir}$  in place of  $E_{sq}$ .

One final adjustment to be made to the results of the radiosity-irradiation analysis is to account for increased energy absorption in the encapsulation layers above the cell due to internal reflections from the intercell area. This can be done in a manner similar to eq. (D-3) for correcting the energy absorbed in the solar cell

$$\begin{aligned} Q_1' &= Q_1 (1 + E_{sq}) \\ Q_2' &= Q_2 (1 + E_{sq}) \end{aligned} \quad (D-7)$$

This completes the process of accounting for sunlight concentration effects. Equations (D-4), (D-5), (D-6), and (D-7) are used for this purpose.

## APPENDIX E

COMPARISON OF METHODS FOR SOLVING MULTIREFLECTION

RADIATION PROBLEMS IN SINGLE-LAYER THIN FILMS

## APPENDIX E: COMPARISON OF METHODS FOR SOLVING MULTIREFLECTION RADIATION PROBLEMS IN SINGLE-LAYER THIN FILMS

### E.1 INTRODUCTION

The classical method of solving multireflection, radiation exchange problems is to set up a number of infinite series and solve these series to obtain the reflected, transmitted, and absorbed energy fluxes. In this appendix, a method involving the solution of simultaneous equations is used to determine these fluxes. This method is similar to that developed by Siegel [19].

The two methods will be used to calculate reflectance and transmittance through a transparent layer of thickness,  $t$ , as shown in Figure E-1. Surfaces A and B have reflectivity,  $\rho$ , and transmissivity,  $\tau$ . The material has an absorption coefficient,  $a$ . The transmittance,  $T$ , of the layer is given by the equation

$$T = e^{-at} \quad (E-1)$$

### E.2 RADIOSITY-IRRADIATION METHOD

To solve for the radiant energy absorbed in the layer, the radiosities and irradiances must be determined for each side of each surface involved in the radiation exchange process. Seven radiant fluxes are shown in Figure E-1, and the equations for these fluxes are:

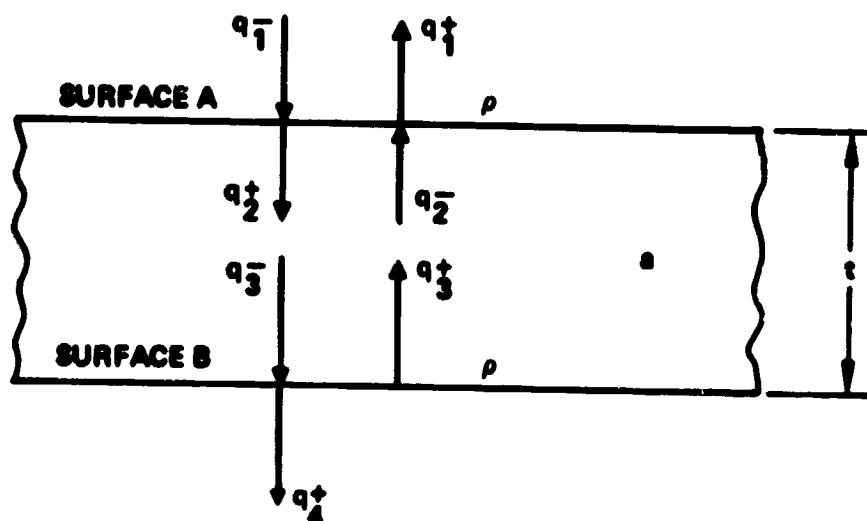


Figure E-1. Radiant Energy Fluxes in a Transparent Thin Film

$$q_1^- = 1$$

$$q_1^+ = \rho q_1^- + (1-\rho)q_2^-$$

$$q_2^- = \tau q_3^+$$

$$q_2^+ = (1-\rho)q_1^- + \rho q_2^-$$

$$q_3^- = \tau q_2^+$$

$$q_3^+ = \rho q_3^-$$

$$q_4^+ = (1-\rho)q_3^-$$

(E-2)

where the irradiation,  $q_1^-$ , has been normalized to a value of one

This system of equations is given below in matrix form

$$\begin{bmatrix} 1 & -1(1-\rho) & 0 & 0 & 0 & 0 \\ 0 & 1 & 0 & 0 & -T & 0 \\ 0 & -\rho & 1 & 0 & 0 & 0 \\ 0 & 0 & -T & 1 & 0 & 0 \\ 0 & 0 & 0 & -\rho & 1 & 0 \\ 0 & 0 & 0 & -(1-\rho) & 0 & 1 \end{bmatrix} \begin{bmatrix} q_1^+ \\ q_2^- \\ q_2^+ \\ q_3^- \\ q_3^+ \\ q_4^+ \end{bmatrix} = \begin{bmatrix} \rho \\ 0 \\ (1-\rho) \\ 0 \\ 0 \\ 0 \end{bmatrix} \quad (E-3)$$

or, in matrix notation

$$[M] \bar{q} = \bar{C} \quad (E-4)$$

The unknown radiant fluxes are then solved by inverting matrix M.

$$\bar{q} = [M]^{-1} \bar{C} \quad (E-5)$$

The radiant fluxes are given by the following equations

$$q_1^- = 1$$

$$q_1^+ = \rho + \frac{\rho(1-\rho)^2 T^2}{1-\rho^2 T^2} \quad (E-6a)$$

$$q_2^- = \frac{\rho(1-\rho) T^2}{1-\rho^2 T^2} \quad (E-6b)$$

$$q_2^+ = \frac{1-\rho}{1-\rho^2 T^2} \quad (E-6c)$$

$$q_3^- = \frac{T(1-\rho)}{1-\rho^2 T^2} \quad (E-6d)$$



$$q_3^+ = \frac{\rho T(1-\rho)}{1-\rho^2 T^2} \quad (\text{E-6e})$$

$$q_4^+ = \frac{\rho T(1-\rho)^2}{1-\rho^2 T^2} \quad (\text{E-6f})$$

Once the fluxes are known, the radiant energy reflected from, absorbed in, and transmitted thru the layer are determined by means of the following relations:

$$\text{Energy reflected} = q_1^+ \quad (\text{E-7})$$

$$\text{Energy absorbed} = q_a = q_2^+ + q_3^+ - q_2^- - q_3^- \quad (\text{E-8})$$

$$\text{Energy transmitted} = q_4^+ \quad (\text{E-9})$$

Substitution of eqs. (E-6) into eqs. (E-7) thru (E-9) then yields the following expressions

$$\begin{aligned} q_a &= \frac{1-\rho}{1-\rho^2 T^2} - \frac{\rho T^2(1-\rho)}{1-\rho^2 T^2} + \frac{\rho T(1-\rho)}{1-\rho^2 T^2} - \frac{T(1-\rho)}{1-\rho^2 T^2} \\ q_a &= \frac{(1-\rho)(1-\rho T^2 + \rho T - T)}{1-\rho^2 T^2} \\ q_a &= \frac{(1-\rho)(1-T)}{1-\rho T} \end{aligned} \quad (\text{E-10})$$

The transmitted energy is given by eq. (E-6f) and the reflected energy is given by eq. (E-6a). Note that as  $\alpha \rightarrow 0$ ,  $T \rightarrow 1$ , and eq. (E-6a) reduces to:

$$q_1^+ = \rho \quad (\text{E-11})$$

This method of defining radiosities and irradiances for each side of each surface involved in a radiation exchange is easily expanded to many surfaces

and absorbing media in series. The resulting system of simultaneous equations is readily solved by digital computer, or for smaller problems, by programmable calculator.

### E.3 INFINITE SERIES METHOD

The multiple reflections that occur between surfaces A and B are illustrated in Figure E-2. Only the first few of an infinite number of rays are shown.

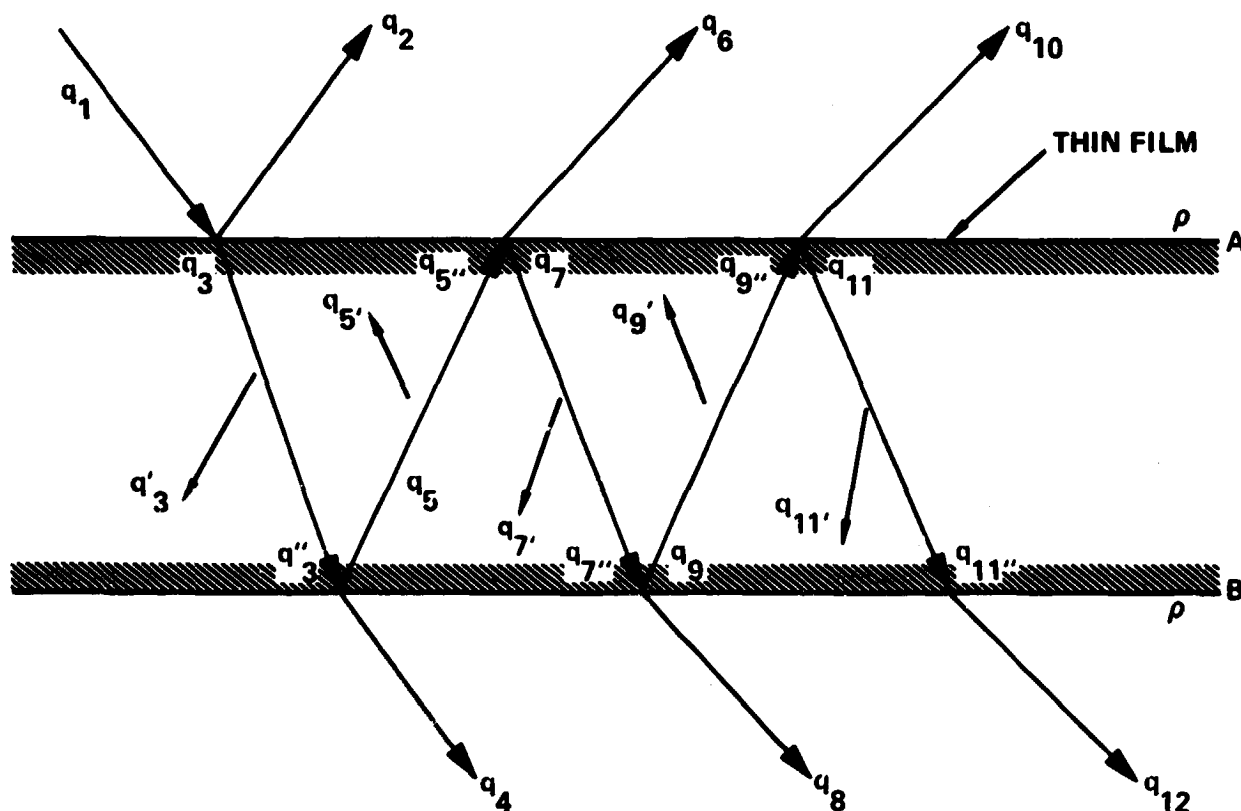


Figure E-2. Path of Light Ray in Single-Layer Thin Film

The energy in each ray is given by

$$q_1 = 1 \text{ (normalized value)}$$

$$q_2 = (1-\rho)q_1 = 1-\rho$$

$$q_3 = \rho q_1 = \rho$$

$$q_3' = (1-T)q_2 = (1-\rho)(1-T)$$

$$q_3'' = Tq_2 = (1-\rho)T$$

$$q_4 = (1-\rho)q_3'' = (1-\rho)^2 T$$

$$q_5 = \rho q_3'' = (1-\rho)T$$

(E-12)

$$q_5' = (1-T)q_5 = \rho(1-\rho)T(1-T)$$

$$q_5'' = Tq_5 = \rho(1-\rho)T^2$$

$$q_6 = (1-\rho)q_5'' = \rho(1-\rho)^2 T^2$$

$$q_7 = \rho q_5'' = \rho^2(1-\rho)T^2$$

$$q_7' = (1-T)q_7 = \rho^2(1-\rho)T^2(1-T)$$

$$q_7'' = Tq_7 = \rho^2(1-\rho)T^3$$

$$q_8 = (1-\rho)q_7'' = \rho^2(1-\rho)^2 T^3$$

$\vdots$

etc

The energy absorbed in the film is obtained by summing the fluxes impinging at each surface. Thus, for  $q_a$

$$q_a = q_3 + q_5 + q_7 + q_9 + \dots$$

$$q_a = (1-\rho)(1-T) + \rho(1-\rho)T(1-T) + \rho^2(1-\rho)T^2(1-T) + \rho^3(1-\rho)T^3(1-T) + \dots \quad (E-13)$$

$$q_a = (1-\rho)(1-T)(1 + \rho T + \rho^2 T^2 + \rho^3 T^3 + \dots)$$

Knowing that

$$1 + \rho T + \rho^2 T^2 + \rho^3 T^3 + \dots = \frac{1}{1-\rho T} \quad (E-14)$$

the equation for  $q_a$  can be written as follows

$$q_a = \frac{(1-\rho)(1-T)}{1-\rho T} \quad (E-15)$$

Equation (E-15) is the same as eq. (E-10) obtained from the radiosity irradiation network.

The energy transmitted thru the layer is given by

$$q_t = q_4 + q_8 + q_{12} + \dots$$

$$q_t = (1-\rho)^2 T + \rho^2 (1-\rho)^2 T^3 + \rho^4 (1-\rho)^2 T^5 + \dots \quad (E-16)$$

$$q_t = (1-\rho)^2 T (1 + \rho^2 T^2 + \rho^4 T^4 + \dots)$$

Since

$$1 + \rho^2 T^2 + \rho^4 T^4 + \dots = \frac{1}{1-\rho^2 T^2} \quad (E-17)$$

equation (E-16) reduces to

$$q_t = \frac{(1-\rho)^2 T}{1-\rho^2 T^2} \quad (E-18)$$

This result is the same as equation (E-6f) obtained from the radiosity-irradiation analysis.

As the number of surfaces increase in the multireflection problem and the reflectivities and absorptivities vary from layer to layer, the infinite series method becomes extremely complex. For these problems, it is easier to solve the simultaneous equations resulting from the radiosity-irradiation method.

## Appendix F

### LIFE CYCLE COST

In order to compare one design to another the life cycle cost of power must be determined. Figure F1 shows the life costing algorithm which was developed to show the power cost over the life of the plant.

To use this algorithm many assumptions must be made. Table F1 lists these assumptions. All costs are in 1980 dollars. Assumptions were based on data given during the Flat Plate Photovoltaic Module and Array Circuit Design Optimization Workshop on March 31 and April 1, 1980 at JPL. The three designs shown in Table F2 were looked at in detail. Tables F3 and F4 show how an initial array cost was developed for the glass superstrate case. Table F5 shows the results of this analysis for the three designs based on 5, 10, and 20 year module life.

It can be seen from this table that module life is the major factor in arriving at life cycle cost. The balance of system cost also represents a significant portion of the initial array cost.

This analysis represents one set of assumptions in relatively simple costing algorithm. The use of life cycle cost to determine the relative merits of various designs will only be useful when better information is available on the true life expectancy of photovoltaic modules.

Figure F1  
LIFE COSTING ALGORITHM

$$\left( \frac{\text{BOPC} + \left( \frac{\text{IAC} + \sum_{n=1}^L C_n (1+k)^{-n}}{\text{PE} \times \frac{1\text{kW}}{\text{m}^2}} \right)}{\left( \text{AI} \right) \times \left( \sum_{n=1}^L P_n (1+k)^{-n} \right) \times \left( \frac{1\text{kW}}{\text{m}^2} \right)} \right) = \text{PC}_L$$

BOPC = balance of plant costs \$/kW

IAC = initial array cost \$/m<sup>2</sup>

L = plant life years

C<sub>n</sub> = operating cost in year n \$/m<sup>2</sup>

k = discount rate

PE = plant efficiency

AI = annual insulation kWh/m<sup>2</sup>/year

P<sub>n</sub> = fraction of initial power in year n

PC<sub>L</sub> = power cost over life of plant in \$/kWh

Table F1

COSTING ASSUMPTIONS

Soiling Loss	8%
Wiring Loss	2%
Cell Matching Loss	5%
Power Condition Loss	6%

Thus, Plant Efficiency = .81 x Module Efficiency

Discount Rate = 10%

Balance of Plant Costs = \$150/kW

Maintenance = \$1.25 m<sup>2</sup>/Year

Annual Incident Insolation = 1825 kW-h/m<sup>2</sup>/Yr.

Table F2

TASK III DESIGN CONCEPTS

<u>Layer</u>	<u>Material</u>		
	<u>#1</u>	<u>#2</u>	<u>#3</u>
Surface	None	None	None
Top Cover	Tempered Glass	Tedlar	Tedlar
Pottant	EVA	EVA	EVA
Spacer	Crane Glas	Crane Glas	Crane Glas
Substrate	None	Wood Product	Mild Steel
Back Cover	Al-Acrylic	EVA Crane Glas	EVA Crane Glas



Table F3  
MODULE COSTING

	<u>1980 \$/m<sup>2</sup></u>
Cell Circuit	60.00
1/8" Glass Tempered	8.18
20 mil EVA Pottant	1.02
10 mil Crane Glas	.03
Al/Acrylic Back Cover	.54
Termination	1.00
Assembly	<u>4.70</u>
MODULE COST	75.47

Table F4  
INITIAL ARRAY COSTING

	<u>1980 \$/m</u>
Module Cost	75.47
Panel Frame Structure and Assembly	18.00
Panel Wiring	2.00
Panel Installation	1.00
Installed Field Structure and Foundations	18.00
Land and Preparation	<u>4.00</u>
INITIAL ARRAY COST	118.47

Table F5

LIFE CYCLE COSTS

		<u>Glass Superstrate</u>	<u>Wood Substrate</u>	<u>Steel Substrate</u>
\$ kW-H @	5 Year Life	.1828	.1774	.1793
	10 Year Life	.1271	.1238	.1248
	20 Year Life	.1021	.0999	.1004
	Module Cost	75.47 \$/m <sup>2</sup>	70.12 \$/m <sup>2</sup>	75.30 \$/m <sup>2</sup>
Initial Array Cost		118.47	113.12	118.30